Optical and electrical excitation of nanoantennas with atomic-scale gaps

Dissertation zur Erlangung des
naturwissenschaftlichen Doktorgrades
der Bayerischen Julius-Maximilians-Universität
Würzburg

vorgelegt von

Johannes Kern

aus Würzburg

Würzburg 2014

Eingereicht am _____
bei der Fakultät für Physik und Astronomie

1. Gutachter: Prof. Dr. Bert Hecht
2. Gutachter: Prof. Dr. Martin Kamp
3. Gutachter: _____
der Dissertation

1. Prüfer: Prof. Dr. Bert Hecht
2. Prüfer: Prof. Dr. Martin Kamp
3. Prüfer: _____
im Promotionskolloquium

Tag des Promotionskolloquiums: _____

Doktorurkunde ausgehändigt am: _____

Contents

1 Introduction and overview

The interaction of photons with electrons is not only of fundamental interest but is also a key requirement for many technological applications. However, the interaction between photons and electrons, i.e. light and matter, is typically weak. The reason is that there is a mismatch between the spatial confinement of electrons in matter and the possible confinement of propagating photons, which is governed by diffraction.

The consequences of this mismatch can be easily realized by considering the example of the absorption of visible light by some nano-object. This object could be a fluorescent molecule used for imaging of a biological sample or some nanophotonic element on a future computer chip which converts a photonic to an electronic signal. Let us assume that a freely propagating light beam with a diameter of 1 mm impinges on the nano-object. Inside the nano-object photons are absorbed by inducing electronic transitions between localized electronic states. Within a simple particle-in-a-box model the discrete (n=1, 2, 3,...) energy states of the nano-object are given by $E_n = \frac{h^2 n^2}{8mL^2}$, where h is Planck's constant, m the electron mass and L the length of electron confinement. Using this model, it can be calculated that a transition involving the energy of a visible photon requires an electron confinement length on the order of a few nanometers. Consequently the active region of the nano-object is many times smaller than the light beam and most photons will pass by unaffectedly.

An obvious strategy to enhance the absorption is to place a focusing element between the light beam and the nano-object. Using conventional optics, such as a microscope objective, the confinement of light is limited by diffraction to a diameter of about $\lambda/2$. This remains 2-3 orders of magnitude larger than the nano-object and only a small fraction of the incident light can be absorbed by nano-objects, such as single molecules[1]. A further consequence of the length scale mismatch is that the coupling of quantum emitters to the electromagnetic field is weak, which results in low photon emission rates due to long excited state lifetimes on the order of nanoseconds [2].

A possible solution to these problems is the use of plasmonic metal nanostructures which are able to localize optical fields to regions far below the diffraction-limit. This is possible because the free electrons inside the metal particle respond collectively to the incoming fields and the displaced electrons constitute a source for evanescent optical near-fields. Plasmons are therefore a hybrid excitation involving electrons and photons. Plasmonic near-fields are not only strongly localized but, if the dimensions of the nanostructure is chosen such that the electrons respond resonantly, the near-field intensity can be enhanced by a factor of more than 1000 with respect to the exciting field. Consequently, plasmonic nanostructures build an efficient bridge between the macroscopic and the nanoscopic world and are therefore named optical antennas. The link between far-field and near-field works in both directions and an optical antenna can increase absorption as well as emission of photons. Optical antennas are therefore an important concept for the interaction of light with nanomatter.

The development of optical antennas was motivated by microscopy [3] and recently plasmonic nanoantennas have evolved into a vivid and active field of research [4, 5]. Their ability to localize fields to sub-wavelength scale has been shown by optical excitation [6, 7] as well as excitation with an electron beam [8, 9]. Upon excitation with polarization-shaped laser pulses these fields can be controlled in space and time [10]. An obvious application of localized plasmonic fields is high-resolution microscopy and spectroscopy. Single-molecule fluorescence signals have been recorded with a resolution of 15 nm [11]. Sub-nanometer resolution has been achieved for plasmon-enhanced Raman scattering [12].

In most cases the field localization goes in hand with an enhancement of the field and high-intensity optical near-fields have been exploited for the amplification of various linear and non-linear signals. Second- [13] and third-harmonic [14] generation, continuum generation [15] as well as extreme-ultraviolet light generation [16] has been demonstrated using plasmonic nanoantennas. Moreover, strong non-linearities have been observed for electron emission from sharp metal tips in the strong-field regime [17, 18]. Gigantic enhancement factors of more than 10^{10} are observed for surface-enhanced Raman spectroscopy [19]. A limiting factor of fluorescence enhancement is quenching of emitters in close vicinity to metal surfaces as well as the fact that the fluorescence quantum efficiency of good emitters is already close to unity. Experimentally obtained enhancement factors are less than 100 [20, 21] for intrinsically efficient emitters. However, for molecules with a low intrinsic fluorescence efficiency, enhancements of more than 1000 have been observed [22, 23].

Besides intensity enhancement it has been shown that the radiative properties of single emitters can be controlled by the antenna. Directed emission [24, 25], antenna-controlled polarization [26] and a shaping of the emission spectra [27, 28] have been demonstrated. The quantum nature, i.e. single photon emission, of the emitters remains undisturbed [29, 30]. Another interesting aspect is the coupling of excitonic and plasmonic states. In the intermediate coupling regime, interference between the broad plasmon and the narrow exciton gives rise to a Fano-like resonance [31]. The strong-coupling regime manifests itself in the observation of Rabi splitting [32] and Rabi oscillations [33]. A particular exciting field is that of electro-plasmonics. Plasmonic nanoantennas have been used to enhance photodetection [34–36], to improve photovoltaic devices [37] as well as for the conversion of solar to chemical energy [38]. Moreover, light emitting devices [39, 40] as well as electrically-pumped nanolasers [41, 42] have been realized.

Most of the above described experiments and applications rely on the high near-field intensity provided by the plasmonic nanostructures. Particularly strong fields occur in the gap of two coupled particles. With decreasing gap size the Coulomb interaction over the gap becomes stronger, which leads to increased surface charge accumulation accompanied by even more intense optical near-fields. At the beginning of this thesis it was an open question at what length scales electron tunneling and spill-out start to affect the intensity enhancement and confinement of plasmonic fields. Within the first part of this thesis it was attempted to answer this question and the results will be presented in Chapter 4. In general it is not possible to measure the field confinement and enhancement directly. However, an elegant approach was found and is based on the fact that the coupling of two metal particles results in a hybridization of the single

particles resonance into a symmetric and anti-symmetric Eigenmode. The energy splitting of these two resonances strongly depends on the interaction strength, which is mainly determined by the gap size. Scattering spectra of self-assembled plasmonic structures, with gaps reaching below 0.5 nm, were recorded. The good agreement to a numerical model suggest that a strong confinement and enhancement can be achieved in atomic-scale gaps down to about 0.5 nm. Similar experiments have been conducted by several other research groups [43–46]. The conclusion from these studies is that the onset of quantum effects is at about 0.5 nm.

The fact that in gaps of plasmonic nanostructures resonant optical fields can be concentrated to (sub)-nanometer length scales opens the door for investigating the interaction between electrons and photons in regions of extremely confined and intense optical fields. However, localized plasmon resonances rely on oscillating currents in noble metal particles with dimensions of a few hundred nanometers and at the beginning of this thesis it was an open question how to electrically connect these structures. A general solution is presented in Chapter 5, where it is demonstrated that electrical connectors can be attached to a nanoantenna without influencing its resonant optical properties. The key idea is to place the connectors close to the center of the antenna, the position where the fields of the isolated structure show a minimum. The realization of electrically-connected antennas required the development of advanced fabrication techniques, involving bottom-up synthesis of single-crystalline gold flakes and top-down focused ion beam (FIB) milling on an insulating substrate. The fabricated structures show excellent optical and electrical properties and provide an ideal platform for the investigation of electro-plasmonic effects.

The last Chapter 6 combines the previously gathered knowledge and demonstrates the realization of electron to photon conversion in a sub-wavelength device. This novel photon source integrates light generation and control into a planar single-material nanostructure. A tunnel junction is obtained by manipulating a gold sphere into the gap of an electrically-connected resonant optical antenna. Upon applying a DC voltage electrons tunnel inelastically across the antenna gap and generate far-field photons via the antenna resonance. The spectrum, directivity and polarization of the radiated photons are therefore dictated by the antenna resonance and the electron-to-photon conversion is strongly enhanced.

2 Basic theoretical concepts and overview of the field

2.1 Plasmonics

A plasma is a state of matter consisting of a dense gas of charged particles. Plasmas can be found in nature and can be created artificially. The sun consists mainly of a plasma and lightning bolts originate from discharges in plasmas. Plasmas are also used in energy-saving fluorescent lamps or in material processing such as sputtering, cleaning or deposition.

Plasmas not only exist in gases, also materials with high electric conductivity and large carrier densities can behave as plasmas. These two requirements are intrinsic properties of metals, which are therefore most typically[1] considered for plasmonic application. Upon illumination with an external electromagnetic field the free electrons in the metal respond collectively. The resulting surface-charge oscillations are 180° out of phase to the applied field and give rise to strongly enhanced optical near-fields which are localized at the vicinity of the metal surface. These surface-charge density oscillations can be ascribed to a quasi-particle named plasmon. Plasmons can be excited at planar interfaces, on extended wires and on finite-sized particles. In the former two cases propagating surface plasmon modes are supported, whereas in the latter case the plasmon modes are localized. For the interaction of light and nanomatter, localized plasmon modes supported by particles are of particular interest. The reason is that their optical near-fields are confined in all three spatial dimensions and for certain particle geometries and sizes the electron response can be resonantly enhanced, leading to exceptionally high near-fields.

For the most simple case of a spherical particle excited by an applied electromagnetic field the momentary charge and field distributions are schematically sketched in Figure 2.1a. Since the applied field will change in time, the resulting charges in the nanoparticle will follow this oscillatory behavior. This situation is in analogy to a mass-spring model, where the electron gas (mass) is displaced and charges of opposite signs build up on each side of the particle leading to a restoring force (spring) depending on the field created by the charge distributions. The mass-spring model is illustrated in Figure 2.1b. It provides the most intuitive description of a localized plasmon and will be used throughout this thesis for the understanding of the plasmon modes of more complex geometries.

The optical properties of localized plasmons depend on the material properties as well as their geometrical shape and spatial extension. The optical properties of metals are governed by the negative real part of their dielectric constant and are discussed

[1] Alternative materials are discussed in [47–49], but so far plasmonic properties in these materials have been restricted to the IR spectral region.

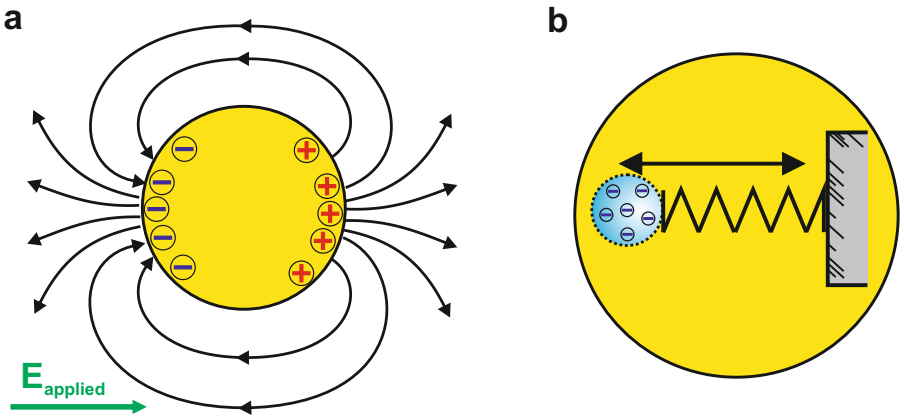

Figure 2.1: Illustration of a particle plasmon resonance. **a** Momentary charge and field distribution of the particle plasmon provided by a single sphere. On resonance the electron oscillation is out of phase to the applied field. **b** Illustration of the mass-spring model. Electron gas (mass) is displaced due to the applied field. Coulomb interaction leads to a restoring force (spring). Adapted from [50].

in detail in the first part of this section. In the two subsequent parts the plasmon resonances of spheres and rods are discussed and described by simple models. In the fourth part the resulting hybridized modes resulting from the coupling of two closely-spaced plasmonic particles are studied. These structures are often called optical antennas, since they provide an efficient link between far- and near-field. This will become clear in the last part of this chapter where different geometries are compared by calculating the radiative and non-radiative rates of a quantum emitter placed in the vicinity of the plasmonic particles. The conclusion of this study is that gap antennas with small gaps are most effective in enhancing the radiative decay rate and can lead to drastic efficiency enhancement of quantum emitters with an intrinsically low efficiency.

2.1.1 Optical response of noble metals

The complex frequency-dependent dielectric function $\epsilon(\omega)$ relates the externally applied field to the induced polarization in the material and consequently describes the optical response of the material. The dielectric function of metals is characterized by a negative real part as well as a positive imaginary part. The negative real part is responsible for the strong reflectivity of metals and, as seen in the next subsection, a requirement for a plasmon resonance. The imaginary part leads to damping of the resonance and a low value is desired. In this thesis gold has been chosen as a material for all structures. The reason is that it combines a favorable dielectric function in the red part of the visible region with an excellent chemical stability and is available in the form of single-crystalline gold flakes (see Chapter 3.1.3).

In a first approximation the dielectric function can be obtained from the Drude-Sommerfeld theory [50]. In this model the electrons of the metal are considered to be a free electron gas and are described as a damped driven oscillator without a restoring

force. Using this model one obtains [50]

$$\varepsilon_{\text{Drude}}(\omega) = 1 - \frac{\omega_\text{p}^2}{\omega^2 + i\gamma\omega}. \tag{2.1}$$

Here $\omega_\text{p} = \sqrt{ne^2/m_\text{e}\varepsilon_0}$ is the plasma frequency and, since e and m are constants, is mainly determined by the electron density n. The damping $\gamma = 1/\tau$ is mainly due to scattering at impurities or phonons and τ is the mean free time between collisions. In Figure 2.2a the dielectric function of gold is plotted using typical values of $\omega_\text{p} = 13.6 \cdot 10^{15}$ s^{-1} and $\gamma = 10 \cdot 10^{15}$ s^{-1} [50]. The direct comparison to the experimental data of Johnson and Christy [51] clearly shows the validity limits of the Drude model. The large deviation for energies larger than 2 eV is due to interband transitions. In a classical picture interband transitions can be described as the oscillations of bound electrons with a resonance frequency ω_0. Each transition then results in a correction term which needs to be added to the Drude term (equation 2.1). Here only one correction term is considered and it reads [50]

$$\varepsilon_{\text{Interband}}(\omega) = 1 + \frac{\widetilde{\omega}_\text{p}^2}{(\omega_0^2 - \omega^2) - i\Gamma\omega}. \tag{2.2}$$

It is important to note that $\widetilde{\omega}_\text{p}^2$ and Γ now describe bound electrons. Further interband transitions at higher energies can be accounted by an offset ε_∞. Using the parameters $\widetilde{\omega}_\text{p} = 4.5 \cdot 10^{15}$ s^{-1}, $\Gamma = 0.9 \cdot 10^{15}$ s^{-1} and $\varepsilon_\infty = 5$ [50] the interband-corrected Drude-Sommerfeld model is compared to the experimental data in Figure 2.2b and a reasonable agreement is found up to energies of 2.7 eV.

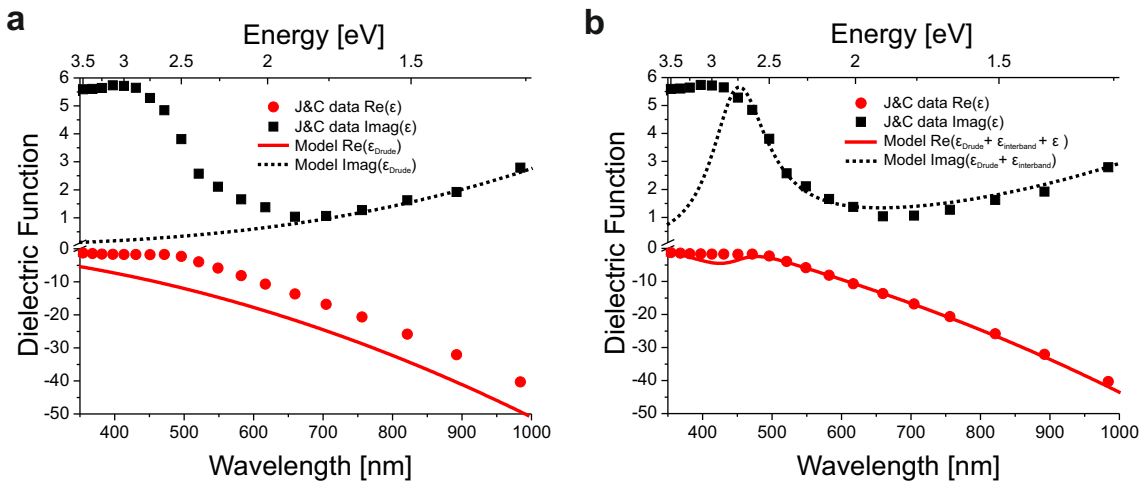

Figure 2.2: Dielectric function of gold. Comparison of experimental data of Johnson and Christy [51] (symbols) and models (lines) with **a** Drude-Sommerfeld model **b** Drude-Sommerfeld model corrected for interband transitions. Model parameters are taken from [50] and are stated in the text.

Within the here presented local description it has been assumed that the induced material polarization depends on the applied external field at the same point in space

and time. In reality the induced polarization will also depend on electric fields at nearby positions and at earlier times. This dependency is taken into account within a non-local description of the dielectric function. Non-local effects are most prominent for very small (few nanometers) metallic particles and for pairs of metallic particles with gaps below one nanometer [52]. In Chapter 4.4 non-local effects are discussed with respect to the investigated nanorod dimers and results from recent publications are stated.

2.1.2 Plasmon resonances of single spheres

In the previous subsection the dielectric function, which fully describes the optical properties of bulk materials, was introduced. For nanoparticles the optical properties not only depend on the material but also on their size. In the case of noble metal nanoparticles for certain geometrical parameters a collective resonant response, i.e. a plasmon resonance, can occur. The plasmon resonance then strongly dominates the optical properties and can lead to enhanced near-field intensities as well as enhanced absorption and scattering of the particle. The spectral properties and their dependence on particle geometries, theoretical modeling and experimental observation of plasmon resonances will be discussed in the following subsections. This subsection starts with the simplest system, a single sphere.

It is possible to analytically calculate the optical response of a spherical particle to a plane-wave illumination. The basic idea is to solve the Helmholtz equation in spherical coordinates by expanding incident as well as scattered field by spherical wave functions, considering the material boundary conditions. This solution strategy is typically denoted Mie theory and a rigorous derivation can be found in various text books [53, 54]. Since the Mie description is fully analytic, it provides an important reference for numerical methods as well as for simple models.

Such a simple model is the quasi-static approximation. Here retardation is neglected and it is assumed that all points on the particle oscillate in phase, which is a good approximation for small systems as demonstrated at the end of this chapter. In this case the Helmholtz equation reduces to the Laplace equation $\nabla^2\Phi = 0$. It turns out that the scattered field of a small sphere with complex dielectric constant ε_m and radius a embedded in a dielectric with real ε_d is the same as for a static dipole located at the center of the sphere [53]. The induced dipole moment $\mathbf{p}$ is related to the external field $\mathbf{E}_0$ via $\mathbf{p} = \varepsilon_0\varepsilon_\mathrm{m}\alpha\mathbf{E_0}$, where α is the polarizability:

$$\alpha = 4\pi a^3 \frac{\varepsilon_\mathrm{m} - \varepsilon_\mathrm{d}}{\varepsilon_\mathrm{m} + 2\varepsilon_\mathrm{d}}. \tag{2.3}$$

The polarizability shows a resonant enhancement for a minimum of $\mathrm{Re}\,[\varepsilon_\mathrm{m}] = -2\varepsilon_\mathrm{d}$, which in the case of gold is fulfilled in the green spectral regime (see also Figure 2.2). In the case of the sphere, typical near-field intensity enhancements are on the order of 20. The near fields are strongly localized to the vicinity of the metal particle and exhibit highest intensities at the air/dielectric interface, which is perpendicular to the direction of the excitation polarization. A numerically calculated field distribution is shown later (Figure 3.8). In experiments near-field distributions can be obtained (or at least estimated) by scanning near-field optical microscopy (SNOM) [6], two

photon photoluminescence (TPL) [7], electron energy loss spectroscopy (EELS) [9], cathodoluminescence (CL) [8] or photo electron emission (PEEM) [55]. However, they often require dedicated setups and the interpretation of the contrast mechanism is often complex. A quantitative measurement of the near-field intensity is even more difficult, but has been claimed for special cases [56, 57].

A simpler (both in terms of experimental setup as well as interpretation) characterization of plasmon resonance can be done by scattering or extinction, i. e. scattering plus absorption, measurements. Scattering is the elastic radiative relaxation of the excited particle, whereas absorption is the non-radiative relaxation. Extinction spectra are typically obtained by measuring the transmission [58–60]. For scattering measurements it is important to suppress the direct reflection by using a dark-field technique [61–63]. A novel dark-field microscope was developed during this thesis and is presented in Chapter 3.2.2.

In order to obtain quantitative magnitudes of scattering and absorption as well as to learn about their dependency on structural parameters, a small analytical study is presented next. Within the quasi-static approximation, a normalization of the above stated polarizability to the excitation source [53] yields the absorption C_{abs} and scattering cross-sections C_{sca}. For a sphere with radius a the cross-sections read as:

$$C_{\mathrm{sca}} = \frac{k^4}{6\pi} |\alpha|^2 \propto a^6 \tag{2.4a}$$

$$C_{\mathrm{abs}} = k\mathrm{Im}\left[\alpha\right] \propto a^3 \tag{2.4b}$$

In Figure 2.3 the absorption and scattering cross-sections for spheres with a diameter of 10 nm and 100 nm are calculated using the quasi-static approximation (equations 2.4) as well as full Mie theory[2]. The cross-sections have been normalized to the geometrical cross-section and therefore represent the scattering and absorption efficiency. For the small sphere absorption dominates over scattering by a factor of more than 500. The efficiencies remain small, which makes it difficult to detect small particles [65]. The resonances occur in the green spectral region at wavelengths of 502 nm and 518 nm for absorption and scattering, respectively. Due to the small size of the sphere the quasi-static approximation is in excellent agreement to the full Mie theory.

For the larger sphere absorption and scattering have the same order of magnitude. For this size the efficiencies are larger than one and on resonance the absorption cross-section is more than twice as large as the geometrical cross-section. The quasi-static approximation clearly deviates from the Mie theory and predicts resonance wavelengths[3] which are smaller than the correct values of 511 nm and 532 nm for absorption and scattering, respectively. In addition, the magnitude of scattering and absorption are underestimated by a factor of 1.5.

[2] In the calculation the dielectric function shown in Figure 2.2b has been used and for the numerical implementation the Matlab script of [64] has been modified to account for a wavelength dependence.

[3] According to equations 2.4 resonance wavelengths do not dependent on the size of the sphere for the quasi-static approximation.

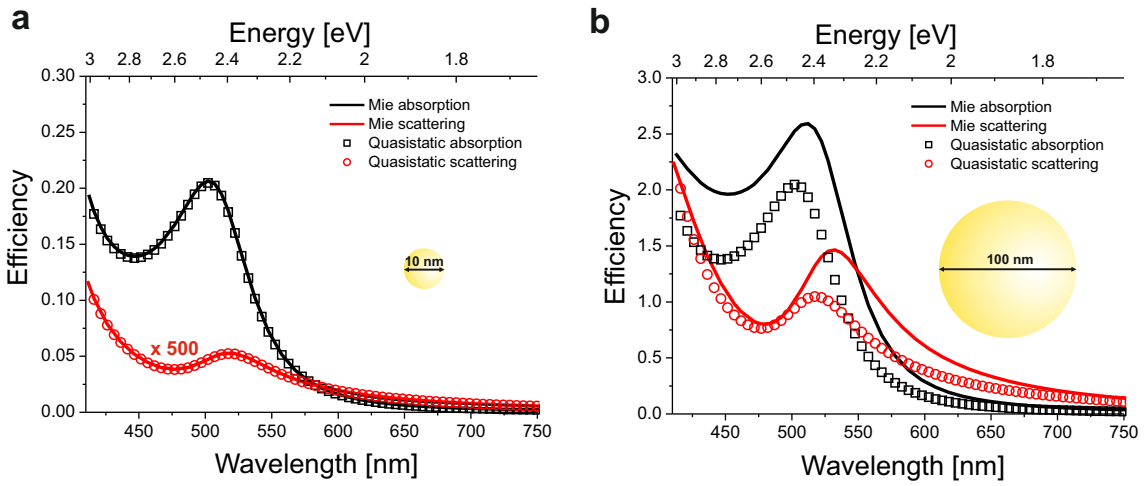

Figure 2.3: Absorption and scattering of gold particles. **a** Scattering (red) and absorption (black) efficiencies of a sphere with a diameter of 10 nm. Scattering is scaled by a factor of 500. Quasi-static approximation (symbols) is in perfect agreement to the full Mie theory (solid lines). **b** Scattering (red) and absorption (black) efficiencies of a sphere with a diameter of 100 nm. Absorption and scattering are of similar magnitude. The differences between quasi-static approximation (symbols) and full Mie theory (solid lines) are clearly visible.

In conclusion, single metallic spheres can show a resonant enhancement of the polarizability, leading to a near-field intensity enhancement as well as absorption and scattering cross-sections which are larger than the geometrical cross-sections. The resonance wavelength only slightly depends on the size of the sphere and occurs in the green spectral region. For practical applications elongated particles are more interesting since their resonance wavelength can be tuned by their geometry and larger near-field intensity enhancements can be achieved, as demonstrated in the next section.

2.1.3 Plasmon resonances of single rods

In this subsection plasmon resonances of elongated nanoparticles are discussed. Nanorods are the basic building block for the structures investigated in this thesis and it is therefore important to understand their resonance in an intuitive way. For this reason a simple Fabry-Pérot model is introduced, which predicts fundamental and higher-order longitudinal resonances. At the end of this chapter the transverse and longitudinal resonances are analyzed in a numerical study and their dependence on rod length as well as the near-field enhancements of the respective modes will be discussed.

Nanorods are elongated particles and exhibit resonances along their short as well as long axis, which are denoted transverse and longitudinal resonance respectively. The transverse resonance does not depend on the length of the rod and shifts only slightly with increasing diameter, which is understood by considering that an extended wire can be modeled as a two dimensional sphere. For a constant diameter the longitudinal

resonance shifts approximately linearly with increasing rod length.

An intuitive approach to the modeling of first and higher order longitudinal modes is provided by the Fabry-Pérot model [66–68]. The basic idea of this model is that a particle with a constant cross-section provides a mode which is guided along the rod. The termination of the rod acts as a mirror and the guided mode will be reflected. Interference of for- and backward propagating modes leads to standing waves, whose resonance wavelengths scale with the length of the cavity.

The guided mode is described by the complex propagation constant $k_{\mathrm{y}}(\omega) = \alpha + i\beta$. The imaginary part of the propagation constant β is related to the effective wavelength $\lambda_{\mathrm{eff}} = 2\pi/\beta$ inside the cavity, which can be significantly smaller than the free space wavelength. The inverse of the real part of the propagation constant α is the decay length, which is the length at which the amplitude of the mode has decreased to $\frac{1}{e}$ of its original value. The reflection at the end of the particle is described by a complex reflection coefficient $\theta(\omega) = |\Gamma(\omega)| e^{i\theta_R(\omega)}$. The real part determines the amount of reflection, whereas the imaginary part introduces an additional phase upon reflection. When the accumulated phase upon a round trip equals 2π forward and backward traveling waves interfere constructively and a standing wave builds up in the cavity of length L. The condition for the resonance then reads:

$$\beta(\omega) L - \theta_R(\omega) = m\pi, \tag{2.5}$$

where $m = 1, 2, 3, ..$ is the order of the resonance. A graphical illustration of the Fabry-Pérot concept is shown in the inset of Figure 2.4a.

Following the procedure described in [69], the propagation constant and reflection coefficient are determined as a function of wavelength, in order to calculate the dependence of the resonance wavelength to the length of the cavity. The modeled system is a gold rod with a diameter of 30 nm, situated in vacuum. The numerical simulations yield a fundamental guided mode with enhanced electric fields for x and z-direction and zero magnetic field along the propagation direction y. The values for the effective wavelength range from 200 nm to 510 nm for excitation wavelength of 600 nm and 1000 nm, respectively. The decay length takes on values between 450 nm and 3000 nm for excitation wavelength of 600 nm and 1000 nm, respectively. The wavelength dependence of the reflection coefficient is less pronounced. Its absolute value is about 0.6 and the phase is about -0.6 rad. In Figure 2.4a the resonance wavelengths are calculated using equation 2.5 and the determined reflection and propagation parameters. An almost linear relationship between rod length and resonance wavelength is observed, in agreement to the linear scaling rule of [70]. However, the model does not provide any information about amplitude or spectral width of the resonance. In addition, from the mass-spring model a resonance along the short (transverse) axis of the rod should occur, which is not predicted by the Fabry-Pérot model.

Finding the resonance position of all modes as well as the values of the near-field intensity enhancements requires a full numerical Finite-Difference-Time-Domain (FDTD) simulations[4] for each rod length. The simulated geometry is identical to the Fabry-Pérot calculation and a total-field-scattered-field source with suitable boundary conditions is used. The values for the resonance wavelengths are shown in Figure 2.4a.

[4]See Chapter 3.2.1 for details on this technique.

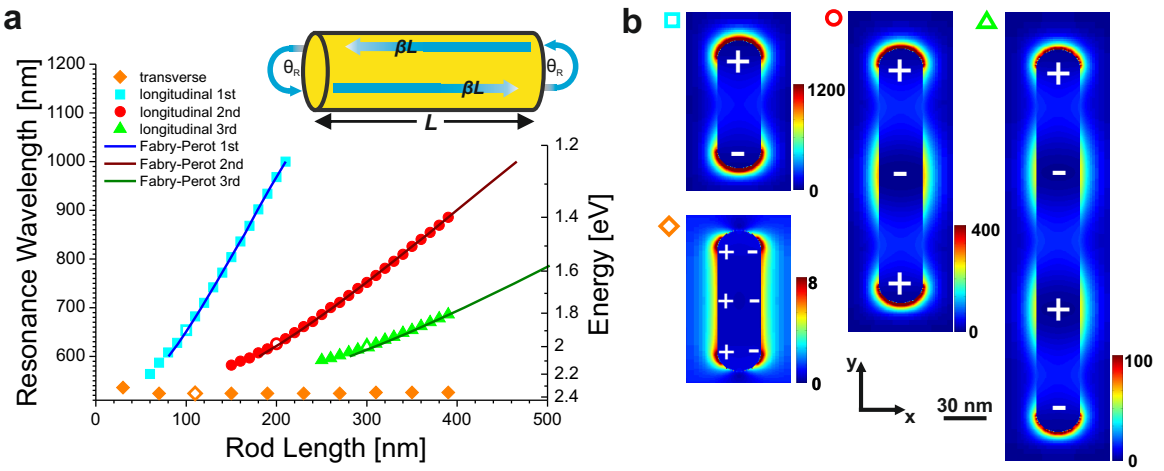

Figure 2.4: Resonances of single rods. **a** Resonance wavelength as a function of rod length. The four observed resonances in the FDTD simulations are the transverse (orange rhombus), 1st order longitudinal (blue square), 2nd order longitudinal (red circle) and 3rd order longitudinal (green triangle) mode. The solid lines are the results from the Fabry-Pérot model. For the open symbols, the near-field distributions are shown. **b** Normalized near-field intensity distributions for the four resonances, as indicated by the open symbols. Plus and minus signs indicate the charge distribution. Note the different color bars.

They are in excellent agreement to the Fabry-Pérot model. In addition, the transverse resonance is observed at a wavelength of 525 nm, exhibiting a small blue shift with increasing rod length. Representative near-field intensity distributions of all modes are shown in Figure 2.4b. As predicted by the Fabry-Pérot model the different orders are characterized by one, two and three nodes in their intensity distribution. The plus and minus signs indicate a snapshot in time of the oscillating charge distribution and reveal the phase relation along the rod.

The smallest intensity enhancement of 10 is found for the transverse resonance. Similar to a single sphere this low value is mainly governed by the strong damping due to interband transitions in the green spectral region. The highest intensity enhancement of roughly 1000 is observed for the first order longitudinal mode. A significantly smaller value of 100 is obtained for the 3rd order mode. This is attributed to the fact that the length of the cavity becomes comparable to the decay length of the guided mode. The 2nd order mode exhibits a symmetric charge distribution and can therefore not be excited by a plane-wave at normal incidence. However, asymmetry can be introduced by a localized excitation source [71] or detector [6] and dark modes of even order can be excited. The achievable near-field intensity strongly depends on the excitation efficiency, which must be taken into account for a quantitative analysis.

2.1.4 Plasmon resonances of coupled particles

Most interesting with respect to intensity enhancement and field confinement are geometries including two nanoparticles. The reason for this is that if brought in close vicinity the particles can couple via Coulomb interaction [72]. The Coulomb interaction causes an additional charge accumulation at the gap between the particles and leads to fields which are strongly localized to the gap. In the mass-spring model this situation would correspond to an additional spring over the gap of the two particles, as depicted in Figure 2.5a,b.

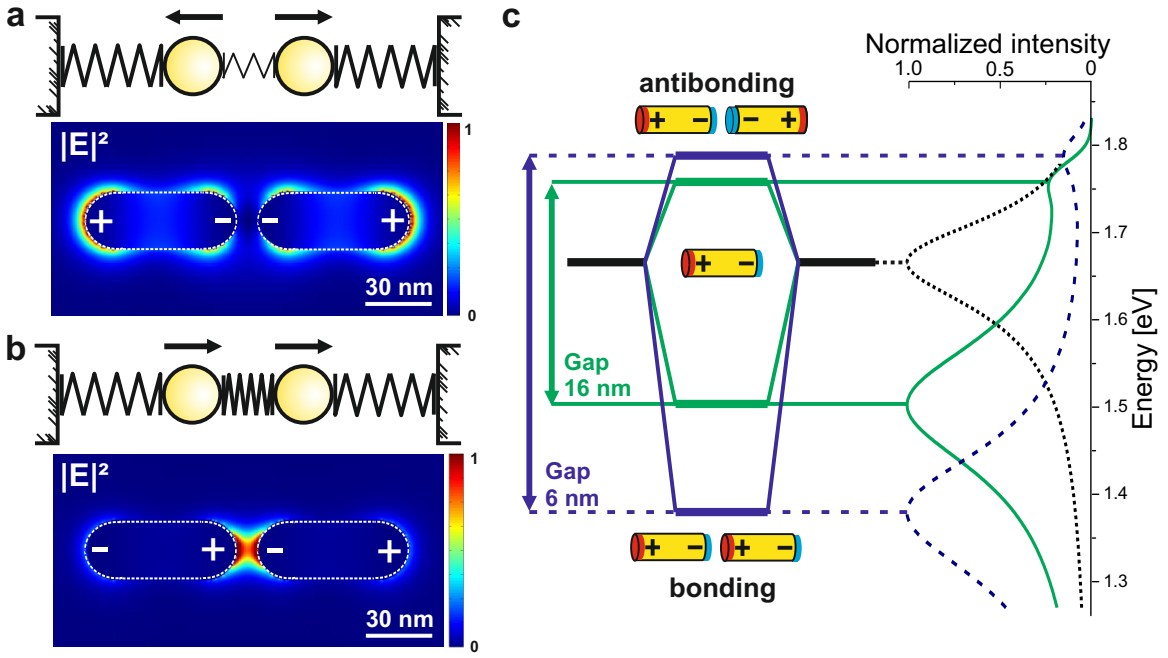

Figure 2.5: Antibonding and bonding resonances of coupled particles. **a** Mass-Spring model and near-field intensity distribution for the out-of-phase charge oscillation, i.e. anti-bonding mode. **b** Mass-Spring model and near-field intensity distribution for the in-phase charge oscillation, i.e. bonding mode. **c** Energy-level diagram of two coupled system with gap sizes of 16 and 6 nm. Adapted from [73].

Similar to two coupled harmonic oscillators the charge distribution on the individual particle can oscillate in and out of phase. This gives rise to two new resonances of the coupled system, i.e. a mode hybridization [74]. In Figure 2.5c the energy level diagram of the two coupled particles is shown for two gap sizes. In analogy to molecular orbital theory the out-of-phase oscillation is called anti-bonding mode and exhibits a symmetric charge distribution with respect to the gap (Figure 2.5a). The resonance energy is larger than that of the single particle. The in-phase oscillation is called bonding mode and exhibits an antisymmetric charge distribution with respect to the gap (Figure 2.5b). The attractive Coulomb force over the gap weakens the restoring force in the individual particles leading to a shift of the resonance to lower energies.

This behavior is different from two coupled harmonic oscillators where the in-phase oscillation has the same resonance frequency as the individual oscillator. It is important to point out that the Coulomb interaction between the two particles scales with the width of the gap. With decreasing gap size, the Coulomb interaction increases, leading to larger shifts of both modes and therefore a larger energy splitting between bonding and anti-bonding mode.

The intensity enhancement maps of the two modes are shown in Figure 2.5a,b. It is clearly visible that strongly enhanced and localized fields are present only for the bonding mode. Due to its symmetry the bonding mode can be excited by a plane-wave and intensity enhancements are typically larger than 1000. It should be noted that the intensity enhancement strongly depends on the gap size and for gaps smaller than 5 nm values exceeding 10000 are possible[5]. Similar to the even modes of single rods the symmetry of the anti-bonding mode does not allow for a plane-wave excitation at normal incidence. Nevertheless, the anti-bonding mode was experimentally observed by a displaced excitation beam [75] or using asymmetric total internal reflection [76].

Besides end-to-end aligned nanorods, the coupling of nanorods has been investigated for various geometries [62, 77]. Of particular interest are side-by-side aligned gold nanorods since they possess various distinguishable symmetric and antisymmetric modes in the visible range [78]. Self-assembly of chemically grown nanoparticles leads to nanometer gaps [79]. Consequently, side-by-side aligned nanorods are exploited for the investigation of atomic-scale confinement of optical fields, presented in Chapter 4.

The understanding of the different modes which can be supported by nanostructures is not only important for this thesis but is also a key requirement for various fields, such as coherent control and Fano resonances. The field of coherent control exploits interference of different modes to control optical fields on a nanometer length and femtosecond time scale [10]. Plasmonic Fano resonances [80] arise from an interference of a spectrally broad (e. g. dipole) mode with a spectrally narrow (e. g. quadrupole) mode and exhibit high quality factors. It is worth noting that simulation results also predict a two times larger quality factor of the bonding mode with respect to the anti-bonding mode. However, this is typically not observed in experiments [73] and is possibly related to surface effects [81]. Only recently a reasonable agreement between experimental and theoretical quality factor was observed for structures fabricated with helium-ion lithography [82].

2.1.5 Coupling of a dipole to a nanoantenna

In this chapter the coupling of a dipole to an optical antenna is investigated in a numerical case study. Three different geometries, a single sphere, a single rod and a gap antenna consisting of two rods are analyzed with respect to their enhancement of decay rates as well as quantum efficiency. An important aspect, which will be specifically discussed, is the intrinsic quantum efficiency of the dipole. This can strongly vary for different types of systems and for example a good fluorescent molecule can have a quantum efficiency of unity, whereas the generation of photons from tunneling

[5]For a quantitative comparison of gap antennas with different gap sizes the reader is referred to the next subsection.

electrons, which is studied in Chapter 6, can be intrinsically quite inefficient. Before the numerical study is presented, the classical and quantum mechanical descriptions of light emitted by a single dipole are stated. An excellent treatment of the coupling of emitters to plasmonic antenna is presented in [4], which has served as a basis for this chapter.

In a classical description the only source term in Maxwell's equation is a current density, meaning that electromagnetic radiation is created by moving charges. The current density $\mathbf{j}$ can be expressed by the sum over individual charges q_n times the velocity of the respective charge $\mathbf{v_n}$. Considering only the lowest-order term of a Taylor series of $\mathbf{j}$ with origin r_0 and assuming a harmonic time dependence the following relation between current density at spatial coordinate $\mathbf{r}$ and dipole moment $\mathbf{p}$ is obtained [50]

$$\mathbf{j}(\mathbf{r}) = -i\omega\mathbf{p}\,\delta\left[\mathbf{r}-\mathbf{r_0}\right]. \tag{2.6}$$

Within the lowest order approximation any current density can therefore be described by a dipole, making this case study valid for a variety of light sources. Continuing the classical description one can derive the radiated power P by a dipole from Poynting's theorem [50]:

$$P = \frac{\omega}{2}\Im\left\{\mathbf{p}^* \cdot \mathbf{E}(\mathbf{r_0})\right\}. \tag{2.7}$$

Here $\mathbf{E}(\mathbf{r_0})$ is the field radiated by the dipole and scattered back to its position. Due to the dot product in equation 2.7 only dipole moments which are orientated along the electric field at the dipole position $\mathbf{E}(\mathbf{r_0})$ need to be considered. This has the important consequence that emitters need to be aligned with respect to the enhanced near-field in order to be affected by it. Spontaneous emission from a two-level system needs to be described in the framework of Quantum-Electro-Dynamics. Starting from Fermi's golden rule and after a lengthy derivation [50] one arrives at the result for the decay rate γ as a function of partial local density of states ρ_p[6]:

$$\gamma = \frac{\pi\omega_0}{3\hbar\epsilon_0}\left|\hat{\mathbf{p}}\right|^2\rho_p(\mathbf{r_0},\omega_0). \tag{2.8}$$

Here $\hat{\mathbf{p}}$ describes the matrix element of the transition between initial and final state.

Using the Green functions formalism it can be shown [50] that, after normalizing to the free-space values γ^0 and P^0, the classical expression (right-hand side) is identical to the quantum mechanical description (left hand side):

$$\frac{\gamma}{\gamma^0} = \frac{P}{P^0}. \tag{2.9}$$

This formula has the important consequence that relative changes of spontaneous decay rates from quantum emitters can be calculated by classical dipoles. The total decay rate in free space is the sum of non-radiative and radiative decay rate $\gamma^0 = \gamma^0_{nonrad} + \gamma^0_{rad}$ and the intrinsic quantum yield is defined as $qe^0 = \gamma^0_{rad}/(\gamma^0_{nonrad} + \gamma^0_{rad})$. The presence of an antenna has strong influence on the emitting properties of the dipole. The antenna modifies its radiative decay rate and therefore influences the

[6] For isotropic and homogenous media and if the quantum system has no fixed dipole axis the partial local density of states is identical to the total local density of states [50].

number of photons which can be emitted per unit time. Since metals are lossy an additional non-radiative decay channel γ_{loss} is opened up and these photons are lost. The analysis considers the low power excitation regime and neglects saturation effects, which is an adequate description for the light generation from inelastically tunneling electrons. For the moment $qe^0 = 1$ is assumed, leading to an overall quantum efficiency QE= $\gamma_{rad}/(\gamma_{loss} + \gamma_{rad})$.

To obtain a quantitative understanding, the radiative and non-radiative decay rate are calculated by FDTD simulations. In the simulation the intrinsic quantum yield of the dipole is 1 and the emitted and absorbed power are calculated by integrating the Poynting vector over the surface of a closed box of monitors. As illustrated in Figure 2.6a three antenna geometries are studied. A single sphere with a diameter of 60 nm, a single rod with a length of 130 nm and a gap antenna consisting of two rods, each with a length of 100 nm. The normalized decay rates at the wavelength of the plasmon resonance are calculated for different dipole distances. Note that in the case of the antenna this results in a change of gap size. The plasmon resonance of the sphere is at 543 nm and the plasmon resonance of the rod is at 747 nm. The resonance of the antenna strongly depends on the gap size and varies from 671 to 739 nm for the investigated gaps ranging from 52 to 3 nm. In Figure 2.6b the obtained results are plotted. A general trend for all structures is an increase of decay rates for a decrease in dipole distance. The largest radiative decay rates are observed for the antenna with smallest gap and take on values of 10^5. The increase in radiative decay rate shortens the lifetime of the dipole and more photons are emitted per time, compared to the free-space value. If the emitter is below saturation this does not result in an increase of the total number of emitted photons. The efficiency of the photon emission is determined by the ratio of radiative rate to the total decay rate. The quantum efficiency as a function of dipole distance is shown in Figure 2.6c. For the case of the sphere the quantum efficiency decreases with smaller dipole distance and for a dipole distance of 1 nm the quantum efficiency is only 2 %. The rod can maintain a 50 % quantum efficiency down to dipole distances of 4 nm. In the case of the gap antenna the QE remains at 60 % even at smallest dipole distance. These results reflect that it is not possible to improve the emission of a emitter with a quantum efficiency of unity, when it is excited below saturation. In this regime an enhancement is only possible for optical excitation, where absorption can be increased by enhanced optical near-fields.

However, the situation drastically changes for dipoles with a low intrinsic quantum efficiency, which are analyzed next. Using the definition $qe^0 = \gamma^0_{rad}/(\gamma^0_{nonrad} + \gamma^0_{rad})$ it is possible to rewrite the overall quantum efficiency in the following form:

$$\mathrm{QE} = \frac{\gamma_{\mathrm{rad}}/\gamma^0_{\mathrm{rad}}}{\gamma_{\mathrm{rad}}/\gamma^0_{\mathrm{rad}} + \gamma_{\mathrm{loss}}/\gamma^0_{\mathrm{rad}} + (1 - \mathrm{qe}^0)/\mathrm{qe}^0)}. \tag{2.10}$$

For a dipole with $qe^0 = 1$ the term on the right-hand side of the denominator vanishes and equation 2.10 becomes identical to the expression stated earlier. However, for very low quantum efficiencies this term can become large. Assuming $qe^0 << 1$, it is possible to recast equation 2.11 into:

$$\mathrm{QE} = \frac{1}{\gamma_{\mathrm{loss}}/\gamma_{\mathrm{rad}} + \gamma^0_{\mathrm{rad}}/(\mathrm{qe}^0\gamma_{\mathrm{rad}})}. \tag{2.11}$$

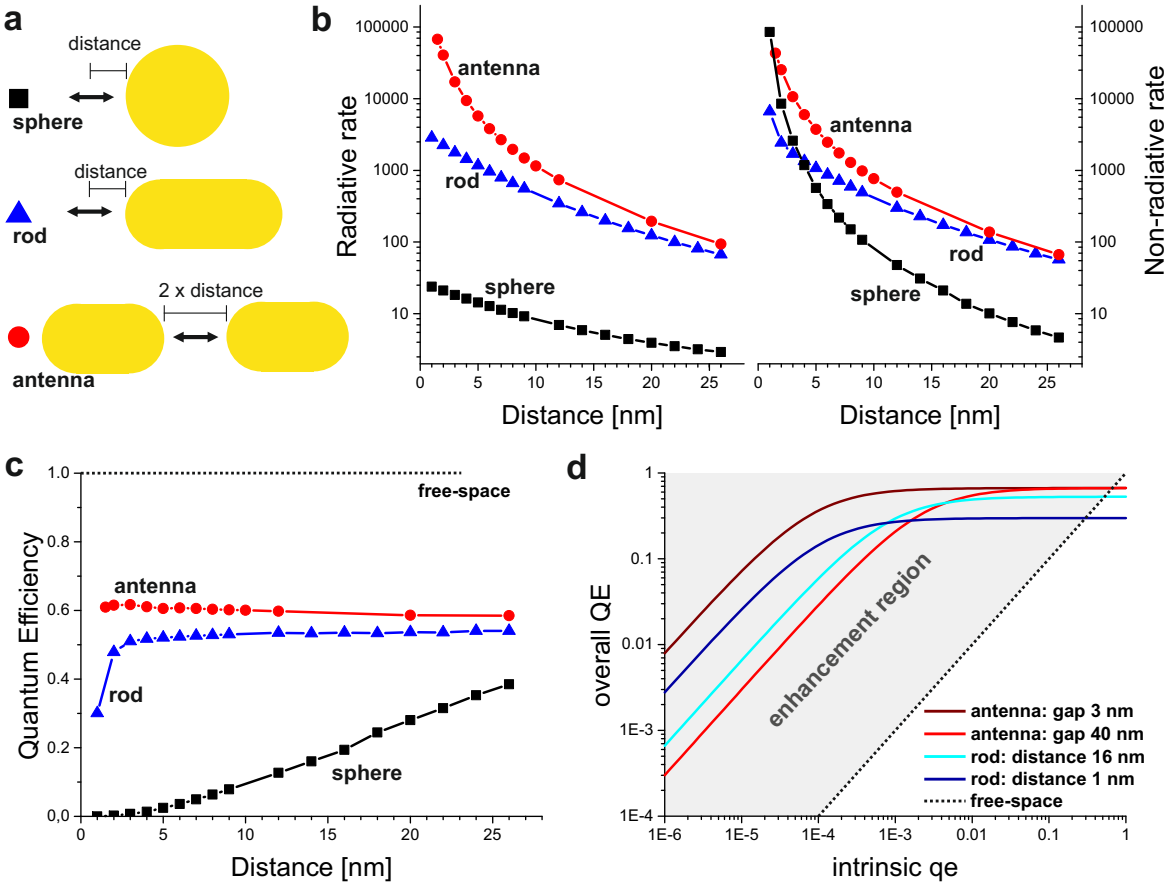

Figure 2.6: Coupling of a dipole to different nanoantennas. **a** Sketch of the antenna geometries and definition of dipole distance. **b** Radiative and Non-Radiative Rates calculated at the respective resonance wavelength. **c** Quantum efficiency for an emitter with intrinsic quantum efficiency of 1. **d** Dependence of intrinsic quantum efficiency of the exciting dipole on total quantum efficiency.

From this equation it becomes clear that for dipoles with a low intrinsic efficiency not only the ratio between radiative and non-radiative rates is important, but that a large radiative decay rate can compensate a small value of intrinsic quantum efficiency.

Using equation 2.11 as well as the parameters obtained from the FDTD simulations it is possible to see this effect in a quantitative way. In Figure 2.6d the overall quantum efficiency is calculated as a function of the intrinsic efficiency of the emitting dipole. Four geometries are compared: a dipole in the gap of antennas with a gap width of 40 nm and 3 nm as well as a dipole placed 16 nm and 2 nm away from a single rod. In addition, the corresponding curve of a free-space dipole is shown. For emitters with an intrinsic efficiency qe^0 close to unity there is not much to improve and the overall quantum efficiency is decreased due to loss in the metal. However, for less efficient emitters the enhanced radiative decay rate can compensate a low intrinsic efficiency. The presence of the antenna increases the overall quantum efficiency when

the intrinsic efficiency is lower than 0.7. For an intrinsic efficiency lower than 0.1 all structures provide an enhancement of the overall quantum efficiency. The antenna with small gap shows the highest overall efficiency. The efficiency of an intrinsically inefficient dipole ($qe^0 = 1^{-4}$ or lower) can be enhanced by three orders of magnitude when it is coupled to an antenna.

The conclusion of this chapter is that the enhancement of emitters, such as molecules, quantum dots or tunneling electrons, strongly depends on the choice of the antenna. Especially for emitters with low intrinsic quantum yield, gap antennas show by far the best performance in terms of quantum efficiency as well as radiative rates. This is also reflected in the fact that the so far highest fluorescence enhancement of >1000 was observed for the coupling of a poorly emitting molecule (qe^0=0.025) to a bow-tie antenna [22]. A series of experiments studying the fluorescent enhancement of emitters coupled to plasmonic structures has been conducted by the Novotny group and is summarized in a review by this group [4]. It should be noted that the discussion presented here assumes a low excitation power far from saturation. In the high power regime the excited-state of the intrinsic emitter is saturated and sets a limit to the amount of radiated photons. In this regime the increase of radiated decay rate by the antenna causes a faster depopulation of the excited state and one can extract much more photons per time.

In Chapter 6 an optical antenna is excited by inelastically tunneling electrons. Fluctuations in the tunneling current constitute a spectrally-broad emitter and the dipole moment is naturally aligned with respect to the antenna. For these reasons all values stated in this chapter have been calculated at the respective antenna resonance wavelength and for dipoles, which are aligned with respect to the dominating field component of the enhanced near-field. For other dipole orientations or wavelengths the decay rates will be drastically lower.

2.2 Electronics

In this thesis a platform for efficient electro-plasmonic devices is developed using a planar gold-SiO_2-gold junction, which was designed to provide distinct plasmonic resonances (Chapter 5). By placing gold nanoparticles in between the gold electrodes a tunneling junction is constructed and electrons tunneling inelastically through this junction couple to the plasmonic mode and emit light (Chapter 6). For the discussion of these studies it is important to provide a solid background on the electrical conduction in such systems, which will be the goal of this chapter. The first part treats the conduction mechanisms in a rather general way and is based on [83, 84]. This section starts with the basics of metal-insulator contacts before discussing the bulk- and electrode-limited conduction mechanisms and their corresponding current-voltage characteristics. The second part of this chapter treats the topic of electron tunneling in detail. The different tunneling regimes are presented and the derivation of a general current-voltage characteristic is outlined. In order to keep the relation simple, approximations on the barrier shape are necessary and their error is estimated. The chapter finishes by reviewing experimental results of Au-air-Au tunneling junctions.

2.2.1 General conduction mechanisms

The conduction mechanism in a metal-insulator-metal (MIM) system is not necessarily determined solely by the insulator, since the interaction between insulator and metal electrode can play an important role. One can specify two groups of conduction processes: *electrode-limited* and *bulk-limited*. For electrode-limited conduction a potential barrier is established at the interface between insulator and electrode and the current will be limited by the rate electrons can flow over the interfacial barrier. In the case of bulk-limited conduction the charge carriers are generated at the metal-insulator interface. The electrons therefore do not need to overcome the barrier and the current is limited by the rate the electrons can flow through the insulator.

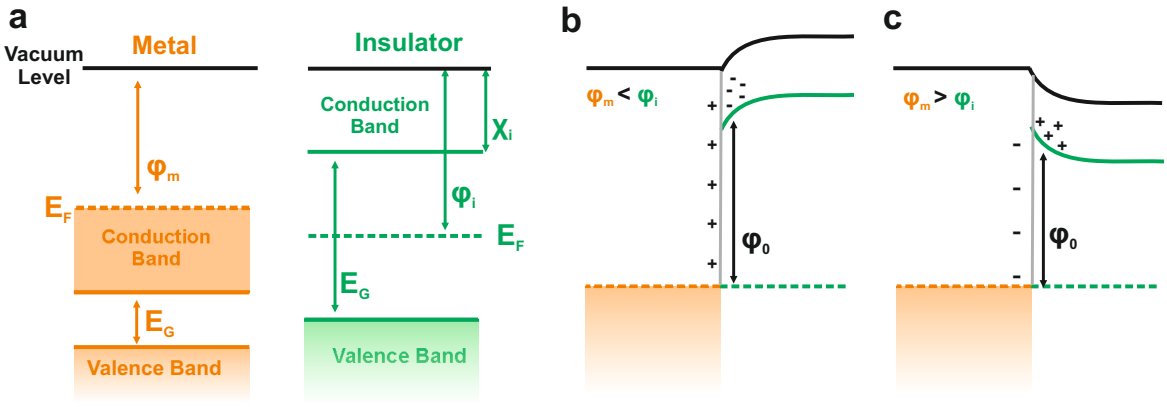

Figure 2.7: Energy diagrams illustrating different types of metal-insulator contacts. **a** Schematic energy diagrams of an isolated metal and an isolated insulator. **b** Ohmic contact. **c** Blocking contact.

Before discussing the different types of contacts it is worth to recall the energy levels of an isolated metal electrode and an isolated insulator. A simplified sketch of the energy levels is shown in Figure 2.7a. The energy level structure of (crystalline) solids is governed by bands of electronic states and by regions without states. The occupation of these states is determined by the Fermi-Dirac distribution and at zero temperature only states below the Fermi Energy E_F are occupied, as indicated by the shaded regions in Figure 2.7a.

A metal is characterized by the fact that the Fermi Energy falls within a band, which is therefore only partly filled. This band is called conduction band, since it is responsible for the electrical conductivity. For the case of gold the Fermi Energy is about 5 eV.

An insulator is characterized by a completely filled valence band which is separated by a large bandgap from the completely empty conduction band. The width of the energy gap E_g is about 9 eV in the case of SiO_2. At zero temperature the Fermi level of an intrinsic insulator is exactly in the middle of the energy gap. Another important quantity is the electron affinity χ_i, which is the energetic distance between the lower edge of the conduction band and the vacuum level. The electron affinity of SiO_2 is about 1 eV.

Bringing metal electrode and insulator in contact leads to the formation of a potential barrier at the interface, since in equilibrium and without an applied voltage, Fermi levels will line up and be continuous across the interface. The height of the barrier at the interface is given by $\varphi_0 = \varphi_m - \chi_i$. However, it is not the height of this barrier but the type of contact which determines the conduction process. Depending on the relative work functions of the metal electrode φ_m and of the insulator φ_i the type of contact can be *ohmic*, *blocking* or *neutral*.

In the case of a *neutral contact* the work function of metal and insulator are equal. Vacuum and Fermi level align naturally and the energy levels are identical to the ones of the isolated materials.

An *ohmic contact* requires the work function of the electrode to be smaller than the work function of the insulator. Electrons are then injected from the metal into the conduction band of the insulator in order to satisfy thermal equilibrium requirements. Consequently a space charge region is formed and the conduction band bends upwards, as depicted in Figure 2.7b. The region where negative charges accumulate extends into the insulator and can act as a charge reservoir. Consequently electrons do not need to overcome the interfacial barrier and the conductivity is therefore limited by the rate electrons can flow through the insulator, i.e. *bulk-limited*.

If the work function of the metal electrode is larger than the work function of the insulator a *blocking contact* occurs. In this case electrons flow from the insulator to the metal electrode. The space charge region in the insulator is consequently positively charged and causes a downward bending of the conduction band, as shown in Figure 2.7c. However, for an intrinsic insulator the amount of electrons is very small and the conduction band can be assumed to be flat. Nevertheless, the free electron concentration at the interface is much lower than in the bulk of the insulator and the conduction in the system is limited by the rate electrons can flow over the barrier at the interface between metal and insulator, i.e. *electrode-limited*.

In the following, the *bulk-limited* conduction processes, i.e. **ohmic** conduction,

space-charge-limited conductivity, **hopping** and **Poole-Frenkel** conductivity, as well as *electrode-limited* conduction processes, i.e. **Schottky** (thermionic) emission and **electron tunneling**, are briefly discussed. Illustrational sketches of the different mechanism are shown in 2.8a-e.

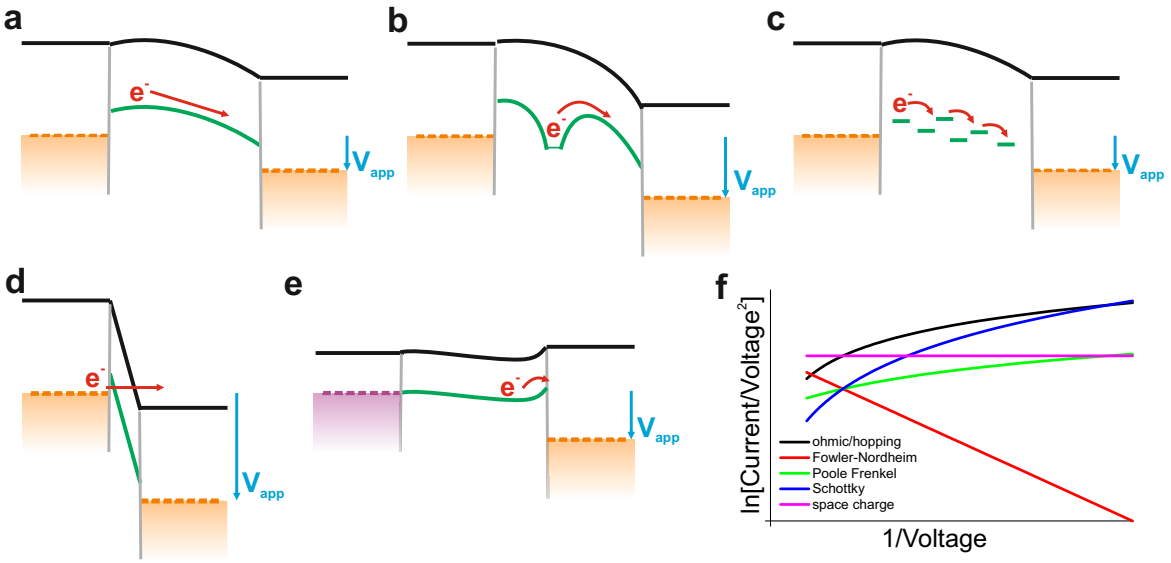

Figure 2.8: Schematic illustration of conduction mechanisms in metal-insulator-metal junctions. The conduction is either bulk-limited: **a** space-charge limited conduction, **b** Poole-Frenkel effect, **c** hopping, or electrode-limited: **d** electron tunneling, **e** Schottky emission. For the case of Schottky emission the typical situation of one ohmic and one blocking contact is illustrated. **f** Schematic current-voltage characteristics of the various conduction mechanisms in a Fowler-Nordheim plot.

Bulk-limited conduction requires an ohmic contact between electrode and insulator. If the insulator is sufficiently thin, the accumulation regions formed at both metal-insulator contacts overlap and an electric field, i.e. a space charge, extends throughout the insulator. For low voltages, when the injected electron concentration is lower than the thermally generated carrier concentration n_t, the conduction is **ohmic** and the current density scales linearly with the applied voltage

$$J = n_t e \mu \frac{V}{d} \propto V, \tag{2.12}$$

where e is the elementary charge, μ the mobility and d the thickness of the insulator. If the applied voltage is large enough, such that the injected electron concentration is larger than the thermally generated concentration, a transition from ohmic to **space-charge-limited** (SCLC) conductivity occurs (e.g. in CdS [85] or Sb_2S_3 [86] films). The SCLC current scales quadratically with the applied voltage and, for a trap-free material, is given by

$$J = \frac{9}{8} \epsilon_0 \epsilon r \mu \frac{V^2}{d^3} \propto V^2, \tag{2.13}$$

where ϵ_0 and ϵ_r are free-space and material permittivity, respectively. For further information, such as the inclusion of trap states, the interested reader is referred to the literature [84, 87, 88].

Impurity states also play an important role in the second bulk-limited conduction process which is governed by the **Poole-Frenkel** effect. Electrons located at impurity centers cannot contribute to conduction unless they are promoted to the conduction band. If a significantly large electric field is applied, the Coulombic potential barrier between positively charged trap state and conduction band edge is lowered by an amount $\Delta\psi_{PF} = \beta_{PF}E$, where E is the applied electric field and β_{PF} the Poole-Frenkel field-lowering coefficient. Electrons can escape through the reduced potential into the conduction band and contribute to conduction. The lowered potential increases the current density by an exponential factor such that

$$J = J_0 \exp(\frac{\beta_{PF}\sqrt{V}}{kT\sqrt{d}}) \propto V \exp(\sqrt{V}), \tag{2.14}$$

where d is the insulator thickness and $J_0 = \sigma_0 E$ is the low-field current density. Poole-Frenkel conduction is (at high fields and high temperatures) widely observed in insulators such as silicon oxide [89–91] as well as silicon nitride [92]. It should be noted that the Poole-Frenkel effect can be easily confused with the Schottky effect due to its similar current-voltage characteristic [93].

The last *bulk-limited* conduction process presented in this chapter is **hopping** of electrons between localized electron levels. Localized states are typical for non-crystalline materials and arise from a missing long-range order, voids, defects or impurities. Since these localized states are closely spaced, hopping requires only small amounts of thermal energy, i.e. it can occur at very low temperatures. Different varieties of hopping are observed [94] and the respective conductivity exhibits a characteristic temperature dependence. For nearest-neighbor hopping the conductivity is $\sigma \propto \exp[-T^{-1}]$. For variable-range hopping (here hops occur to levels which are on average further than to the nearest neighbor but have a smaller energy difference) the conductivity is $\sigma \propto \exp[-T^{-1/4}]$. Since the conductivity is independent of the applied voltage the current density scales linear with the applied voltage

$$J = \sigma\frac{V}{d} \propto V. \tag{2.15}$$

Hopping conduction has been observed in various materials [94] including SiO_2 films, which contain C, Si, and Ge clusters [95].

Schottky or thermionic emission is an *electrode-limited* conduction process, which is dictated by a field-assisted lowering of the potential barrier at the metal electrode. Similar to the Poole-Frenkel effect the current density increases exponentially with the reduced potential and is given by

$$J = AT^2 \exp(-\frac{\varphi_0}{kT}) \exp(-\frac{\beta_S\sqrt{V}}{kT\sqrt{d}}) \propto \exp(\sqrt{V}), \tag{2.16}$$

where A is the Richardson constant and β_S the Schottky coefficient. The Schottky effect plays an important role in semiconductor diodes as well as for thermionic electron

emitters. In order to work efficiently these devices often exploit an ohmic as well as a blocking contact. Experimental observation of Schottky emission using symmetric MIM geometries has been claimed for Al-Al_2O_3-Al [96], Cu-SiO/SnO_2-Cu [97] as well as W-Air-Au [98] junctions.

Electron tunneling is a quantum-mechanical effect. It arises from the fact that for very thin insulating films the electron wave function can extend through the insulator. This leads to a finite probability for the electron to traverse the barrier. Applying a voltage to the tunneling junction leads to a deformation/tilting of the barrier and for high voltages, i.e. larger than the potential barrier φ_0, the barrier width is reduced. This is the regime of Fowler-Nordheim tunneling or field emission. The current-voltage characteristic is given by:

$$J = \frac{2.2e^3V^2}{8\pi h\varphi_0\Delta s^2}\exp(-\frac{8\pi\sqrt{2m}d\varphi_0}{3heV}) \propto V^2\exp(-\frac{1}{V}), \tag{2.17}$$

where Δs is the effective barrier width and φ_0 the barrier height. Electron tunneling will be discussed in more detail in the next chapter. Three different tunneling regimes are identified and the effect of image charges will be discussed.

So far ideal structures have been considered. However, it must be noted that in reality surface states can exist in the energy gap of the metal or the insulator. Surface state arise from the lack of translational symmetry at the interface even for a perfectly clean material. If in addition adsorbents or defects are present at the interface, the situation gets even more complex since adsorbents can influence surface states as well as work functions. A detailed presentation of these effects goes beyond the scope of this thesis and the interested reader is referred to standard text books [99–101]. Another effect is the formation of conductive pathways within the insulating SiO_2 [102, 103], leading to the observation of resistive switching, negative differential resistance and current hysteresis [104]. Moreover, it was found that the surface conductivity of silicon dioxide strongly depends on the humidity in the surrounding air [105, 106].

Consequently, care must be taken when analyzing the electrical conductivity. However, if stable and reproducible current-voltage characteristics are obtained, their specific shape is a good indicator of the conduction mechanism within the respective voltage range. For example, in Figure 2.8f the current-voltage characteristics of various conduction mechanisms are compared in a Fowler plot, i.e. $ln(I/V^2)$ vs. $1/V$. It is clearly seen that the only mechanism exhibiting a negative slope is the Fowler-Nordheim tunneling.

2.2.2 Electron tunneling

The goal of this chapter is to derive an expression relating the tunneling current through a thin insulator to the applied voltage. For modeling experimental data a simple expression is desired, which requires various assumptions on the barrier shape. The derivation presented here follows the standard Simmons model [107] and the work by Baldea and Köppel [108], which critically reviews the Simmons model. Three regimes of electron tunneling: direct, quasi-Fowler-Nordheim and Fowler-Nordheim tunneling are discussed. It is shown that the error introduced by the WKB *(Wentzel-Kramers-Brillouin) approximation* and Simmons approximation is much smaller than

the inclusion of (classical) image charge effects. In the last part an overview is given how tunneling junctions can be realized in experiments and how the results compare to the theoretical predictions.

In quantum mechanics the motion of an electron is given by its wave function, as described by Schrödinger's equation. In the case of two metal electrodes separated by a thin insulating gap the wave function can exponentially decay inside the gap and there is a finite probability for the electron to penetrate the barrier. The energy diagram of an unbiased metal-insulator-metal tunneling junction is sketched in Figure 2.9. For the following discussion the barrier is assumed to be in x-direction and the energy-dependent transmission probability will be denoted $D(E_x)$.

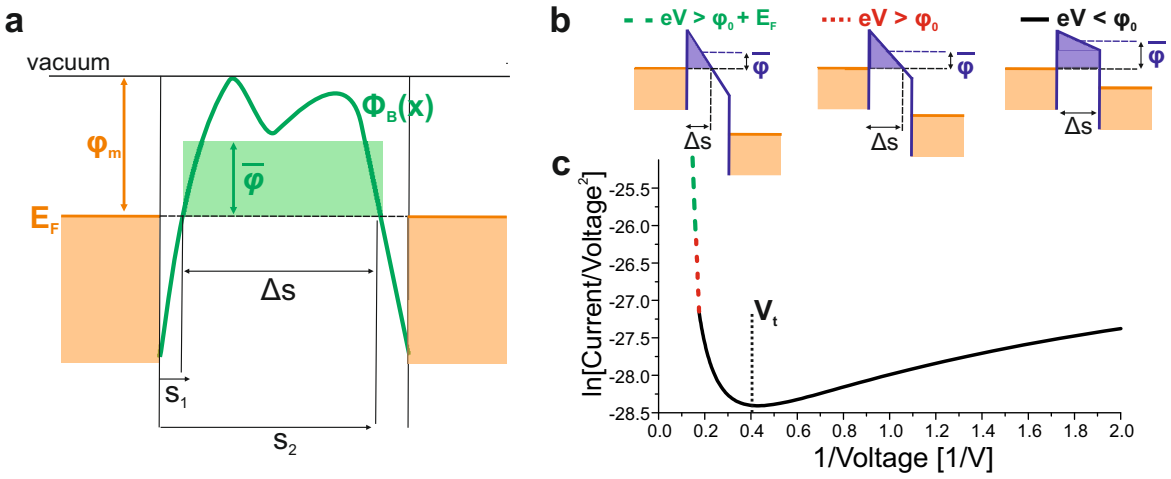

Figure 2.9: Regimes of electron tunneling. **a** Schematic illustration of a metal-insulator-metal tunneling junction. **b** Illustration of the three different regimes of direct tunneling (black solid line), quasi Fowler-Nordheim tunneling (red dotted line) and Fowler-Nordheim tunneling (green dotted line). **c** Analytically calculated current-voltage characteristic for the three different tunneling regimes.

Putting the right electrode at a negative potential eV_{app} with respect to the left electrode leads to a respective lowering of the Fermi Energy of the right electrode. Free states become available for electrons to tunnel into and a net current flows through the barrier. The current density can be expressed as [107]

$$J = \frac{4\pi me}{h^3}\left(eV_{app}\int_0^{E_F-eV_{app}} D(Ex)dE_x - \int_{E_F-eV_{app}}^{E_F} E_x D(E_x)dE_x\right). \qquad (2.18)$$

Even though no assumptions were made on the barrier shape so far, the above formula is valid only for zero temperature, a parabolic conduction band dispersion and an elastic tunnel process. The transmission probability $D(E_x)$ is not straightforward to calculate and a popular approach is to use the WKB which assumes the potential barrier $\Phi_B(x)$ to be a slowly varying function. Within the WKB approximation the

transmission probability is given by:

$$D(E_x) = \exp\left[-\frac{2}{\hbar}\int_{s_1}^{s_2}\sqrt{2m(E_F + \Phi_B(x) - E_x)}dx\right]. \tag{2.19}$$

Due to the square root this equation can still not be solved analytically. Within the so called *Simmons approximation* one replaces the complex barrier $\Phi_B(x)$ by a rectangular-shaped barrier (see Fig 2.9a for illustration of parameters) of width $\Delta s = s_2 - s_1$ and a mean height $\bar{\varphi}$ of

$$\bar{\varphi} = \frac{1}{\Delta s}\int_{s_1}^{s_2}\Phi_B(x)dx. \tag{2.20}$$

With this assumption it is possible to integrate equation 2.20 and subsequently equation 2.19 analytically, leading to the final expression relating current I and applied voltage V_{app} as a function of the mean barrier height $\bar{\varphi}$

$$I = C_s J_0\left\{\bar{\varphi}\,\exp(-A\sqrt{\bar{\varphi}}) - (\bar{\varphi} + eV_{app})\cdot\exp(-A\sqrt{\bar{\varphi} + eV_{app}})\right\}. \tag{2.21}$$

Here, C_s is the tunneling cross section, $A = 4\pi\beta\Delta s/h\sqrt{2m}$ and $J_0 = e/2\pi h(\beta\Delta s)^2$. The correction factor β describes the deviation to the actual potential and is typically close to unity. The first term in equation 2.21 can be considered a current flowing from the left to the right and the second term a current flowing from right to left electrode. Even though some approximations were necessary, the advantage of equation 2.21 is that it can be applied to any barrier shape once the mean barrier is known. Vice versa the mean barrier height can be deduced, if the current-voltage characteristic is known.

From equation 2.21 it becomes clear that the tunneling current depends on the applied voltage V_{app} and the width Δs and height $\bar{\varphi}$ of the potential barrier. However, under an applied voltage the rectangular-shaped (Simmons approximation) potential barrier becomes triangular $\Phi_B = \varphi_0 - (eV_{app}\cdot x/s)$, where φ_0 is the unbiased barrier height. Consequently, the barrier width and height are voltage-dependent and one can identify three different regimes: **direct tunneling**, **quasi Fowler-Nordheim tunneling** and **Fowler-Nordheim tunneling**. The energy levels of the three regimes indicating barrier width Δs as well as mean barrier height $\bar{\varphi}$ are sketched in Figure 2.9b. As discussed in the previous chapter, conduction mechanisms can be distinguished in Fowler Nordheim plots ($\log[I/V]$ as a function of $1/V$). For this reason it is worth to discuss the current-voltage characteristics of the three regimes in a Fowler Nordheim plot (Figure 2.9c). For the calculation of the tunneling I-V characteristic a barrier height of $\varphi_0 = 5$ eV, a tunneling cross-section of C_s=1 nm^2 and a tunneling gap of s=0.8 nm have been used.

Direct tunneling occurs for low voltages $V < \varphi_0/e$, where the barrier is only slightly tilted. The barrier width is equal to the width of the insulator $\Delta s = s$ and the mean barrier height is given by $\bar{\varphi} = -eV_{app}/2 + \varphi_0$. In this regime the Fowler characteristic changes from a positive to a negative slope at the transition voltage V_t.

For larger voltages $V > \varphi_0/e$, the barrier is significantly tilted and the barrier width is reduced to $\Delta s = s\varphi_0/eV_{app}$. Integrating equation 2.20 over this width leads to a mean barrier height of $\bar{\varphi} = \varphi_0/2$. For the barrier parameters used, the current flowing

from left to right is much larger than the current from right to left and the Fowler characteristic has an almost constant negative slope. In the literature this regime has no distinct name, but will be called **quasi Fowler-Nordheim tunneling**, due to its similar current-voltage characteristic.

In the case of very high voltages $V_{app} > (\varphi_0 + E_F)/e$ the Fermi Level of the right electrode is situated below the conduction band of the left electrode. Consequently tunneling from the left to the right electrode is not possible since there are no available states in the energy gap. Therefore the right hand side of equation 2.21 is zero. This is the only difference to the quasi Fowler-Nordheim regime and barrier width and height are given by $\Delta s = s\varphi_0/eV_{app}$ and $\bar{\varphi} = \varphi_0/2$ as in the quasi Fowler-Nordheim regime. The obtained current-voltage characteristic $I \propto V^2 \exp[\frac{1}{V}]$ is fully linear in the Fowler-Nordheim plot. This situation is identical to field emission from a metal tip, i.e. **Fowler-Nordheim tunneling**.

So far the interaction of the tunneling electron with the two metal surfaces has been neglected. In a classical approach this interaction can be described by an image potential. The effect of the image potential is to round off the corners of the barrier and reduce its width. Simmons approximates the potential to[7]:

$$\varphi(x) = \varphi_0 - \frac{eVx}{s} - \frac{1.15\lambda s^2}{2x(s-x)}. \tag{2.22}$$

In Figure 2.10a the potential barrier (gold-vacuum-gold) is calculated within the Simmons approximation for an applied voltage of 2.12 V, a work function of 5.7 eV and a vacuum gap of 0.8 nm. For this choice of parameters the approximation of Simmons is in good agreement to the exact solution (taken from [108]), however it diverges for x=0 and x=s. The effect of including image charges on the current-voltage characteristic is elucidated in Figure 2.10b, where the Fowler characteristics are plotted with (dashed lines) and without (solid lines) image charges. The main effect of including image charges is a drastic increase in current, whereas the overall shape of the characteristic is only slightly affected. In addition, Figure 2.10b shows the effect of the WKB and Simmons approximation on the Fowler characteristic. The data for the exact solution and WKB approximation are taken from [108] and the Simmons approximation has been calculated using equation 2.21 and applying equation 2.20 and 2.22, respectively. In order to allow for a comparison, the values from [108] (φ_0=5.7 eV, s=0.8 nm and Cs=19 nm^2) have been adopted. From Figure 2.10b it becomes clear that deviations introduced by the Simmons approximation are comparatively small. Consequently, throughout this thesis the Simmons approximation will be used.

On the other hand, the inclusion of image charges strongly affects the absolute values of the current-voltage characteristic. However, the inclusion of image charges in the form of equation 2.22 is a classical description from which multiple problems arise [110]. First, the image potential diverges when the charge come close to the electrode, as can be seen in Figure 2.10a. This is unphysical since the potential energy inside a conductor is finite. Second, the classical calculation is stationary and retardation, i.e. a finite response time of the electron gas to the moving charge, is neglected. Including the interaction of the tunneling electron with the barrier in a quantum mechanical

[7] In [109] it is noted that a factor of two is missing in the original work [107].

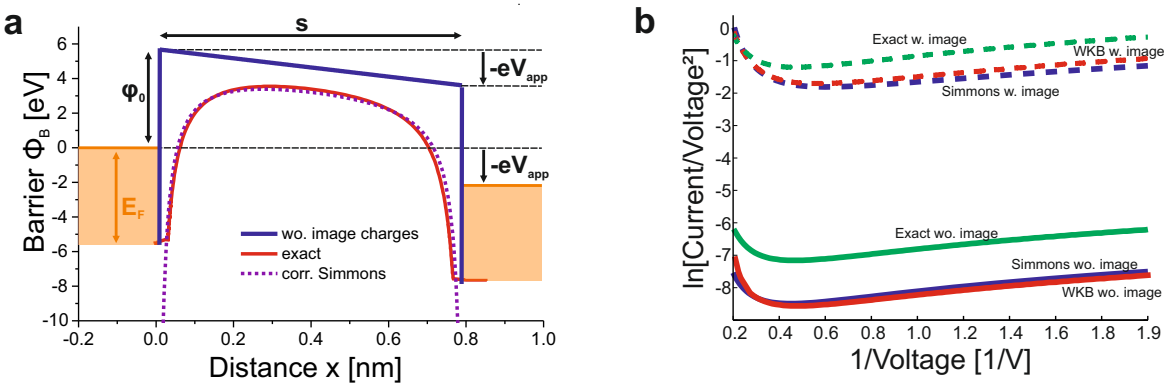

Figure 2.10: Effects of approximations and image charge effects on tunneling. **a** Barrier height as a function of distance for a barrier without image charges (solid blue line), a barrier within the Simmons approximation including image charges (dashed magenta line) and the exact barrier (solid red line). **b** Influence of WKB and Simmons approximation on the Fowler characteristic. For dashed/solid curves the calculation is with/without image charge effects. The data for the exact shape and for WKB approximation have been taken from [108].

framework can be a solution to these issues. Further information on these quantum corrections can be found in [108, 110] and the references therein. Most importantly the corrections cause the barrier to be finite at the position of the electrodes and weaken the effect of image charges. An incorporation of quantum corrections is not straightforward and it is difficult to estimate their effect for the junctions investigated in this thesis. For this reason all current-voltage characteristics are fitted with and without the inclusion of image charges, which allows to estimate the error introduced by the classical treatment.

In the last part of this chapter different tunneling junction geometries are presented and typical results for the observed current-voltage characteristics are stated. In particular, the reported barrier heights and the effect of image charges will be discussed. Probably, most tunneling experiments are performed by using a scanning tunneling microscope (STM), in which a vertical junction is formed between the moveable metal tip and the sample surface. Planar tunneling junctions can be realized with mechanically controlled break junctions (MCBJ) or by exploiting electromigration. Junctions formed by electromigration do not require bulky setups and can be possibly integrated into nanoscale circuits. On the other hand STM and MCBJ allow for a dynamic control of the tunneling distance which is important to gain insight on quantum mechanical effects as well as the role of image charges. Measuring the tunneling conductance G_t as a function of the tunnel distance d yields the apparent barrier height $\phi_A \propto \partial(\ln G_t)/\partial d$, which is equal to the work-function for $d \longrightarrow \infty$. In a quantum-mechanical jellium model[8] and within the local density approximation the apparent barrier height is ex-

[8]The jellium model replaces the ion cores in the metal surface by a uniform positively charged background.

pected to decrease below the work-function at a distance of 0.6 nm, an effect that has been observed in STM experiments [111, 112]. However, in a more recent study under ultra-clean conditions a constant value of ϕ_A has been reported and it was argued that adhesive forces between tip and surface counterbalance the decrease in ϕ_A [113]. The obtained barrier heights in that study was 4.7 ± 1.0 eV, which is close to the expected value of an Au-vacuum interface. Similar results were reported for MCBJ under ultra-clean conditions [114]. It is important to note that for experiments conducted without ultra-high vacuum a drastic lowering of the potential barrier (down to 0.5 eV for a gold-vacuum-gold junction) is typically observed for STM junctions [115] as well as electromigrated gaps [116, 117]. In particular, for a gold-SiO_2vacuum-gold junction the reported values for the potential barrier vary from 0.7 eV in ambient condition [116] to 2.4 eV for a vacuum of 10^-6 mbar [117]. It should be noted that in these experiments the obtained barrier heights strongly vary from sample to sample. The question if (classical) image charge effects need to be considered for nano-scale electrodes seems to be still under discussion. It has been reported that best agreement to experimental current-voltage characteristics was obtained without image charge effects [116]. Modeling the distance-dependent tunneling conductance with a constant barrier height showed very good agreement to the experimental data and it was concluded that image charge effects are small for nano-scale electrodes [114]. However, in a later study by the same group the experimentally obtained transition voltage as function of distance could not be modeled without the inclusion of image charges [118]. In addition, other authors also claim good agreement when using a model with image charge [117].

2.3 Electro-Plasmonics

The goal of this chapter is to give an overview on the field of electro-plasmonics. Recently, this field has obtained much attention and researchers explore different aspects of the interplay between electrons and plasmons. The first part of this chapter tries to categorize the field of electro-plasmonics and give a general overview. The second part will focus on light emission from inelastically tunneling electrons.

2.3.1 Overview

Many applications are based on the interplay of optical-frequency photons and static electric fields or currents. In principle all these applications could show an increased performance by implementing optical antennas. Optical antennas can be designed for large absorption cross-sections, strong field confinement and enhanced near-fields. The design of the antenna strongly depends on the requirements of the application and antennas have been used as passive and active elements.

The field of electro-plasmonics is rapidly growing and many exciting experiments have been conducted. The goal of this chapter cannot be to give a complete summary but it is rather meant to give a glimpse on the variety of the different experiments. To this end an attempt is made to categorize these experiments, even though strict boundaries cannot always been drawn. The four categories of **Plasmon assisted**

charge extraction, **Excitation of plasmons with electrons, Plasmon assisted light emission**, **Modification of plasmons by DC fields** and **Nonlinear electroplasmonics** are addressed individually in the following.

- **Plasmon assisted charge extraction** This category features photodetectors and photovoltaics, photocatalysis as well as electron emission. All of these applications benefit from the increased absorption cross-section of antennas as well as their capability to concentrate light into small volumes. In the case of photodetectors, antennas hold promise to reduce the detector size leading to increased sensitivity due to reduced noise, lower power consumption as well as increased speed [119]. A tenfold photocurrent increase was observed by adding a "nanoantenna" consisting of a metal grating with a sub-wavelength aperture on top of a silicon photodiode [120]. Dipole nano antennas have been implemented into germanium IR-photodetectors and a polarization contrast factor of 20 has been demonstrated [34]. Polarization contrast was also observed by designing the electrical contacts to a Ge nanowire as an optical antenna and a broadband absorption enhancement of 1.7 was reported [36]. Moreover, antennas were used as polarization and wavelength-sensitive active elements for photocurrent generation by plasmon-induced hot-electron injection [35].

  For photovoltaic cells the main benefit of antennas is to increase the absorption either by scattering into an absorbing layer or by positioning the absorbing layer directly into the enhanced antenna near-field. Further information can be found in review papers covering conventional solar cells [37] as well as photovoltaic devices based on hot-electron generation [121]. Moreover, plasmonic enhancement by nanoantennas is used for the conversion of solar into chemical energy [38].

  Another exciting field is (photo)electron emission from metal nanostructures. In various experiments sharp metal tips are excited by short laser light pulses. The enhanced near-field at the very tip promotes electrons to the vacuum level by a multiphoton absorption. Thus the tip acts as a pulsed source of strongly localized electrons. The region from where electrons are emitted is in the nanometer regime [122] and the pulse duration is below 100 fs [123]. It is interesting to note that strong-field effects [18, 124] have been observed in these structures and attosecond control has been achieved [125]. It should be noted that photo-electron emission microscopy (PEEM) is also used as an imaging technique featuring ultra-fast temporal and nanometer spatial resolution. An overview of this technique can be found in [55]

- **Excitation of plasmons with electrons** Since electrons can be easily confined to the nanometer regime, the excitation of plasmons with electrons allows for a high resolution mapping of plasmonic near fields. In electron energy loss spectroscopy (EELS)[9] [9, 127, 128] an electron beam is raster scanned over the structure and from the amount of energy loss plasmon excitation is deduced. In cathodoluminescence [8, 129] a high-energetic electron beam is used to excite plasmon modes and its subsequent radiation is detected as an optical signal. An

[9] Remarkably, plasmons were observed for the first time using this technique [126].

extensive review on these two techniques is presented in [130]. Excitation of plasmons with electrons is not only interesting from a microscopy point of view but also to convert electronic to photonic signals. This aspect is discussed in the next category.

- **Plasmon assisted light emission** This category is based on the radiative recombination of electrons and holes in semiconductor light emitting devices (LED) [40, 131] as well as in organic LEDs [39, 132]. An overall electroluminescence enhancement of 3 was demonstrated by placing silver nanoparticles on top of Si-based light-emitting diode [133]. Using a patterned sub-wavelength hole array as a top electrode in an organic light-emitting device the electroluminescence was enhanced by a factor of 7 [134]. A further increase is expected by employing carefully designed nanoantennas. Moreover, nanoantennas could be designed with distinct radiation properties, allowing for control of the polarization as well as spectral and angular distribution of the emitted light. A pioneering experiment has demonstrated a control over the fluorescence spectrum of a quantum dot by means of the Stark effect [135].

  Stimulated emission was achieved and electrically pumped nanolasers have been realized [41, 42]. This concept can also be used to provide gain for propagating plasmons [136]. Recently, an electrically driven optical nanocircuit has been realized by coupling electroluminescence into a plasmonic waveguide [137].

  Besides electron-hole recombination, far field photons have been excited by inelastically tunneling electrons. A variety of experiments exploit plasmonic modes to enhance this electron-photon conversion process in scanning tunneling microscopes (STM) as well as layered systems. A detailed overview of this field is given in the next section 2.3.2.

- **Modification of plasmons by dc-fields** The prospect of modifying plasmonic properties by electric field is mainly studied to realize an electro-optical switch or modulator. An electric field can change the refractive index of a dielectric and therefore shift the resonance wavelength of the plasmon. First prototype devices have been demonstrated using liquid crystals [138–140] as well as phase change media [141]. Electro-optic effects such as the Pockels effect, which produces a birefringence upon an applied electric field, could possibly be employed as well.

- **Nonlinear electro-plasmonics** The last category is based on nonlinear optics and relies on the mixing of zero-frequency and optical-frequency field components. This field is still in its infancy but is expected to gain significant attention in the near future. Pioneering experiments have demonstrated electrically controlled second harmonic generation [142] and optical rectification [143].

2.3.2 Photon emission from inelastically tunneling electrons

A particular interesting aspect of electro-plasmonics is the generation of plasmons by inelastically tunneling electrons in metal-insulator-metal (MIM) junctions. The basic concept of the inelastic tunnel process is sketched in Figure 2.11. Applying a voltage V_{app} to the right metal electrodes raises its Fermi level with respect to the left electrode. The electric potential between the electrodes and the nanometer distance between the electrodes gives rise to a finite probability for electrons to tunnel from the right to the left electrode. The MIM junction can provide plasmonic modes, whose local density of states depends on the geometry of the junction. Electrons can tunnel into/via these states resulting in the excitation of a plasmon, which can subsequently decay radiatively and lead to the generation of a photon. Since the electron loses energy during this process, it is called inelastic tunneling.

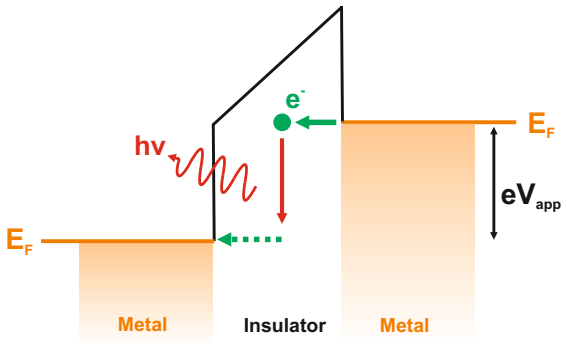

Figure 2.11: Sketch of the inelastic tunneling process. Electrons tunneling from the right to the left electrode, couple to the plasmonic gap mode and are converted into free-space photons.

The goal of this chapter is to give an overview on the research field of photon emission from tunnel junctions. A simple model for the excitation process is provided and typical junction geometries are discussed.

The first light emission by inelastically tunneling electrons IET was observed in 1976 by Lambe and McCarthy [144]. Metal-Insulator-Metal tunneling junctions were fabricated by oxidizing an aluminum film and consecutive evaporation of a counter electrode. The authors claim to obtain gaps of 3 nm and report that roughing of the electrode by a mild etch leads to an increased out-coupling of light. Broad-band light emission was observed with a high-frequency cutoff $h\nu = |eV_{app}|$ depending on the applied voltage V_{app}. The authors attribute their results to the excitation of surface plasmon modes which are out-coupled via surface roughness. The effect of surface roughness was investigated in more detail by the same group [145]. They compared bare Al-Al_2O_3-ITO tunnel junctions to junctions where silver particles were added on top as well as embedded into the ITO layer. The junctions with embedded silver particles showed an increase in light emission by one order of magnitude with respect to the bare junction. The external quantum efficiency of their best devices was 10^{-5}. Similar values were reported by Hansma and Broida [146]. In their experiments the

top electrode consisted of Au particle clusters overlaid with a conducting Au film. The authors present light emission spectra as a function of voltage. These results are reprinted in Figure 2.12a. The shape of the spectrum is not discussed in detail by the authors. It seems there are two contributions, a shoulder in the NIR spectral region as well as a peak at 1.9 eV which is becoming more pronounced for higher voltages.

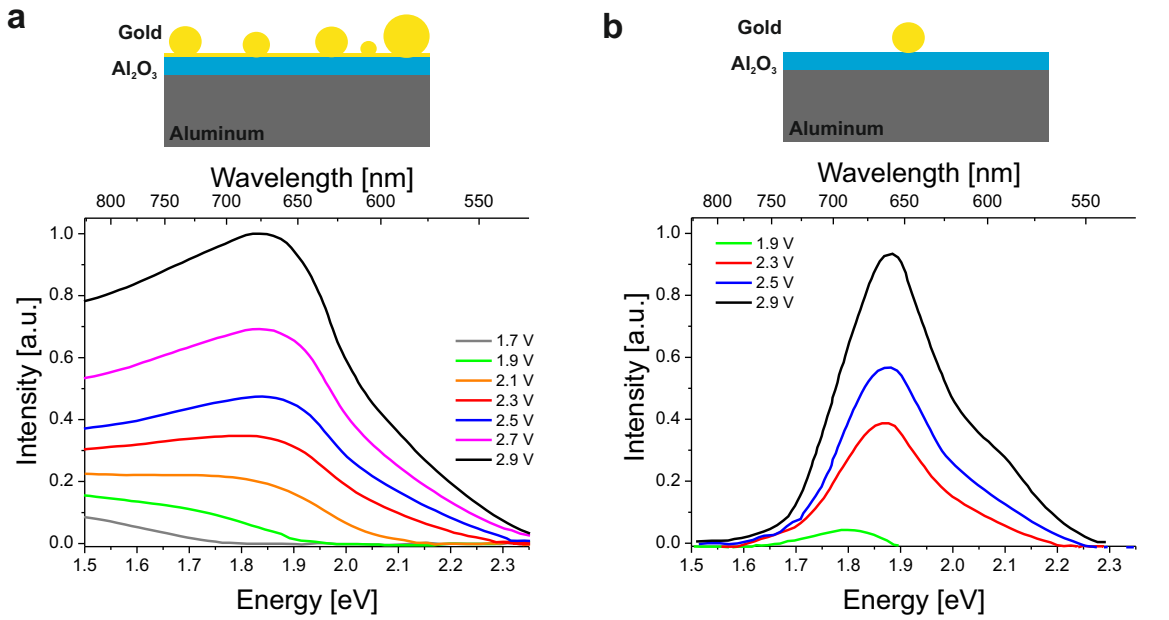

Figure 2.12: Light emission from metal-insulator-metal tunnel junctions. **a** Experimentally investigated tunnel junction geometry and light emission spectra for different applied voltages. Data from [146]. **b** Modeled geometry and theoretical calculation of light emission spectra for different applied voltage. Data from [147].

The theoretical modelling of the MIM tunneling junctions was presented soon after the experiments. Rendell and Scalapino [147–149] model a single sphere on top of an insulator-covered metal film, exhibiting a localized plasmon resonance. Their calculation show a well-defined light emission spectra with a maximum at 1.9 eV, once the applied voltage is larger than 1.9 eV (Figure 2.12b). The idea of their model is based on a two-step process: in the first step a fluctuation of the tunneling current excites the plasmon mode of the antenna and then in the second step the antenna radiates photons. It is argued that the fluctuations originate from shot noise and that only the frequency-dependence of the fluctuating current is important for the light emission. Recently, experimental support of this hypothesis was given in a study on single-atom contacts [150]. The current power spectrum $C(\omega)$ is given by the rate of tunneling electrons. It can be calculated by Fermi's golden rule, which describes the transition from initial to final state. For the interaction (or perturbation) term in the matrix element the tunneling (or transfer) Hamiltonian [151] is used. Under the assumption of zero temperature and within a free-electron model the resulting current power spectrum reads as

$$C(\omega) = \frac{eV}{2\pi R_0}\left(1 - \frac{\hbar\omega}{eV}\right). \tag{2.23}$$

Here V is the applied voltage and R_0 denotes the DC junction resistance. The result reflects the fact that electrons loosing small energies have more final states available than electrons loosing large energies. It is important to note that so far this equation does not contain any contribution of the plasmon itself. The fluctuating current serves as a source exciting the plasmon, which subsequently radiates. The radiated power can be described by the multiplication of the current power spectrum $C(\omega)$ by a factor $A(\omega)$ which takes the excitation and radiation efficiency of the plasmon mode into account. The system consequently acts as an antenna and converts an oscillating current into a free-space photon. Within a linear process the applied voltage determines the maximum energy of the photon and leads to a quantum cutoff. For voltages much larger than this cutoff the spectrum of the radiated light is largely dominated by the plasmon resonance.

Even though the model based on the fluctuating tunnel current is now widely accepted, it is worth noting that there was quite some controversy in the early days. In particular, the observed s-polarized emission along the surface normal [152] could not be explained. Therefore a complementary study by Laks and Mills [153] uses an approach based on perturbation theory to calculate the amount of scattering of a surface plasmon at a surface roughness, instead of considering a localized plasmon. Within this model an s-polarized component is predicted, however the fact that the excess p-polarization shows a maximum for an angle of 55° is not observed. Moreover, Kirtley et al. [154] studied light emission from tunnel junctions on gratings. Even though the intensity of the emitted light did scale as predicted by equation 2.23 the overall intensity did not agree to the theory [153]. This led the authors to the proposal that injected electrons could play an important role [155]. This controversy was addressed later in a theoretical study by Persson and Baratoff [156], who have calculated the overall efficiency of photon emission from electron tunneling to be 10^{-3} and of hot-electron injection to 10^{-6}. In the overall efficiency a plasmon radiation efficiency of 10^{-1} has been included. It should be noted that also here a tunneling Hamiltonian formalism is used and the tunneling current is calculated via Fermi's golden rule.

The main activity of tunnel junctions based on layered structures more or less ended in the 1980s. In a review paper by Szentirmay [157] this is attributed to the much smaller quantum efficiency of the MIM devices compared to semiconductor devices. As mentioned above, discrepancies between experiment and theory existed in this early work. The experimentally observed infrared component of the light emission is not predicted from theory (Figure 2.12) and the polarization dependency could not be explained [152]. Possibly this can be attributed to the fact that at that time microstructures with well-defined and pronounced plasmon resonances could not be fabricated.

A tool allowing for precisely controlled experiments, the scanning tunneling microscope STM, was invented in the 1980s [158]. Just a few years later the first photon emission experiments were conducted by tunneling from a tantalum/silver tip into a silicon/silver substrate [159, 160]. Already at this very early stage it could be shown that the emitted light shows variations on the sub-nanometer scale, due to its sensitiv-

ity to the distance between tip and sample[159]. The spectral features were attributed to plasmon resonances [160].

The fact that light emission arises from the coupling of inelastic tunneling electrons to the plasmonic cavity modes formed by the tip and sample was experimentally demonstrated by Berndt et al. [161] and supported by the theoretical model of Johansson, Monreal and Apell [162]. Berndt et al. [161] showed a transition from field emission to tunneling regime by changing the tip voltage in constant current mode, which leads to a tip retraction at larger voltages. Significantly more photons were observed for small tip voltages in the tunneling regime. Spectra have been measured in the tunneling and field emission regime. A good agreement between calculation and emission spectra in the tunneling was observed, as shown in Figure 2.13a. Three different metal substrates (Ag, Au, Cu) were investigated and their different emission spectra were related to the dielectric functions. However, for all materials a red-shift of the tunneling spectra with respect to the field emission spectra has been observed. The authors did not explain this red-shift, but it is possibly related to the increase of gap size with increasing voltage. Another important aspect of their work was to demonstrate that the dominant excitation process occurs by inelastic tunneling rather than hot electrons. The authors based their argumentation on the fact that the light emission was not polarity dependent and on their study of isochromatic spectra as a function of conductivity.

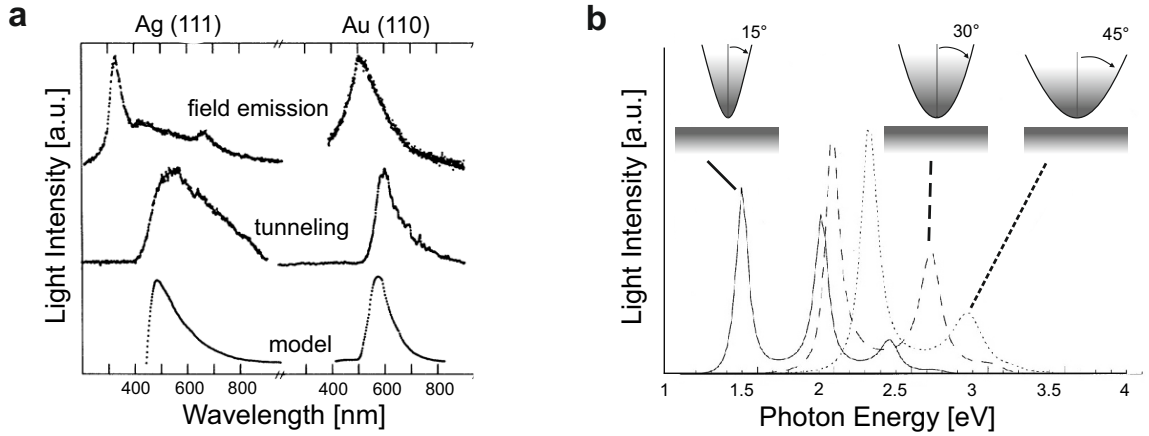

Figure 2.13: Light emission from tip-sample tunnel junction in a STM. **a** Light emission for a silver and a gold tip. Top row: field emission regime, center row: tunneling regime, bottom row: calculation. Modified from [161]. **b** Light emission spectra for different Ag tip apertures at a distance of 0.5 nm from an Ag substrate. Modified from [163].

The theoretical model by Johansson, Monreal and Apell [162] is in essence very similar to that of Rendell and Scalapino [148] and the tip-induced plasmon is excited by a fluctuating current. Instead of calculating the radiated field by the dipole in the gap directly, the authors employ the reciprocity theorem and calculate the optical field in the tip-film cavity induced by a point current density far away. Neverthe-

less, the basic objective is still to determine the frequency-dependent current as well as the optical properties of the junction. In their formalism the optical properties are described by the Green's Function and the current-density is determined by the tunneling Hamiltonian [151].

The optical properties of the cavity formed between STM tip and film are governed by the geometrical dimensions as well as their material. Most intense luminescence is typically found for noble metal junctions, for example the light emitted from an Au-Au junction is one order of magnitude larger than for a W-Au junction due to the larger damping of tungsten [164]. Moreover, a theoretical study [165] found that a dielectric layer (C_{60}, Al_2O_3) leads to a considerable decrease in light emission due to the increased tip-metal separation. Similar reduction is experimentally observed if a water film is present between tip and sample [166]. Johansson [167] modeled the STM tip as a sphere and found that a smaller tip-sample distance leads to a higher light intensity as well as a red-shift of the emission spectra. In the case of an Ag-Ag junction it was found that the fundamental mode strongly shifts to smaller energies with an increase of the tip radius. A more realistic hyperbolic tip shape was considered by Aizpurua et al. [163]. In this work it was shown that the tip aperture has a drastic influence on the emission spectra and that an increase of the aperture angle leads to emission at larger energies (see Figure 2.13b). The tip curvature, i.e. sharpness of the tip, mainly effects the radiated power, which is larger for sharp tips. Strong effects of the tip shape on the emission spectra were also observed in an experimental study [168]. The authors further report a truncation of the tip during the tip approach as well as the observation of microstructure at the tip apex after scanning. In this context, it is worth mentioning that under ambient conditions at room temperature a modification of the surface (and tip) upon scanning is observed at least for elevated bias voltages [169, 170].

Light emission from STM tunneling junctions could be employed in a variety of exciting experiments. Standing wave patterns of two-dimensionally confined electrons were imaged [171]. The localized electronic states of atomic silver chains could be probed [172]. The transition probability from initial to final states, i.e. Fermi's golden rule, was visualized [173]. In addition, the mapping of electric-field distributions of individual [174] and coupled plasmon modes [175] was claimed. In the case of a single-atom contact the optical spectra revealed single- and multi-electron processes, which were consistent with a hot electron cascade process [171, 176]. Furthermore, propagating plasmons could be excited on flat gold films [177] as well as nanowires [178].

Besides pristine junctions the light emitting properties of organic molecules, C_{60} nanocrystals as well as semiconductor quantum well and dots have been studied. For semiconductor materials light emission is reported to arise from electron injection into the electronic bands and a subsequent interband transition [179, 180]. In the case of organic materials the light generation process drastically depends on the coupling to the metal electrodes. If the material is directly placed on the metal, non-radiative quenching prevents the observation of intrinsic luminescence and the dominant light emission process is inelastic electron tunneling. In this case three different effects of the molecules have been identified: the molecules act as a dielectric spacer altering the field strength of the junction mode [164, 165, 181, 182], the molecules change the density of

initial or final states and thereby effect the efficiency of the inelastic tunneling [183, 184] or the molecules act as dynamic dipole oscillator enhancing the plasmon modes [182]. However, by placing an additional insulating material between molecule and metal [185] or by using molecular multilayers [186] intrinsic luminescence of the molecules can be observed and spatially mapped [187]. The proposed mechanism is an injection of electrons into molecular electronic states, relaxation to a lower vibrational level and subsequent radiative transition mediated by the junction plasmon. The plasmonic enhancement of the tip-sample nanocavity was further employed for up-conversion electroluminescence [188] and Raman spectroscopy with sub-molecular resolution [12].

As demonstrated above, the plasmonic enhancement of the tip-sample cavity has been and is widely used and its strong dependence on the junction geometry is well known. Nevertheless, so far, little effort has been made on optimizing the radiative properties of the junction. Typically observed quantum efficiencies, i.e. number of photons per electron, of the inelastic tunneling process are on the order of 10^{-5} in air [189, 190] and 10^{-4} in ultra-high vacuum [191]. For the case of electroluminescence of organic materials reported quantum efficiencies are on the order of 10^{-5} [186, 192]. It has been reported that the radiation from the junction itself is very poor and more than 90% of the excitation decays into propagating plasmons [177]. Consequently, there is an enormous potential for optimizing the radiative properties of the plasmonic junction. In Chapter 6 a first step in this direction is taken. It is demonstrated that by exploiting a plasmonic nanoantenna the quantum efficiency of the light emission can be as high as 10^{-4} and the electroluminescence spectrum as well as polarization and directivity can be controlled by the antenna.

3 Basic experimental concepts

3.1 Sample preparation

In this chapter the techniques that have been developed or used during this thesis are presented. For several techniques co-workers contributed significantly or even developed the technique. Nevertheless, the main steps of all sample preparation techniques are listed in detail so that the results of this thesis can be reproduced.

3.1.1 Substrates and marker structures

All experiments in this thesis investigate gold nanostructures. Depending on the specific experiment, there are various requirements on the substrate. Optical measurements are performed with an inverted microscope and consequently the substrate needs to be transparent in the visible wavelength range. To avoid complications in fabrication and for a low background in the optical experiments a low surface roughness is required.

These primary requirements are fulfilled by borosilicate cover slips (Menzel Gläser, Braunschweig, DE), which have been used for all samples presented in this thesis. The cover slips have a thickness of 0.17 ± 0.01 mm and are 24×24 mm^2 in size. Prior to further fabrication steps the substrates are thoroughly cleaned by a multi-step procedure. Several cleaning procedures have been tested and by using the following protocol clean glasses are obtained in a reproducible way. The first step consists of mechanical wiping with an ethanol-soaked lens tissue. Next the glasses are ultrasonicated in spectroscopy grade (p.A.) acetone and subsequently spectroscopy grade (p.A.) ethanol for 10 min each. Ethanol is slightly volatile, which can lead to streaks upon drying. To avoid drying of ethanol, the glasses are rinsed in ultrapure water (Milli-Q, Millipore Corp., Billerica, USA)[1] and afterwards blow-dried with nitrogen gas. Remaining organic contamination is removed by exposing the substrate to an oxygen plasma (PDC-3XG, Harrick Scientific Products Inc., Pleasantville, USA) for roughly one minute. The cleanliness has been checked by a confocal fluorescence microscope with single-molecule sensitivity as well as with an Atomic-Force Microscope (Dimension 3100, Veeco, Plainview, USA) and no contamination was found. The substrates are very flat and an RMS roughness value of 0.28 nm has been measured with an AFM. A typical AFM image of a cleaned glass is shown in Figure 3.1. The small circular holes are an intrinsic property of the glass and have a diameter of 30 nm and a depth of 2 nm.

The nanostructures are typically imaged in a Scanning-Electron-Microscope SEM (Helios 600, FEI, Hillsboro, USA or Ultra Plus, Zeiss, Oberkochen, Germany). The imaging electrons can charge an insulating substrate and for a good image quality

[1] The Milli-Q water was kindly provided by the Technical Physics, University of Würzburg, DE.

excess charges need to be removed. It should be noted that the Zeiss SEM allows for acceleration voltage down to 500 eV and oxygen gas can be injected for charge compensation. Non-conductive substrates can therefore be imaged in this SEM. Nevertheless, high resolution images of highest quality require a conductive substrate. For the purely optical studies presented in Chapter 4 the glass substrates have been covered with a 200 nm thick indium-tin-oxide (ITO) layer to provide the necessary conductivity. The ITO layer was kindly provided by the ZAE Bayern and was processed via a sol-gel routine using a dip-coating technique [193]. The layers are quite smooth but exhibit grainy features as can be seen in the AFM image 3.1b. The measured RMS value is 0.84 nm. Despite the grainy surface the ITO layers showed negligible background in the white-light scattering setup.

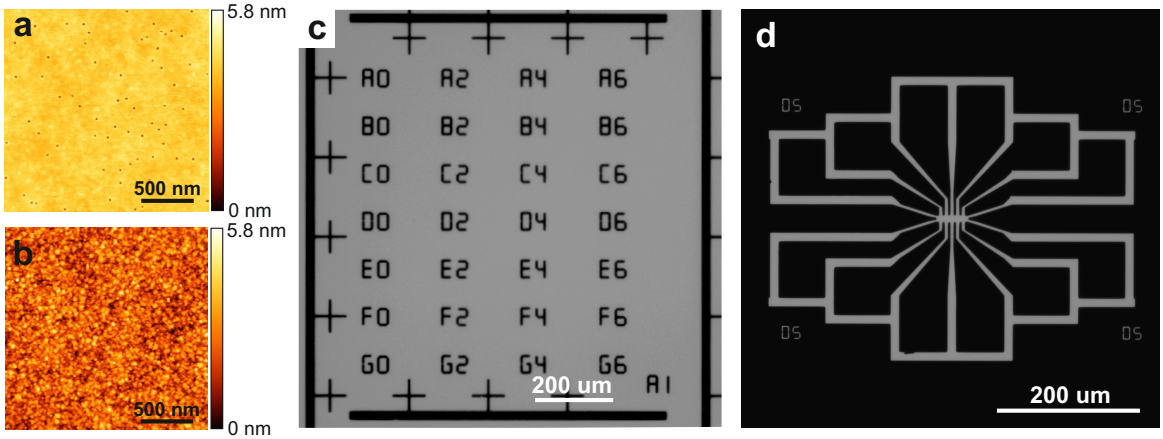

Figure 3.1: Substrates and marker structures. **a** AFM of a cleaned borosilicate cover slip. **b** AFM image of an ITO-coated borosilicate cover slip. **c** Optical white-light transmission image of a marker structure designed for optical experiments. **d** Optical white-light transmission image of an electrode structure designed for electro-optical experiments.

The use of a marker structure has proven to be convenient to identify the nanostructures in the optical microscope as well as in the SEM. The marker structure has been designed in collaboration with Monika Emmerling from the Technical Physics, University of Würzburg, DE. All lithography process steps were conducted by Monika Emmerling. The optical mask was fabricated from a Chromium covered glass plate (G-Materials, Deggendorf, DE) using electron-beam lithography (EB100, Eiko Corp., Japan). The 100 nm thick PMMA resist is prepared by spin-coating and baked at 165° for 120 s. The resist is exposed to a beam current of 20 nA at an acceleration voltage of 80 kV and a dose of 1000 μC/cm^2. Unexposed areas are removed after 25 s in a solution of a 1/3 mixture of 4-Methyl-2-pentanone/Isopropanol and subsequently rinsed in Isopropanol for 25 s. After a wet-chemical etching of the chromium the exposed areas are transparent in the blue spectral region and the mask can be used for optical lithography. There the first step is spin-coating a 1 μm thick layer of positive photoresist (ma-P 1215, micro resist technology GmbH, Berlin, Germany) onto the substrate.

Next the optical mask is brought in contact with the substrate (Maskaligner MJB3, SÜSS MicroTec, Garching, Germany) and the photoresist is exposed to ultraviolet light (λ=405 nm) for 7 s. As a next step the resist is chemically developed (20 s in ma-D331, micro resist technology GmbH, Berlin, Germany) and afterwards rinsed in ultrapure water. A 5 nm thick Chromium adhesion and subsequently a 50 nm layer of gold are thermally evaporated at a rate of 1 Å/s at a vacuum pressure of 10^{-6} mbar. In a final lift-off step (60 s in 80° C 1-Methyl-2-pyrrolidinone (J.T. Baker) the unexposed photoresist is removed. An optical white-light transmission image (IX 70, Olympus, Tokyo, Japan) of the unit cell of the marker structure is shown in Figure 3.1c.

For the electro-optical experiments the substrate must be intrinsically non-conductive. In order to still be able to perform SEM, an electrode/marker structure and a suitable sample holder have been designed. A unit cell of this electrode structure is shown in an optical white-light transmission image in Figure 3.1d. Each unit cell consists of 12 electrode bars, which are electrically isolated from the otherwise continuous gold film covering the substrate. In addition each unit cell provides 2 electrodes which are connected to the continuous film but are not connected to the other electrodes. The gold film is electrically connected to ground potential via the sample holder and excess charges can be removed. The electrode structure uses a negative mask, which was fabricated by the same procedure as listed above. For the optical lithography a thin adhesion layer (AR 300-80, ALLRESIST GmbH, Strausberg, DE) is necessary, which is spin-coated and afterward baked at 95° C for 60 s. Next a 1.3 μm thick negative resist (AR-U4030, ALLRESIST GmbH, Strausberg, DE) was spin-coated and afterward hardened at 95°. The undeveloped resist is removed in a wet chemical process (30 s in AR-300-35, ALLRESIST GmbH, Strausberg, DE) and the sample is subsequently rinsed with water. Finally a 20 nm chromium adhesion layer and subsequently a 100 nm layer of gold are thermally evaporated at a rate of 1 Å/s.

3.1.2 Gold nanorods and spheres

Gold nanoparticles are widely used in the literature and many different synthesis routine are employed, see e.g. [194, 195] for a review on nanorods and [196] for a review on nanospheres. The gold nanorods (TM 30-25-650) and spheres (A11C-30-CTAB-1) used in this thesis have been purchased from Nanopartz (Nanopartz, Loveland, USA). The nanorods exhibit an intrinsic size distribution with lengths and diameters of about 70±10 nm and 30±10 nm, respectively. The nanospheres are very mono-disperse and have a diameter of 30±2 nm. Cetyl-Trimethyl-Ammoniumbromid (CTAB, C19H42BrN) is used as a capping agent. In the literature [197, 198] it is reported that a bilayer forms on the surface of the gold nanorod as illustrated in Figure 3.2a.

The crystal structure of the rod is typically[2] reported to consist of {110}, {111} and {100} facets [200, 201] and is schematically depicted in Figure 3.2b. The high-angle annular dark field scanning transmission electron micrograph (HAADF-STEM) image was taken by Nadezda Tarakina and Martin Kamp at the Technical Physics,

[2]In a recent publication [199] this assignment is questioned.

University of Würzburg, DE using an FEI Titan 80-300 electron microscope operating at 300 kV.

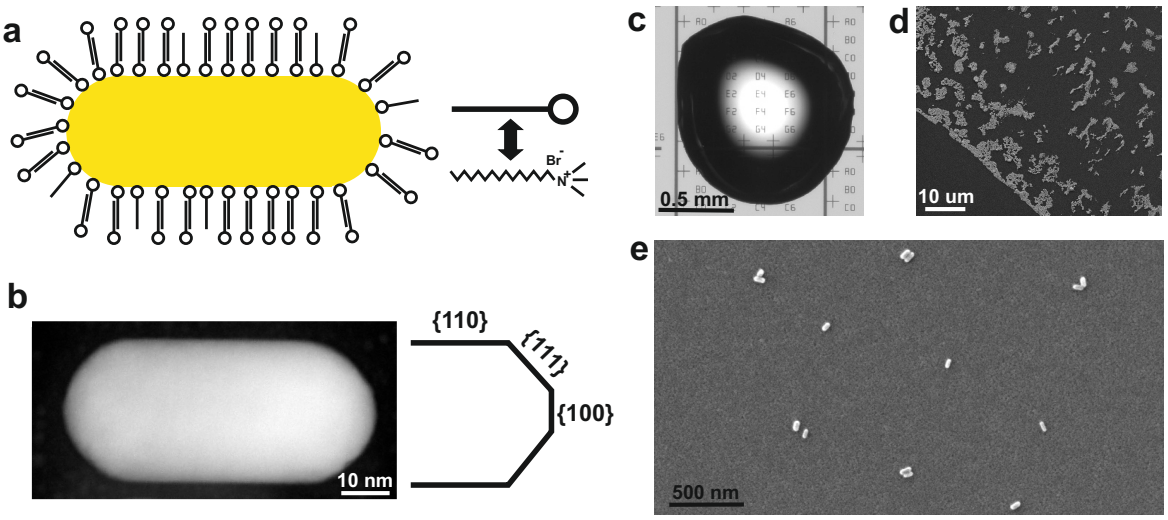

Figure 3.2: Gold nanorods. **a** Schematic illustration of a gold nanorod and its surfactant bilayer. **b** HAADF-STEM image of a gold nanorod and illustration of the crystal facets at the end cap. **c** Drop-casted nanorod solution. **d** Electron micrograph of the rim of a droplet with high concentration. **e** Electron micrograph of the rim of a droplet with low concentration.

The procedure to obtain nanorod dimers, which are investigated in Chapter 4, is as follows: In order to break up agglomerates the original solution is ultra-sonicated for 3 min. It has been found that the highest yield of dimers is obtained by diluting the original solution with a concentration of 10^{10} particles/mL by 1:15 with ultrapure Milli-Q water. Typically 1 μL of the solution is soaked up with a pipette and is dispensed onto the ITO-coated glass coverslip. A transmission image of a droplet can be seen in Figure 3.2c. It should be noted that small spherical droplets gave the best result in the self-assembly. Because of the coffee stain effect [202], the nanorods gather at the rim of the droplet as can be seen in the SEM image of an undiluted solution (Figure 3.2d). An SEM image of a diluted solution is shown in Figure 3.2d and single rods as well as rod dimers are observed at the rim of the droplet (Figure 3.2e). Gold nanorods tend to align side-by-side due to the joint action of capillary forces [203] and the interdigitation of the nanorods surfactant layers in order to minimize the hydrophilic-hydrophobic interaction in presence of water [204, 205]. After the self-assembly, excess CTAB is removed by rinsing the sample in 70° C warm ultrapure Milli-Q water and exposing it to an oxygen plasma.

The gold nanospheres used in Chapter 6 are drop-casted in a similar way as the rods. However, the stock solution of the gold spheres has a concentration of 10^{13} particles/mL and is diluted 1:100. In addition the droplet volume has been increased to 4 μL, such that the droplet is slightly larger than the unit cell of the electrode structure.

3.1.3 Single-crystalline gold flakes

In this thesis electrically connected nanoantennas are used for electro-plasmonic experiments. The reproducible fabrication of well-defined antenna gaps is a key requirement for the fabrication of the tunnel junctions studied in Chapter 6. During the course of this thesis a process based on a combination of bottom-up and top-down methods has been developed and allows for the precise fabrication of complex nanostructures from single-crystalline gold [73]. This section discusses the bottom-up chemical synthesis of single-crystalline gold flakes. The flakes are later on deposited on a substrate and the desired shape is milled with a focused ion beam (FIB), which will be presented in the next chapter. The synthesis leads to flakes of different sizes and triangular as well as hexagonal shape. A typical example is shown in Figure 3.3a. The gold flakes exhibit smooth surfaces as can be seen from an electron micrograph of a flake edge in Figure 3.3b. In contrast evaporated multi-crystalline gold films exhibit grains and a SEM image of the interface between a 10 nm (bottom) and a 30 nm (top) thick gold film is shown in Figure 3.3d. For a quantitative comparison a cross-section of the surface has been measured by AFM and is presented in Figure 3.3c. The lateral dimensions of the crystal grains in the 30 nm thick evaporated film are measured to 30-50 nm and have a height of 2-6 nm. The surface of the single-crystalline flake has a roughness of less than 1 nm and no grains are visible. A transmission electron micrograph, demonstrating the single-crystalline nature of the flakes, is shown in the next chapter (Figure 3.4).

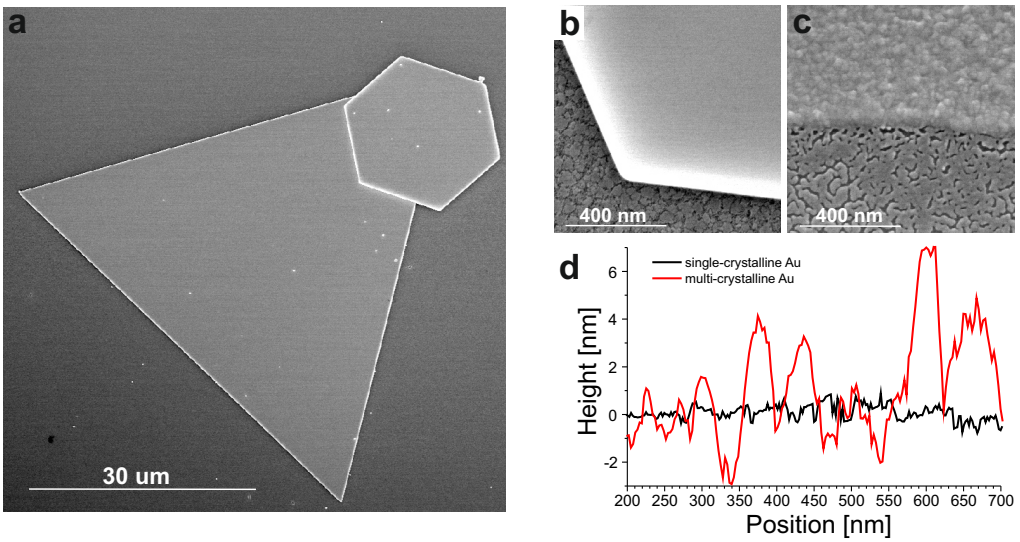

Figure 3.3: Single-crystalline gold flakes and multi-crystalline gold films. **a** Electron micrograph of two single-crystalline gold flakes. **b** High magnification electron micrograph of a single-crystalline gold flake deposited onto ITO. **c** High magnification SEM image of an evaporated multi-crystalline gold film. **d** Height profile of single-crystalline gold flake and evaporated multi-crystalline gold film obtained from AFM measurement.

The chemical synthesis is based on the recipe of [206]. The search for the recipe which reproducibly gives the largest flakes has not finished so far. It is difficult to

obtain detailed knowledge of the growth mechanism on a microscopic level and there is no consistent model in the literature. For more information the following references provide a good overview [207–209]. Nevertheless two protocols are listed in the following: A very reliable protocol uses aniline and glass containers. Gold flakes with lateral sizes of up to 70x70 μm^2 and thickness of 30-100 nm are obtained with this recipe. The recipe is as follows: After thorough cleaning of the glass containers, 180 μL of 0.1 mol/L aqueous solution of chloroauric acid $HAuCl_4$ (Sigma Aldrich) is prepared and added to 20 mL of ethylene glycol (Sigma Aldrich and J.T. Baker gave similar results). The solution is continuously stirred in a 50° C water bath for 20 minutes. Afterward a 0.1 mol/L solution of aniline in ethylene glycol is added drop by drop to the solution under intense stirring. After stirring for another 5 minutes the reaction vessel is placed into an oven heated to 50° C. The reaction is terminated after 48-72 h. At that time the solution has turned from yellowish to brownish red.

The protocol currently leading to the largest flakes with sizes up to 150×150 μm^2 does not use aniline and instead the reaction is conducted in polypropylene (PP) centrifuge tubes (Greiner Bio-One, Frickenhausen, DE) at 95° C for 24 h. In this recipe 72 μL of gold salt with a concentration of 0.5 mol/L is added to 40 mL of ethylene glycol. The role of the PP tubes is not known in detail at the moment. However, the presence of bis(p-methylbenylidene)sorbitol as well as 4-Methyl benzaldehyde could be detected in an NMR analysis[3] of ethylene glycol which was situated in a PP tube at 95° C for 24 h. It is interesting to note that at high temperatures of 140° C ethylene glycol can oxidize to glycol aldehyde which was identified as the primary reductant in polyol synthesis [210]. In addition, it should be pointed out that the pH value of the solution has an important influence [211].

It is possible to directly grow the flakes on the substrate by adding the substrate to the growth solution. The advantage is a stronger adhesion of the flake to the substrate as well as fewer gold particles on top of the flake. However, it was found that a significant amount of large flakes grows only on substrates with a low electrical conductivity such as glass cover slips, mica, PMMA, silicon with an oxide layer and PVA. On substrates with a large electrical conductivity such as ITO, doped TiO_2 and p-doped silicon without an oxide layer, only few and very small flakes could be grown at best. It should be mentioned that these studies were mainly conducted by Xiaofei Wu.

3.1.4 Focused Ion Beam milling

The nanostructures presented in Chapter 5 and 6 were fabricated by focused ion beam (FIB) milling of single-crystalline gold flakes. The advantage of this technique is that it allows (within certain limits) for the fabrication of arbitrary geometries and the results can be imaged directly after the milling. The nanostructures obtained by this technique are of highest quality [73]. For an overview on other fabrication techniques and typical results the reader is referred to [212].

The working principle of FIB is illustrated in Figure 3.4a. A high energetic ion beam

[3]The experiments were performed in the group of Dr. Andrés Guerrero Martínez at the University of Complutense de Madrid, SP

hits the target under normal incidence and can transfer its momentum and energy to atoms in the target. Depending on the collision the ions can backscatter or penetrate into the target. If the energy transfer upon collision is larger than the surface binding energy, the target atoms are sputtered into vacuum and are partly redeposited nearby. In addition secondary electrons can be generated. The ions entering the substrate can undergo multiple collisions and are finally implanted in the substrate. The penetration depth strongly depends on the material to be milled and the acceleration voltage of the ions. For gold and an acceleration voltage of 30 kV a typical penetration depth is 5 nm and the spatial extension of the implanted ions is about 5x5x5 nm^3. The values were obtained from reference [213] in which the interaction of ion and sample is described in more detail.

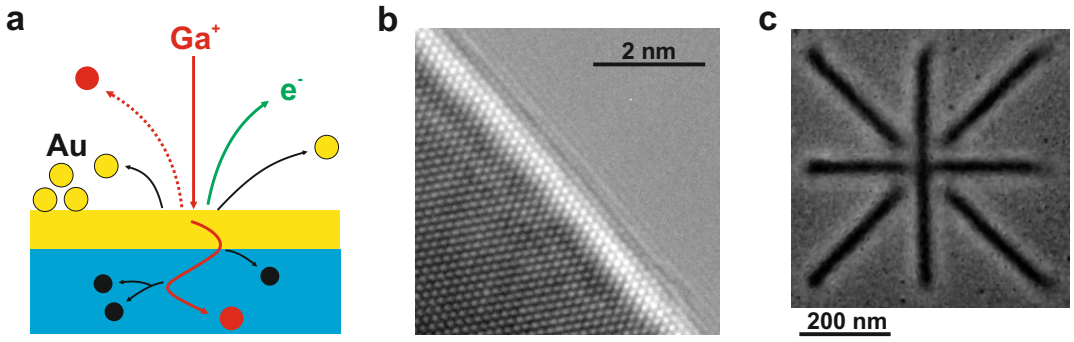

Figure 3.4: Focused-Ion-Beam FIB milling. **a** Working principle of FIB and illustration of beam-sample interactions. **b** Transmission electron micrograph of the edge of a milled single-crystalline gold flake **c** Electron micrograph of the alignment pattern after the ion beam was focused and corrected for astigmatism.

In this thesis a Dual-Beam SEM/FIB system (Helios Nanolab, FEI Company, Oregon, USA) has been used. For all experiments the ion acceleration voltage has been set to the maximum of 30 kV, at which the imaging resolution is specified to 5 nm by the manufacturer. By using single-crystalline gold flakes it was possible to study the effect of ion impact on the surface quality and the crystal structure was found to be preserved. A transmission electron micrograph of a patterned flake edge is shown in Figure 3.4b and does not exhibit any defects. However, it should be noted that sometimes small particles were observed at the edge and the sample was cleaned in an oxygen plasma to remove organic contamination from the edge. Milling of single-crystalline gold flakes is very reproducible, since it does not suffer from structural arbitrariness due to grains. Consequently the focus and astigmatism conditions can be precisely judged and aligned. To this end an alignment pattern consisting of a star-like arrangement of single lines has been designed by a co-worker, see Figure 3.4c. In the alignment procedure the focus or astigmatism is varied and the optimal condition can be chosen by the user. This semi-automatic alignment has proven to drastically expedite the alignment process. Ideal conditions are typically obtained within 30 minutes and cuts with linewidths of 20 nm can be easily achieved. The alignment pattern

has been written in the AutoScript xT language (FEI Company), which allows for a full control of all relevant parameters.

The milling strategy for nanostructures highly depends on the exact geometry of the nanostructure and the requirements of the specific experiment. In general, the following aspects should be considered:

- The smallest ion beam diameter is achieved for the highest acceleration voltage of 30 kV. In addition the beam diameter scales with the beam current and for highest resolution it should, in principle, be set as low as possible, i.e. 1.5 pA.

- The major issue for complex and/or large geometries is (even smallest) sample drift due to charging effects. Therefore the structure should be connected to ground potential as long as possible. The milling depth should be set just slightly below the actual thickness of the gold flake. Deeper milling leads to severe charging and distortion of the structure. For larger patterns the milling time starts playing a role and it was found that for structures larger than 2×2 μ^2 the second largest current setting, i.e. 9.7 pA, is a good trade-off between milling time and beam diameter. For very complex patterns it is best to use two milling steps. First a small and therefore fast milled pattern directly surrounding the structure and afterwards a large pattern removing the surrounding gold. Moreover, a temperature change in the laboratory leads to severe drift of the ion beam and the FIB system must be placed in a climate controlled room.

- Influence of redeposited atoms can be minimized by milling towards the antenna as well as by parallel milling rather than serial milling. As an example see Figure 3.5a,d.

In this thesis two-wire gap antennas with connectors for electrical measurements are used in Chapter 5 and 6. In the following the milling strategy used in this thesis is presented and the milling results of a 60 nm thick flake are discussed. The pattern consists of three levels, which are shown in Figure 3.5. The first layer (blue) consists of 10 rectangles and defines the geometry of the antenna. The rectangles are milled in parallel with a depth of 70 nm. The purpose of this first layer is to mill the antenna geometry as fast as possible in order to avoid drifts due to charging. In the second layer (red) a larger area around the antenna is removed by parallel milling of 6 rectangles each with a depth of 70 nm. The last step is the creation of the gap by cutting a line with a depth of 70 nm. For the fabrication it is crucial to keep the antenna at ground potential so that charges can be removed. The isolation of one antenna arm from ground, which is necessary for the electrical experiments, should be done as the very last step.

The final results are studied by SEM (Figure 3.5b) as well as AFM (Figure 3.5c). It should be noted that also for electron microscopy a removal of charges is required to avoid image artifacts. For this reason both antenna arms have been left connected to ground potential. The strength of AFM lies in its exact information for topology in the out-of-plane direction, i.e. the height of structures. The topography in the sample plane is a convolution of sample topography and the imaging tip. Consequently it is not possible to obtain precise information about the shape if the structure has steep edges and especially the gap of the antenna cannot be measured by AFM.

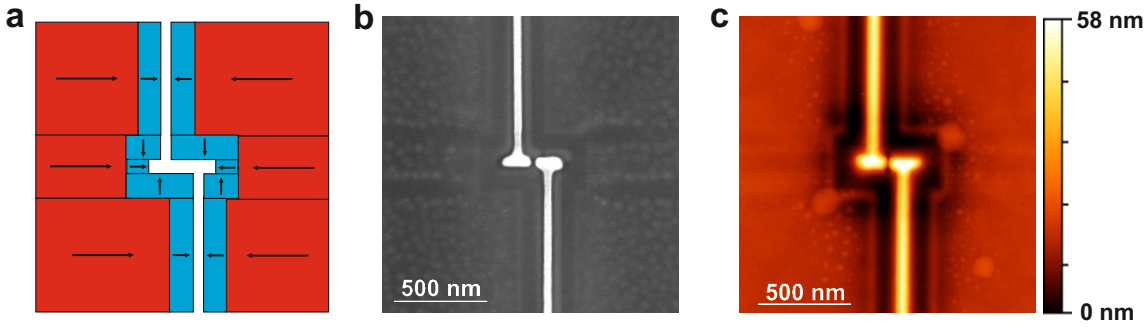

Figure 3.5: FIB milling of connected antennas. **a** Specified 3-level milling pattern. **b** Electron micrograph of the connected antenna fabricated by 3-level milling. **c** AFM image of the connected antenna fabricated by 3-level milling.

The AFM and SEM study demonstrate that the FIB fabrication results in structural dimensions very close to the desired geometries. The corners of the antennas are slightly rounded but width and lengths are exactly as specified. Strangely the inner layer is 15 nm deeper than the outer one, even though they were set to the same value. However this height difference can be easily avoided by setting the depth of the inner layer to a factor 0.8 smaller than the depth of the outer layer. In addition small particles reside at the region of the second layer. The height of these particles is less than 2 nm and they did not cause any artifacts in optical as well as electrical experiments. If desired, the amount of these particles can be reduced by increasing the overlap to 75% (standard is 50%) and increasing the dwell time to 10μs (standard is 1μs). Overlap refers to the overlap distance between adjacent milling pixels and is defined in percentage of the beam diameter. Dwell time is the time the beam is positioned at each pixel and consequently influences the number of times the beam has to pass by a pixel.

One of the most important parameters is the size of the gap, since this determines the achievable near-field intensity. For the above described situation, i.e. a flake with a thickness of 60 nm and a milling depth for the gap of 70 nm, a gap size of 20$\pm$5 nm is obtained. The gap size has been estimated from a cross-section of a high-resolution SEM image and the uncertainty arises from the tapered gap geometry. For a correctly aligned ion beam and a milling depth slightly larger than the flake thickness, a gap size of 20 nm can be reproducibly achieved. By reducing the milling depth to values smaller than the flake thickness, it is possible to obtain smaller gaps on the order of 6-8 nm. The problem with milling shallow and therefore narrow gaps is that small gold particles and/or Gallium ions can reside in the gap. This is a serious issue for electrical measurements and is discussed in more detail in Chapter 5.5. It should be noted that lately Zeiss has introduced a Helium-Ion Microscope, which can most likely produce smaller and cleaner gaps due to the smaller size and chemical properties of Helium ions compared to Gallium ions.

The general conclusion of this chapter is that, by using single-crystalline gold flakes and after optimal ion beam alignment, nanostructures with well-controlled shape are

obtained. The milling strategy strongly depends on the geometry but a few guidelines should be followed. Milling of very narrow gaps is discussed in more detail later, but gaps of 20 nm can be achieved and lead to reproducible electrical and optical properties.

3.1.5 AFM nanomanipulation

The Atomic Force Microscope (AFM) nanomanipulation shown in this thesis was conducted with a Veeco Dimensions 3100 machine, which is the property of the Experimental Physics 6 at the University of Würzburg. First tests of AFM nanomanipulation were performed together with the group of Dr. Berger at the Max-Planck-Institut für Polymerforschung in Mainz, also using a Veeco Dimensions 3100 machine.

In Figure 3.6a the working principle of the manipulation is sketched. An AFM tip is brought into close vicinity of the object and a specified movement pushes or pulls the object to the desired position. In order for the movement to be precisely along the specified direction the AFM must be equipped with a closed-loop piezo scanner. For the manipulation it is important to choose a suitable cantilever, which is flexible in order to take images in tapping mode[4] and still stiff enough for the manipulation to be successful. It was found that cantilevers (OMCL-AC240TSE, Olympus) with a spring constant of 2 N/m and a resonance frequency of 70 kHz gave good results. The material of the cantilever should be firm and should be chosen such that it does not show any adhesive properties with respect to the object, which is to be manipulated. In this thesis gold nanoparticles were moved and it was found that silicon is a good material choice for the cantilever.

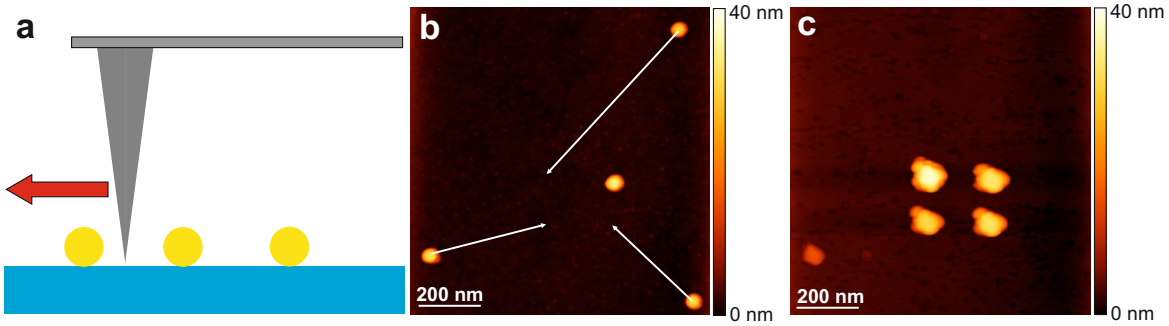

Figure 3.6: AFM nanomanipulation. **a** Schematic illustration of the working principle. **b** Spherical gold nanoparticles before manipulation. White arrows show the desired movements. **c** Nanoparticles after the manipulation. The tip has degraded during the manipulation, leading to tip artifacts in the image. Likely a piece of the broken tip can be seen on the bottom left.

Prior to manipulation, tapping mode images are obtained in order to locate the desired object before and after movement. Once the object is located, the tip is lowered to the surface and the movement is specified as illustrated by the white arrows

[4] Contact mode is not suitable since it would move the objects during imaging.

in Figure 3.6b. A tip velocity of 1 μm/s was found to give good results. In tapping mode the cantilever oscillates above the substrate and is bent when it touches the surface. Consequently, when performing movements perpendicular to the cantilever an offset of about 50 nm must be taken into account.

As discussed in Chapter 3.1.2 the gold nanoparticles are stabilized with an organic surfactant layer, which can stick to the glass substrate. For this reason it is essential to expose the sample to an oxygen plasma prior to manipulation.

In Figure 3.6c the nanoparticles are shown after the successful manipulation. Overall the procedure consisted of ten manipulation steps and sequential tapping mode images. The manipulation was performed without feedback at a distance slightly above the substrate. For manipulation without feedback, typically the sharp AFM tip breaks during one of the first movements. A piece of the broken tip can be seen on the bottom left of Figure 3.6c. In addition the degraded tip leads to tip artifacts in the scan image. Nevertheless, it was found that for a slightly degraded tip the success rate of the desired movements is higher (up to 80%) than for a sharp tip. It should be noted that a manipulation with feedback is also possible. However, in some cases a strong adhesion of the particles to the substrate was observed and manipulation was only possible without feedback.

3.2 Characterization techniques

3.2.1 Finite-Difference Time-Domain simulations

Numerical simulations are an important tool when studying plasmonic nanostructures. One reason is that analytical solutions are accessible only for few geometries. In addition the fabrication of nanostructures is time-consuming and expensive. Consequently, concepts are often tested in simulations before the experiments are performed. Even for relatively simple structures the interpretation of experimental data may require a comparison to simulation results in order to draw solid conclusions. Lastly, not all relevant properties, e.g. near-field intensity and spatial distribution are always experimentally accessible.

All classical electro-dynamical effects are described by Maxwell's equations and a variety of algorithms exist for solving them. Popular techniques are the finite element method (FEM), discrete dipole approximation (DDA) or finite-difference time-domain (FDTD). A good overview about the different techniques is given in [214]. Within this thesis the finite-difference time-domain (FDTD) algorithm is used. The choice is justified because, as shown in the second part of this chapter, FDTD gives highly accurate results and the commercially available software (FDTD Solutions, Lumerical Corp., Vancouver, CAN) is easy to use.

The main idea of the FDTD algorithm is to discretize space into rectangular cubes for which electric and magnetic field components are calculated in a time-stepping fashion. In this chapter emphasis is put on practical aspects and for details of the algorithm the reader is referred to the text book of Taflove [215]. In addition an excellent documentation of the software can be found online [216]. In Figure 3.7 the

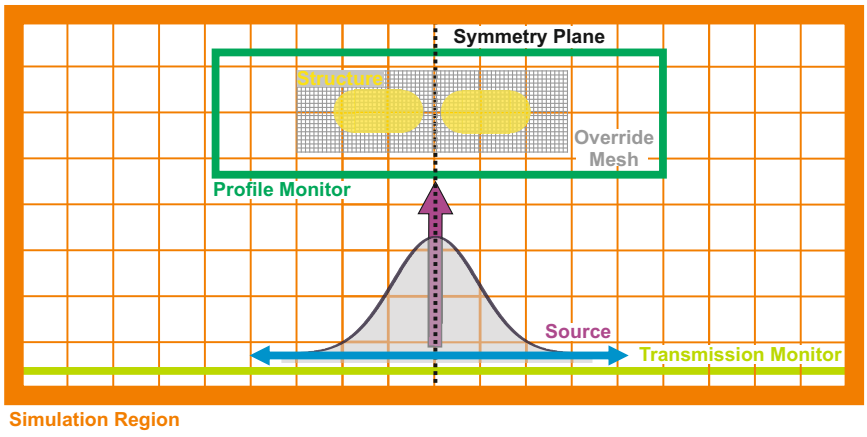

Figure 3.7: FDTD simulation setup. In the simulation region space is discretized into mesh cells, as indicated by the orange lines. In regions containing metallic structures a finer mesh is required and an override mesh is placed. Suitable symmetry planes should be used at the boundaries. Otherwise, the simulation is terminated by PML layers. Electromagnetic fields are injected by a source and are recorded by monitors.

basic simulation parameters are illustrated and will be discussed in the following. In order for the problem to be numerically tractable a finite **simulation region** must be specified. Typically the simulation is chosen to have a spacing on the order of the excitation wavelength between structure and boundary, such that electromagnetic fields have small amplitudes at the boundary. The reflection of remaining electromagnetic energy at the boundary leads to errors and needs to be avoided. This is accomplished by introducing an artificial absorbing material, called perfectly matched layer (PML). If the structure reveals a symmetry, it is possible to impose this onto the boundary condition and consequently the simulation region is reduced by a factor of 2 for each symmetric or anti-symmetric boundary condition.

In this thesis the interest lies on the manipulation of light at the nanoscale by plasmonic structures. Since strong field gradients can be present in the vicinity of these structures the size of the **discrete mesh** cells must be small. In order to keep memory requirements within the available resources the mesh cells are chosen to be non-uniform in size. In regions containing metallic structures the mesh is refined by a **mesh override** region with a typical cell size of 1 nm^3. In regions without metallic materials the grid size has a span of 20 nm in each direction. Within the limits of the discrete mesh it is possible to specify any arbitrary **structure geometry**. The materials involved in the simulations are Gold, Indium Tin Oxide (ITO) and glass. The **dielectric functions** of glass and ITO are assumed to have constant values of n=1.4 and n=1.7, respectively. The dielectric function of gold has a strong wavelength dependence, which must be taken into account. Most commonly the experimental data by Johnson and Christy [51] are used. However, FDTD is a time domain algorithm and it is not possible to specify an arbitrary dielectric function. The software used in this thesis applies a multi-coefficient model [216] to obtain an analytical expression. In order to make the automatic fitting of the software more robust the material data is specified by an analytic fit [217][5] to the data of Johnson and Christy. It is important to keep in mind that the measured values for the dielectric function of gold depend on the respective fabrication technique and different values are obtained by different authors, see [219] for an overview and a recent measurement. Consequently, some uncertainty is introduced when the dielectric function is taken from the literature. Electromagnetic energy is injected into the simulation region via a **source**, which can be a dipole, plane-wave, Gaussian or total-field scattered-field (TFSF) source. The choice depends on the specific situation and will be motivated in the corresponding chapters. For all simulations the source has been specified in the time domain and a pulse length of 3 fs is used, corresponding to a wavelength span of about 250 nm. In the simulation sources are generated by currents. Since these currents run over a few mesh cells, the fields in the very vicinity, i.e. 4-5 mesh cells in each direction of the source are unphysical. During the simulation the electromagnetic fields are calculated at every space coordinate for every time step. Storing all these data is not possible and one-, two- or three-dimensional sub-regions, called **monitors**, need to be specified in which the fields are recorded. Monitors are used to obtain the near-field intensity distributions of the plasmonic structures as well as to measure the radiated or absorbed power. The simulations are automatically terminated when the energy

[5]Note the erratum [218] to this publication.

in the simulation region falls below 10^{-8}. At this point the fields, which have been calculated in time domain so far, are Fourier-transformed to frequency domain.

This chapter is concluded by discussing the accuracy and sources of errors in FDTD simulations. Numerical errors cannot be avoided and reducing errors typically increases simulation time and memory requirements. It is therefore important to know to what extend certain parameters influence the simulation results. This topic is treated in detail by the supplier of the software and is available online [216]. The most important types of errors are discussed in the following. The first type of error stems from evanescent fields overlapping with the simulation boundary. Electromagnetic energy can be lost if the simulation region is too small and too few PML layers can lead to artificial reflection. However, by using a simulation size of twice the excitation wavelength and a minimum of 20 PML layers this type of error becomes negligible. The second type of error is caused by dispersive material properties, as discussed above, and a modeling of the dielectric function is necessary. The error introduced by fitting the dielectric function is small. However, the deviations for the different dielectric functions of gold stated in the literature, i.e. Palik [220] or Johnson and Christy [51], lead to a significant error of about 4%. The last type of error is associated with the mesh. The finite spatial mesh does not fully resolve the geometrical feature of the structures. For very fine features, such as small gaps, this becomes the dominant error in the simulation. Moreover, when using curved surfaces sharp corners are introduced by the rectangular mesh (called staircasing) and can lead to unphysical high field intensities. For extremely small mesh sizes errors can be introduced due to finite precision numbers, however this only starts playing a role for mesh cells 10^7 times smaller than the excitation wavelength, i.e. 10^{-4} nm for λ=1 μm.

In general, it is necessary to investigate the numerical error for every simulation setup. In most cases the exact solution to the problem is not known. This requires convergence test in order to find a good compromise between accuracy and simulation time or memory requirement. Such a convergence test is presented in Figure 3.8 for the scattering cross-section σ of a sphere with a diameter of 100 nm situated in vacuum. For this geometry the exact solution is known from Mie theory (see Chapter 2.1.2) and is compared to the numerical result for mesh sizes from 5 to 0.8 nm. In Figure 3.8a the scattering cross-section is plotted as a function of wavelength for the analytical solution and FDTD simulations using a mesh size of 5 nm and 0.8 nm. For the 0.8 nm mesh the numerical result is almost identical to the analytical solution and for the 5 nm a clear deviation is visible, although the rough qualitative behavior is still captured. The near-field intensity distributions are shown in Figure 3.8b where staircasing is clearly visible for the 5 nm mesh and leads to unphysical hot spots.

A quantitative analysis is done by calculating the error for the different simulations as:

$$\Delta\sigma = \sqrt{\frac{\int (\sigma_{fdtd} - \sigma_{theory})^2 \, d\lambda}{\int (\sigma_{fdtd})^2 \, d\lambda}} \tag{3.1}$$

The result is shown in the inset of Figure 3.8a together with the memory requirement. The error for the 5 nm mesh cell is 15%, but is reduced to 0.3% for the 0.8 nm mesh. However, the memory requirement strongly increases with decreasing mesh size and for the 0.8 nm mesh 6 GB of memory are required.

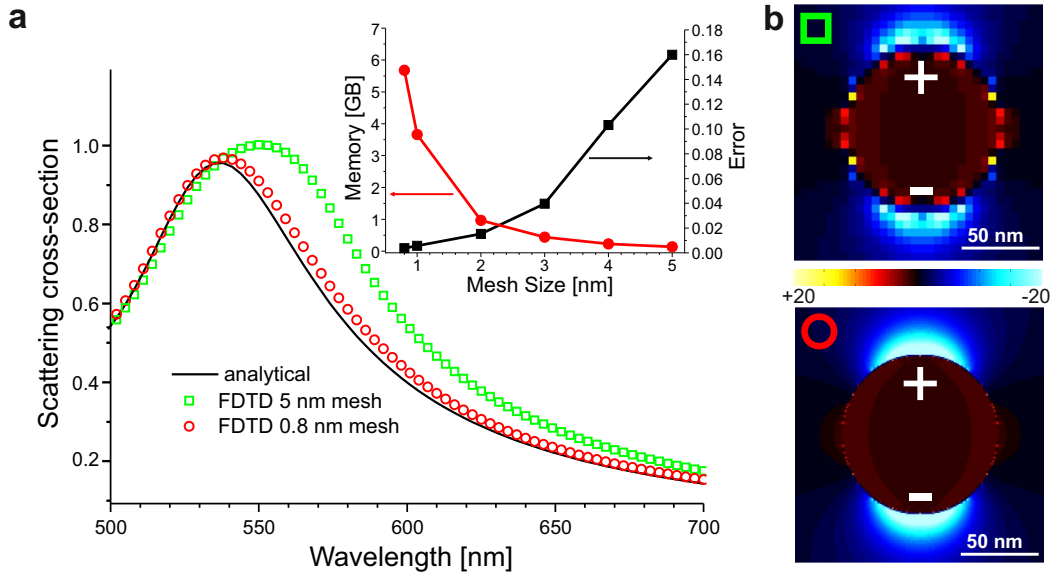

Figure 3.8: FDTD convergence test. **a** Scattering cross-section of a sphere with a diameter of 100 nm. The analytical solution from Mie theory (solid line) is compared to the result from the FDTD simulation using a mesh with 5 nm edge length (green squares) as well as a 0.8 nm mesh (red circles). The inset shows the error to the analytical solution as well as the memory requirement for the simulation as a function of mesh size. **b** Near-field distributions for a 5 nm (top, green square) as well as 0.8 nm (bottom, red circle) mesh.

From this study it becomes clear that accurate results can be obtained from FDTD simulations. Further there is a tradeoff between accuracy and requirements on computer hardware. Within this context one should keep in mind that there are also fabrication errors as well as uncertainties in the experimental measurement and for most plasmonic applications it is not necessary to reduce the simulation accuracy to less than 5%.

3.2.2 Dark-field white light scattering microscopy

Various techniques exists for the characterization of plasmonic resonances and involve photons/electrons for excitation/detection. A good overview of the currently established microscopy techniques is given in [221]. In this thesis plasmonic nanostructures are characterized by dark-field scattering. Dark-field scattering uses far-field photons for excitation and detection. The main advantage of this technique is its simplicity. Scattering is a well understood linear process and the interpretation of the experiment is straightforward. This is particularly important in Chapter 4 where one of the first experiments on plasmonic structures with atomic-scale gaps is presented.

Even though dark-field scattering is well established and commercially available,

most setups studying single particles use a symmetric illumination. In order to excite modes of all symmetries a setup with an asymmetric illumination was designed. This home-built setup is sketched in Figure 3.9 and will be described in the following. The light of a halogen lamp is coupled into a multi-mode fiber. The end of the fiber acts as a point source and the light is collimated by a lens. An iris is used to obtain a needle-like beam with a diameter of about 2 mm. The needle beam is parallel to the optical axis but is displaced from it so that it hits the microscope objective (Plan-Apochromat, 63x, NA = 1.4, Zeiss) at the edge. The beam is therefore injected at an angle larger than the critical angle and undergoes total internal reflection at the sample surface. A polarizer (LPVIS, Thorlabs) in the excitation beam path transmits only s-polarized light in order to avoid out-of-plane field components. Nanostructures scatter light into a broad angular range, which is collected by the same objective while the reflected excitation beam is blocked by a small beam stop. An analyzer (LPVIS, Thorlabs) is used to select the polarization of the scattered light in front of the entrance slit (200 μm) of the spectrometer (ACTON SpectraPro 2300i, 150 lines per mm grating blazing at 500 nm or Shamrock 303i, 80 lines per mm grating blazing at 870 nm). The dispersed photons are detected with a back-illuminated charge-coupled device (DV434-BV, Andor) or an electron-multiplied charge-coupled device (iXon A-DU897-DC-BVF, Andor). All spectra shown in this thesis are corrected for background. The spectral dependence of the halogen lamp, microscope objective, beam splitter, grating and CCD camera has been taken into account.

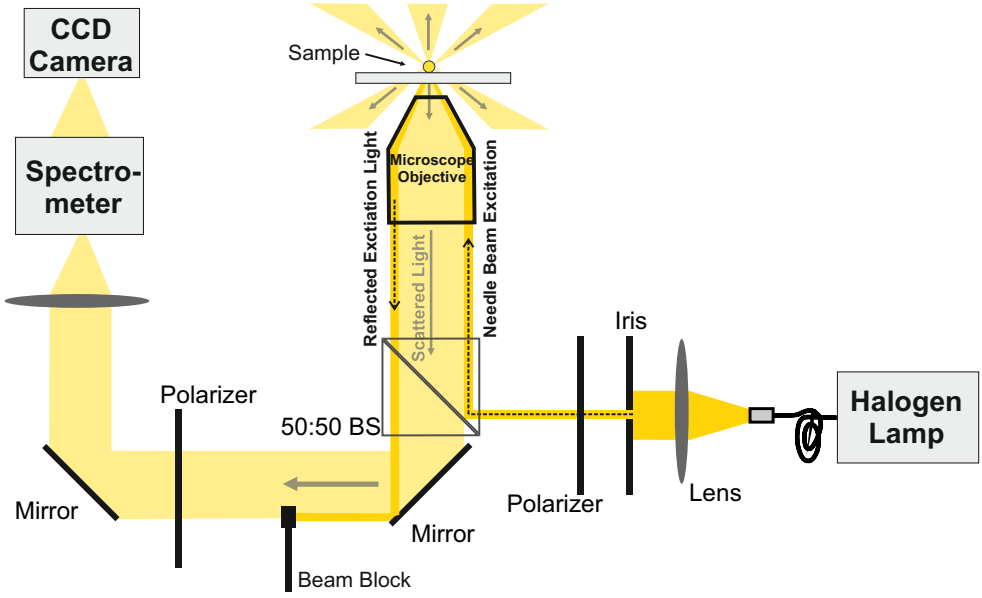

Figure 3.9: Simplified sketch of the optical dark-field scattering setup.

In order to test the performance of the asymmetric white light scattering setup an array of nanorods is investigated. The nanorods are fabricated by FIB milling of a single crystalline flake. In Figure 3.10a an electron micrograph of the array is shown. The rods are 50 nm wide and have a height of 50 nm. The length of the rod is scanned from 80 nm to 480 nm. The individual rods can be clearly identified in the dark-field

scattering setup and appear as isolated bright spots in the image (Figure 3.10b). It should be noted that the asymmetric excitation geometry leads to a spatial dependence of the excitation power and excitation spectrum. For a quantitative comparison the reference spectrum must be taken from the same pixel area as the investigated structures. The obtained scattering spectra of the five shortest rods are shown in Figure 3.10c. A pronounced peak is observed for all structures and as expected the scattering peak shifts to longer wavelengths with increasing rod length. In chapter 2.1.3 the optical properties of nanorods have been discussed in a numerical study and a Fabry-Pérot model was used to understand the different resonance orders. In the experimental study, due to the asymmetric excitation, higher order resonance can be excited and the resonance position as a function of rod length is plotted in Figure 3.10d for the first, second and third order longitudinal resonance. In addition, the results from the numerical study presented in Figure 2.4a are shown as solid lines. Since the fabricated structures have a slightly different geometry than the simulated ones a small offset is observed between experiment and theory, however a qualitative agreement is clearly observed.

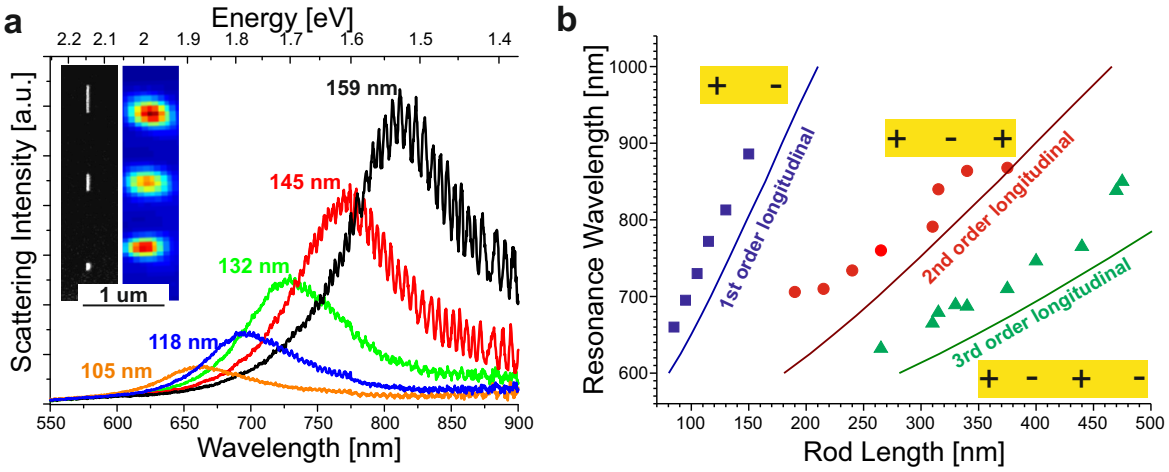

Figure 3.10: Dark-field scattering of gold nanorods. **a** Dark-field scattering spectra of five nanorods with 50x50 nm^2 cross-section and lengths ranging from 105 to 159 nm. The inset shows an electron micrograph and scattering image of the nanorod array. **b** Resonance wavelength versus rod length for 1st, 2nd and 3rd order longitudinal resonance. Symbols are experimental data and solid lines represent the calculated resonance wavelengths from a Fabry-Pérot model.

3.2.3 Electrical characterization

The electro-optical experiments on plasmonic nanostructures require a stable and reproducible electrical contact. To this end single-crystalline gold flakes are transferred to the electrode structure, which was introduced in Chapter 3.1.1. The transfer is performed by a BeCu probe needle (Semprex Corp., Campbell, USA) mounted onto a

probehead (PH100, Süss distributed by Cascade Microtech, Beaverton, USA) and was mainly conducted by René Kullock using the following procedure: First, gold flakes are deposited onto a clean glass substrate. This substrate is brought next to the substrate containing the electrode structure and a large droplet of ethanol is deposited such that it covers both substrates. The edge of the flake is carefully pushed with the needle so that it slightly bends upwards. The needle is then brought in contact with the slightly deformed edge and the flake is carefully peeled off the substrates. The electrode structure is then positioned below the needle by a translational stage and the flake is brought in contact with the electrodes. After the droplet has dried the sample is rinsed in ultrapure water and is plasma-cleaned. Figure 3.11a shows a gold flake transferred to an electrode structure. The deformed edge from the transfer process is visible. Otherwise the surface of the flake takes on the shape of the electrode structure and consequently a good mechanical contact is established.

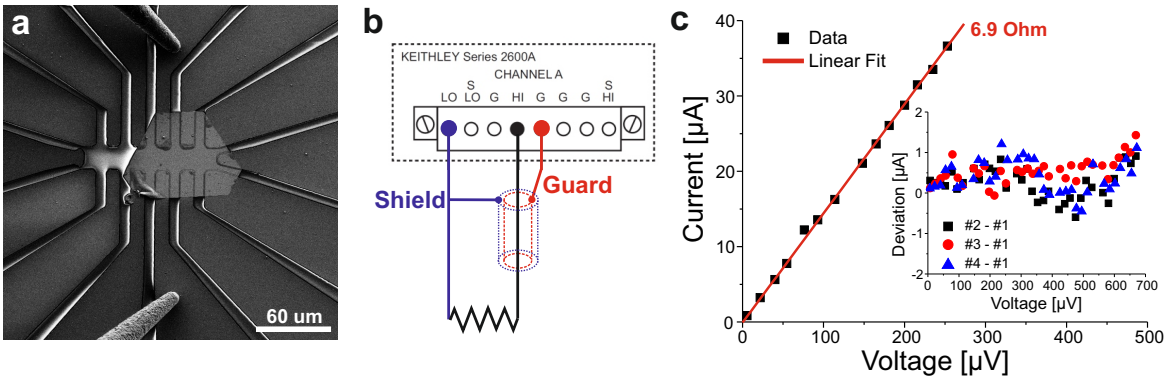

Figure 3.11: Electrical characterization. **a** Electron micrograph of a gold flake transferred to an electrode structures. Probe needles for electrical measurement can be seen at the top and bottom. **b** Schematic of the electronic setup. **b** Current-voltage characteristic of the flake shown in **a**. Symbols are the experimental data. The solid line is a linear fit from which a resistance of 6.9 Ohm is obtained. The inset shows the deviation from consecutive measurement to the first measurement.

In order to characterize the electronic contact the resistance over the flake was measured between the top and bottom BeCu probe needles (see Figure 3.11a) which are attached to nanomanipulators (MM3A, Kleindiek Nanotechnik, Reutlingen, DE) situated inside the vacuum chamber of the Zeiss electron microscope. The BeCu have a tip radius of 6 μm (if necessary the needles can be further sharpened by FIB milling) and were found to be the most suitable choice. Tungsten needles oxidize within a few days, which leads to high contact resistance. Electro-chemically etched gold tips were found to bend upon contacting. The electrical measurements were performed by a source measure unit (SMU) (Keithley 2601A, Keithley Instruments Inc., Cleveland, USA) using a guard and noise shield as depicted in Figure 3.11b. The current-voltage characteristic of the contacted gold flake shows a linear behavior and a resistance of 6.9 Ohm is obtained from a linear fit (Figure 3.11c). The data has been corrected

for the internal current offset of the SMU. The reproducibility of the contact is tested by lifting the needles and bringing them back into contact. This is done 3 times and the deviation from the first measurement is shown in the inset of Figure 3.11c. The deviation is about 1 μA and it can be concluded that a good electric contact is reproducibly achieved. It should be noted that evaporating contacts on flakes using electron-beam lithography also showed low-ohmic and reproducible electric contacts, however this procedure was more time-consuming. Direct contacting of flakes with probe needles turned out to be difficult, since the gold flakes are often damaged upon contacting.

The electrical properties of single- in comparison to multi-crystalline structures was also investigated. The resistance of a continuous 4 μm long single-crystalline gold wires with cross-sections of 60x60 nm^2 has a typical value on the order of 100 Ohm. Similar values are obtained in the literature [222]. On the other hand the resistance of multi-crystalline wires with similar dimension is on the order of 1000 Ohm. A systematic comparison between single-crystalline and multi-crystalline structures by 4-point measurements would be an interesting study. Nevertheless the 2-point measurements already clearly show the superior electrical properties of single-crystalline gold structures.

4 Plasmon resonances in atomic-scale gaps

The interaction of light and matter can be considerably enhanced in the presence of optical near-fields. Plasmonic gap modes in resonant metal-insulator-metal (MIM) structures provide the ability to concentrate optical fields into the insulating gap, leading to a strong localization as well as enhancement of optical fields. Consequently, pairs of metal nanoparticles with small gaps have gained much attention and are widely used in many applications such as single-emitter surface-enhanced spectroscopy [13, 22, 223–225], quantum optics [30, 226], nonlinear optics [14, 122, 227], optical trapping [228] and molecular opto-electronics [229]. The success of resonant MIM structures is based on two fundamental properties of their antisymmetric electromagnetic gap modes. (i) As a direct consequence of the boundary conditions, the dominating field components normal to the metal-dielectric interfaces are sizable only inside the dielectric gap. (ii) Since the free electrons of the metal respond resonantly to an external optical frequency field, enormous surface charge accumulations, accompanied by intense optical near fields, will occur. In addition, with decreasing gap width, stronger attractive coulomb forces across the gap lead to further surface-charge accumulation and a concomitantly increased near-field intensity enhancement.

The superior performance of antennas with small gaps has also been seen in Chapter 2.1.5, where emitters have been coupled to different antenna geometries. The highest enhancement of the radiative decay rate has been obtained for a gap antenna and a strong increase of the radiative decay rates was observed for decreasing gap size. Therefore plasmonic gap antennas with smallest gap seem to be the ideal candidates for the enhancement of light emission from quantum emitters. However, within a classical description ever-decreasing gap widths would lead to ever-increasing field enhancements, finally resulting in a singularity [230, 231]. Recent theoretical work [52, 232, 233] suggest that including quantum effects, such as electron tunneling and a non-local dielectric function, removes this singularity and set a limit to the achievable field enhancement. At the beginning of this thesis little was known about the optical properties of plasmonic nanostructures with atomic-scale gaps and at what gap sizes quantum-mechanics starts to affect plasmon resonances. Experimental investigation of these aspects is of fundamental interest to the field of plasmonics and enhanced light-matter interaction.

The outline of this chapter is as follows. This chapter starts with an identification of the challenges which need to be addressed to study plasmon modes with atomic-scale dimensions. The challenges are structural control over atomic-scale dimensions as well as control over optical modes. They will be addressed individually in the following sections. The last part of this chapter discusses the role of quantum effects in the presented experiments as well as in recent publications.

The results of this chapter have been published in [234]. Most parts of the text and all graphics are taken one-to-one from this publication.

4.1 Challenges and main idea

Near-field intensity enhancement and spatial confinement of optical fields form the basis of enhanced light-matter interaction. However, a quantitative measurement of either property is an enormous challenge. Obtaining an absolute value of the near-field intensity requires a calibrated detector and has been reported for a method exploiting photo-polymerization and subsequent AFM measurements of the developed polymer [56, 57]. This method is clearly difficult to apply to atomic-scale gaps. The difficulties of a measurement of the spatial confinement of optical fields will be illustrated in the following. It is worth to start with the simple measurement on the amount of confinement for a macroscopic system, e.g. a laser pointer. If one would like to determine the spot size of this laser pointer one could shine it on a sheet of paper, position a ruler across the spot and detect the scattered light with the human eye. The simplicity of this experiment lies in the fact that light source, sample and detection system are far apart and are not influencing each other. However, severe difficulties start to appear for nano-optical systems, which confine light to dimensions much smaller than the diffraction limit. Since such strongly localized optical fields can only exist in the vicinity of matter, either light source or detection system need to be very close to the sample and the sample will act back on the source/detector. Imagine a sharp metal tip with a strongly localized field of 1 nm^3. To investigate this strongly localized field we could bring a small scattering object e.g. a metal nanoparticle into the localized field, i.e. within 1 nm distance of the sharp metal tip. However, at this distance Coulomb interaction between the charges in the tip and the charges in the nanoparticle would alter the charge distribution within both objects so significantly that it is inadequate to assume this configuration to consist of two individual systems and only information of the coupled system can be obtained (see also Chapter 2.1.4 for the coupling of two metal particles). A clear distinction between source, sample and detector is therefore not possible and the interaction of the respective elements must be taken into account.

However, the interaction of two metal particles is distance dependent and it should be possible to infer from the properties of the coupled system to the distance. As shown in Chapter 2.1.4 the coupling of two closely spaced metal particles leads to the formation of a symmetric and anti-symmetric Eigenmode, i.e. mode hybridization. For the symmetric mode charges are repelled from the gap region and its resonance is shifted to higher energies with respect to the uncoupled system. Due to its charge distribution the symmetric mode does not provide a localization to the gap. On the other hand, the anti-symmetric mode exhibits an attractive Coulomb force over the gap, resulting in strongly enhanced and localized fields within the gap region. The resonance wavelength of this mode is shifted to lower energies. Since the Coulomb interaction is distance dependent, the hybridization splitting between the corresponding symmetric and anti-symmetric mode provides a measure for the interaction of surface charges across the gap. A large splitting indicates a strong confinement and enhancement of the electric field of the antisymmetric mode. Consequently, information about confinement and enhancement are encoded in the hybridization splitting and it is not necessary to use an external probe.

In order to obtain the hybridization splitting a suitable symmetric/antisymmetric

mode pair must be identified from the various distinguishable symmetric and antisymmetric modes [78] of side-by-side aligned nanorod dimers. By using a dedicated optical scattering setup, dark and bright modes of all symmetries can be efficiently excited, in contrast to previous work on similar structures [62, 77]. By considering the resonance wavelength and angle-dependent emission characteristics the respective modes can be precisely identified by numerical FDTD simulations. Comparing experimental scattering spectra to numerical simulations allows for a calibration of the gap width from the hybridization splitting. Once the gap size is calibrated, information about the corresponding near-field intensity and confinement can be obtained by means of numerical simulations. The identification of the optical modes and realizing the role of the hybridization splitting has posed a first challenge which has been met by a **full control over optical modes**. This challenge will be discussed in detail in Section 4.3.

A second challenge was to find a way to fabricate atomic-scale gaps in a controllable manner. Already the fabrication of structural features of less than 10 nm is challenging using conventional lithography [82, 235]. However, recently several novel methods have been developed to obtain stationary as well as tunable atomic-scale gaps. Stationary atomic-scale gaps can be obtained by self-assembly of colloidal particle pairs [79], by placing colloidal particles on top of metal films covered by a self-assembled monolayer [236] or by electromigration [143]. Structures with tunable gap widths can be created by means of scanning tunneling microscopy [237], shearforce microscopy [238] or by mechanical breakjunctions [239]. Even though it is not easy to obtain atomic-scale gaps, the real challenge is to achieve this in a reproducible and controlled way. In the region of high optical fields smallest deviations of the field-confining structure can significantly alter the optical properties and resonances become difficult to assign [79]. Consequently the actual geometry and crystal structure of the gap must be well controlled and characterized. Here, **structural control over atomic-scale dimensions** is achieved by using side-by-side aligned single-crystalline nanorods. These dimers are obtained from self-assembly and possess gap widths down to 0.5 nm. Details will be presented in Section 4.2.

4.2 Structural control over atomic-scale dimensions

This chapter demonstrates how structural control over atomic-scale dimensions has been achieved. In particular, SEM images of the investigated nanorod dimers are shown and the presence of atomic-scale gaps is demonstrated by means of high-angle annular dark-field scanning transmission electron microscopy (HAADF-STEM).

4.2.1 Self-assembly of nanorod dimers

Nanostructures with very small gaps were obtained by dropcasting chemically grown nanorods onto an ITO-coated glass cover slip with a prefabricated gold marker structure. Further technical details of the sample preparation technique can be found in Chapter 3.1. Prior to optical characterization the nanorod dimers are identified in a Scanning Electron Microscope, SEM (Helios Nanolab, FEI Company) and only the most symmetric dimers were selected. In Figure 4.1 all optically investigated dimers are shown. An intrinsic size distribution with lengths and diameters ranging from 62 to 78 nm and 25 to 32 nm is obtained from an analysis of the SEM images. The

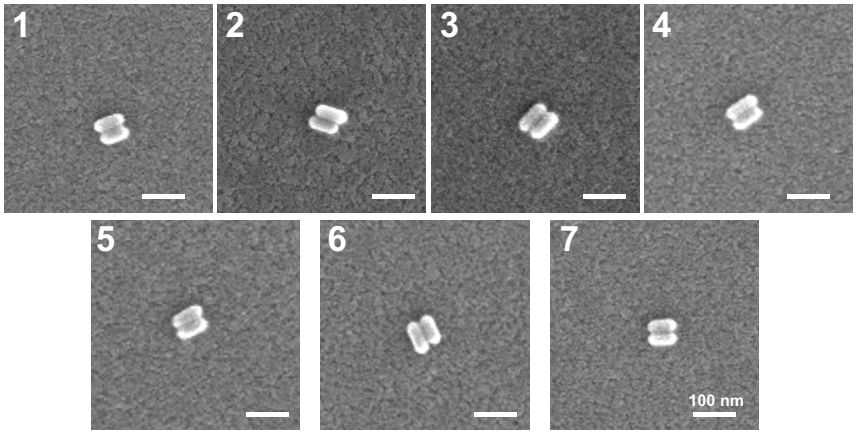

Figure 4.1: Electron micrographs of all optically investigated dimers. Copyright (2012) American Chemical Society.

characterization with SEM bears the advantage that it can be easily performed on the same substrate as the optical experiments. However, it is not possible to resolve the gap width by means of SEM. For this reason HAADF-STEM experiments are conducted, which are presented in the next chapter.

4.2.2 STEM analysis of structural dimensions

High-angle annular dark-field scanning transmission electron microscopy (HAADF-STEM) is a technique that allows for the three-dimensional recording of the crystal morphology [199]. Here, an FEI Titan 80-300 electron microscope with an acceleration voltage of 300 kV was used. The nominal STEM resolution of this microscope is 0.13 nm. The images analyzed for the gap width determination of gold nanorod dimers,

have been taken by Nadezda Tarakina and Martin Kamp at the Technical Physics, University of Würzburg, DE. Prior to imaging, the nanorods have been dropcasted to a holey carbon grid and have been exposed to an oxygen plasma to remove organic contamination. Figure 4.2 shows a typical HAADF-STEM micrograph of a nanorod dimer and a zoom to the gap region. To reveal the atomic structure the left rod was oriented along the [110] zone-axis.

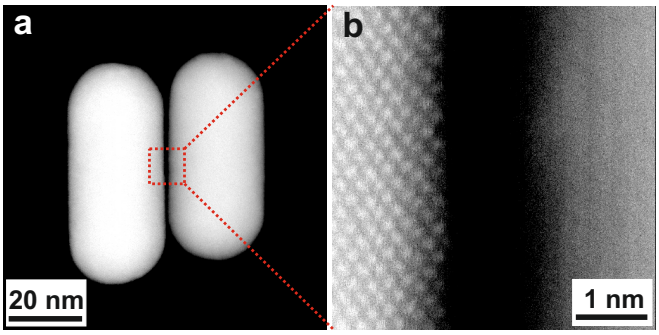

Figure 4.2: Characterization of a nanorod dimer by STEM. **a** Dimer consisting of two side-by-side aligned gold nanorods with diameter of about 30 nm and length of about 65 nm, each. **b** Zoom to the gap region indicated in a (dashed square). The atomic structure of the left nanorod is resolved. Copyright (2012) American Chemical Society.

For the gap width determination, the STEM images of twelve parallel aligned rods were analyzed. A correct alignment is important, since parallax can lead to an underestimation of the gap width (Fig. 4.3a). Therefore for each pair a series of images was recorded for different sample angles. The micrograph with maximum geometric gap was used for further analysis. As indicated by the green box in Fig. 4.3b, for each micrograph the center region spanning about 20 nm along the length of the rods and 30 nm around the gap was selected. This region consists of more than 200 cross sections of the gap, which were all independently analyzed by a nonlinear fitting routine using MatLab. It was found that a cylindrical curved surface is appropriate for fitting the region around the gap. In Fig. 4.3c exemplary cross sections at four different positions along the dimer and according fits are shown. The free parameters of the fitting function were the radii of the rods, centers of the rod and the HAADF signal per thickness. It should be noted that intensity variations on the HAADF-STEM images arise due to changes in chemical composition and thickness and can therefore directly be used to determine the gap width. The mean gap value and its variance has been calculated from the >200 cross-sections for each rod (Fig. 4.3d). Ten out of twelve structures had gaps between 0.5 and 2 nm, one pair (dimer 9) had a gap width too small to be determined and one outlier had a gap width of 3.5 nm. The average gap width for all structures was 1.3 nm. It should be noted that the rods may not be perfectly parallel in every dimer, however the angles between the rods were found to be smaller than 4 degrees in all cases. Besides small tilts, offset between the rods and rods of slightly different length are sometimes observed. Nevertheless, these small uncertainties do only slightly affect the resonance position, as will be shown later.

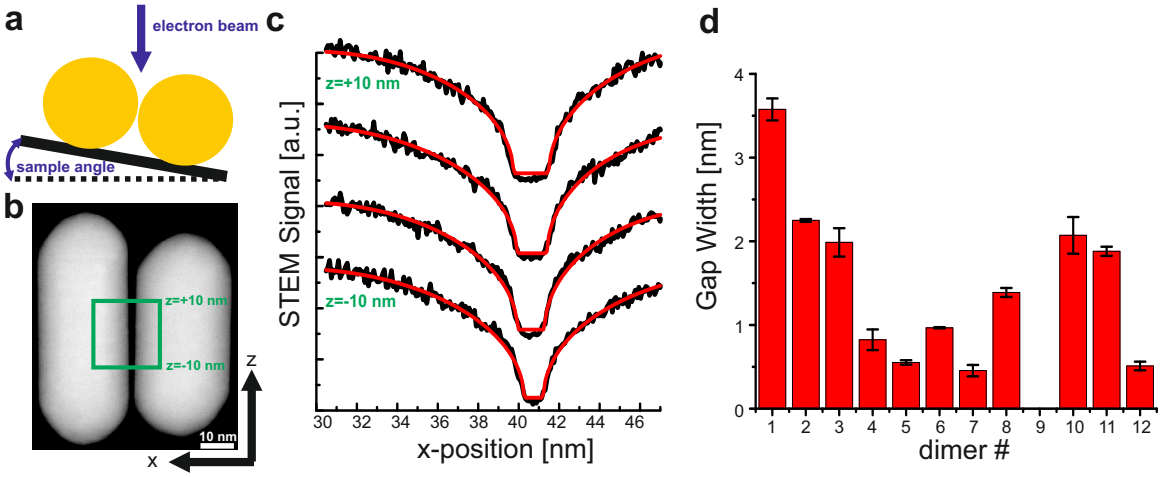

Figure 4.3: STEM study of the gap width of nanorod dimers. **a** Sketch illustrating the importance of correct alignment for estimation of the gap width. **b** STEM image of one of the analyzed rods. The green box illustrates the region used to obtain the cross sections over the gap. **c** Cross sections (solid black line) over the gap for different z-positions along the dimer. The solid red lines show the corresponding fit. **d** Mean gap width and its variance for each dimer as obtained from >200 cross sections. Dimer #9 had a gap width too small to be determined. Copyright (2012) American Chemical Society.

4.3 Control over optical modes

This chapter studies the optical properties of plasmon resonances in atomic-scale gaps by means of numerical simulations as well as experimental optical measurements.

4.3.1 FDTD simulations

Numerical Finite-Difference Time-Domain (FDTD) simulations provide a versatile tool for the investigation of plasmonic nanostructures (see Chapter 3.2.1). The simulations facilitate the assignment of the optical modes by combining the information on spectral position as well as polarization and angle-dependent radiation pattern. The effect of small structural uncertainties on the resonance wavelength and width can be easily investigated in the simulation, an important aspect for drawing conclusions about the role of quantum effects. Moreover, simulation results are used to calibrate the gap width of experimentally investigated nanorod dimers.

In the simulation the rods were modeled as cylindrical particles with spherical end-caps. The diameter of the rods was set to 30 nm and the length was set to 70 nm, in accordance with results from electron microscopy (Chapter 4.2.1). The substrate consists of a 200 nm thick ITO layer (dielectric material with n=1.7) on top of a thick SiO_2 layer (dielectric material with n=1.455). The dielectric constant of gold is modeled by an analytical fit to experimental data [217]. The minimal mesh size is set

to 0.1 nm^3. From a convergence series it has been found that the FDTD algorithm provides robust results, even for a small number of mesh cells in the gap. In particular resonance position and quality factor vary less than 2% when increasing the number of mesh cells from 4 to 10.

Mode Identification

The experimentally accessible wavelength range spans from 500 to 1000 nm, limited by the quantum efficiency of the CCD detector as well as the interband damping of gold. Within this range four characteristic resonances are observed for all numerically investigated gap widths of 0.3 to 3.6 nm. The simulated near-field distributions of these four modes are shown in Figure 4.4. Colored symbols are assigned to the modes and will be used throughout this chapter to provide a convenient labeling. The plus and minus signs in Figure 4.4 indicate the charge distributions. As expected only modes with an anti-symmetric charge distribution exhibit a strongly localized field within the gap. The coupled transverse mode (Figure 4.4a) and the longitudinal mode (Figure 4.4b) both are dipole modes of the coupled system. The remaining two resonances (Figure 4.4c,d) are assigned to the anti-symmetric hybridized counter part of the longitudinal mode as well as the 2nd-order anti-symmetric mode.

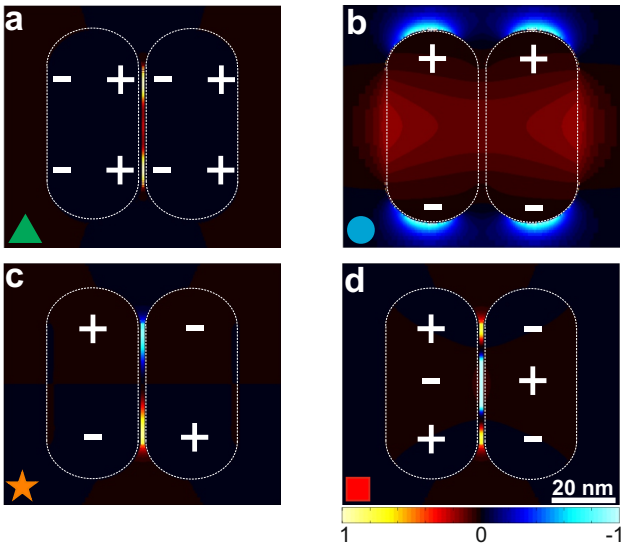

Figure 4.4: Numerical simulations of nanorod dimers. **a-d** Simulated normalized near-field intensity distributions of the coupled transverse (green triangle), coupled longitudinal (blue disk), 1st-order (orange star) and 2nd-order (red square) cavity Eigenmodes, respectively, for a nanorod dimer. A phase-sensitive representation of the dominant field component, sgn(phase(E))*E^2, is used. Copyright (2012) American Chemical Society.

These latter modes can also be interpreted as the first- and second-order mode of a "cavity" that consists of two rods supporting a highly localized MIM mode [240, 241] propagating along the gap and being reflected at the rod's ends [69]. Cavity

resonances occur for extended dimer lengths of $L = m\lambda/(2n_{eff})$, where m is the order of the resonance [68]. Due to the atomic-scale gaps the effective index n_{eff} can be as high as 14, resulting in a significantly shortened wavelength within the cavity. The combination of atomic-scale gaps and small effective wavelengths leads to unprecedentedly small modal volumes of 520 nm^3 for the second-order cavity mode (λ=628 nm), as calculated by the procedure presented in [242].

Polarization-dependent radiation pattern

The polarization dependent radiation patterns provide two important pieces of information. First, according to the reciprocity theorem the emission pattern reveals the most efficient excitation direction and polarization [6]. Second, the knowledge of the respective emission polarization allows to distinguish modes with a spectral overlap. The radiation patterns of all previously identified modes are shown in Figure 4.5.

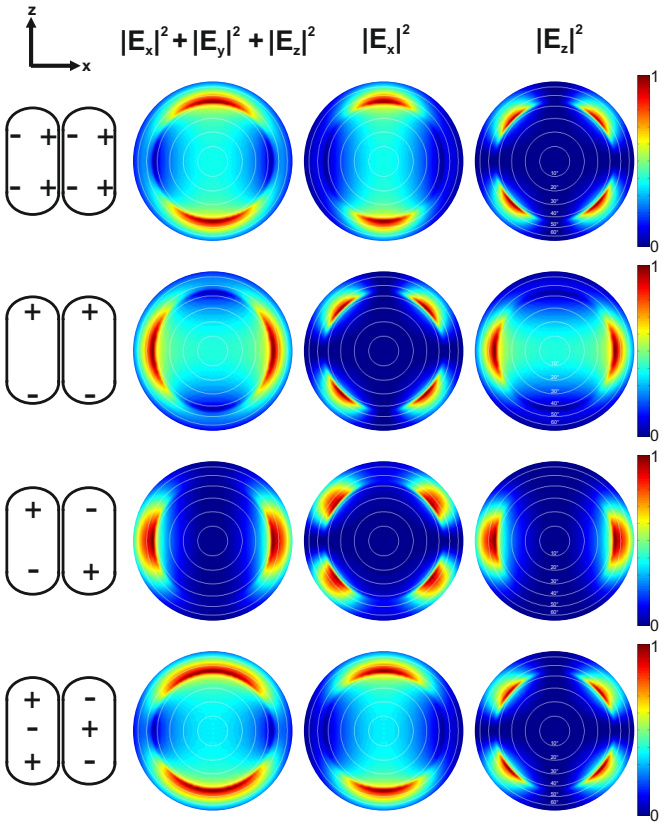

Figure 4.5: Polarization-resolved radiation pattern. Normalized simulated radiation pattern for coupled transverse, coupled longitudinal, 1st-order and 2nd order cavity mode (top to bottom). The radiation pattern have been projected to a hemisphere below the structures and white rings mark the emission angle in steps of 10°. Copyright (2012) American Chemical Society.

The dominating component determines the far-field polarization and E_x/E_z correspond to transverse/longitudinal polarization respectively. The radiation patterns

were obtained from a 22×22 μm^2 large frequency monitor placed below the structure, by applying a far-field projection onto a hemisphere. Since radiation patterns are insensitive to the gap width, a gap width of 10 nm has been chosen. All patterns are normalized to 1 for better visibility. Typical intensity ratios between two- and four-lobed patterns are on the order of 5.

Generally the far-field polarization of each mode is oriented parallel to the symmetric plane of a mode. For the coupled longitudinal/transverse mode such a plane obviously exists in the longitudinal/transverse direction, respectively. Accordingly, a transverse polarization is observed for the second-order cavity mode. The first-order cavity mode has two antisymmetric planes and its radiation is found to be polarized along the longitudinal direction. This mode radiates only weakly into angles normal to the substrate and consequently must be excited under an angle.

Effects of structural uncertainties

The HAADF-STEM analysis presented in chapter 4.2.1 has shown that even the robust side-by-side self-assembly leads to dimers with slightly variable geometries. Therefore the effect of small asymmetries such as tilts, offsets and different lengths on the resonance wavelength were analyzed. The second-order cavity resonance has been chosen for this study since it is most sensitive to structural asymmetries.

Figure 4.6a-d shows that these asymmetries lead to a slight distortion of the near-field intensity distributions. Of particular interest is the effect of structural asymme-

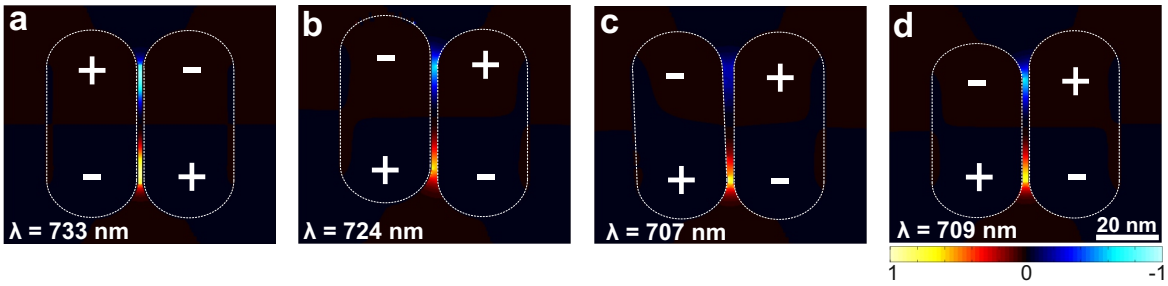

Figure 4.6: Influence of slight structural asymmetries on the optical properties of nanorod dimers. **a-d** Normalized near-field distributions. **a** Symmetric structure. **b** 5 nm offset between the two rods. **c** Tilting the left rod by two degree. **d** Rods with a length difference of 5 nm. A phase-sensitive representation of the dominant field component, sgn(phase(E))*E^2, is used. Copyright (2012) American Chemical Society.

tries on the resonance wavelength and the respective resonance wavelengths are stated in Figure 4.6a-d. With respect to the symmetric structure the following shifts are observed: 9 nm for the geometry with an offset (b), 26 nm for the tilted structure (c) and 24 nm for the structure with different rod length (d). Considering the broad resonances these uncertainties are relatively small. Nevertheless, they must be taken into account for a precise interpretation of experimental data.

4.3.2 Polarization-resolved mode characterization

Numerical simulations have revealed all optical modes of nanorod dimers in the visible wavelength range and their radiation patterns. These information are required to interpret the experimental scattering spectra, which are presented in this chapter. Optical characterization of nanorod dimers was performed using an asymmetric white-light dark-field scattering scheme employing an off-axis needle-like beam to enable efficient excitation of dark and bright modes of all symmetries [76]. In Chapter 3.2.2 the design of the setup has been presented and it was shown that higher-order dark modes of individual nanorods can be excited. Polarization-resolved scattering spectra of a nanorod dimer are shown in Figure 4.7. Within the observation window (500 to 1000 nm wavelength) four resonances are observed. Two resonances exhibit an emission polarization along the transverse axis (green triangle, red square) of the dimer, while the other two resonances show a longitudinal polarization (blue disk, orange star). The resonance wavelength is obtained by fitting a Lorentzian line shape to each peak. Taking resonance position and far-field polarization into account, the observed resonances can unambiguously be identified as the coupled transverse (green triangle), coupled longitudinal (blue disk), first-order (orange star), and second-order (red square) cavity mode.

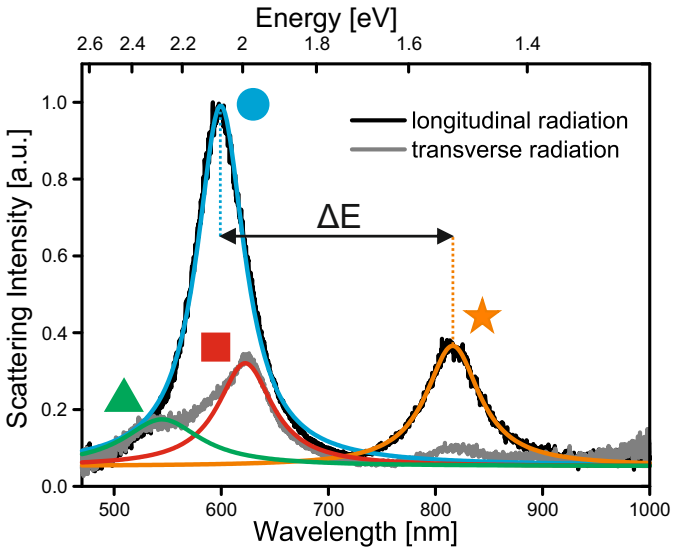

Figure 4.7: Typical experimental scattering spectrum of a nanorod dimer. Longitudinal (black) and transverse (gray) polarized detection with respect to the dimer's long axis. Four resonances are observed to which Lorentzian line shapes are fitted (full lines). The resonances are assigned to coupled transverse (green triangle), longitudinal (blue disk), 1st-order (orange star) and 2nd-order (red square) cavity Eigenmodes. The respective field distributions are shown in Figure 4.4. Copyright (2012) American Chemical Society.

The excitation efficiency of each resonance depends on the orientation of the struc-

ture with respect to the excitation plane and polarization [6]. Indeed the scattering intensity of each resonance can be tuned by varying the orientation of the nanorod dimer with respect to the excitation plane.

For all investigated structures, both cavity resonances and the longitudinal resonance could be easily identified according to their emission polarization and their resonance position. The scattering intensity of the coupled transverse mode is typically very weak, since it falls into a region where gold exhibits strong interband damping. Therefore, the weak transverse resonance could not always be identified with sufficient fidelity.

4.3.3 Gap calibration: atomic-scale confinement

After precise identification of the optical mode, the energy splitting (ΔE) of the hybridized pair, longitudinal and first-order cavity resonance can now be extracted from the data. It is worth recalling that the energy splitting is a measure of the coupling strength and depends on the gap width and the refractive index of the material inside the gap. In Figure 4.8 the energy splitting is plotted as a function of resonance position. The solid lines represent simulated dimers with different gap width and refractive index in the gap, whereas the symbols are the experimentally obtained values of all investigated dimers. Experiment and simulation agree well. For example, the characteristic crossing point between longitudinal and second-order cavity mode is observed, indicating that variation in the gap are indeed the dominant source of spectral shifts in the experiment. As a next step, the dependence of energy splitting on gap width is

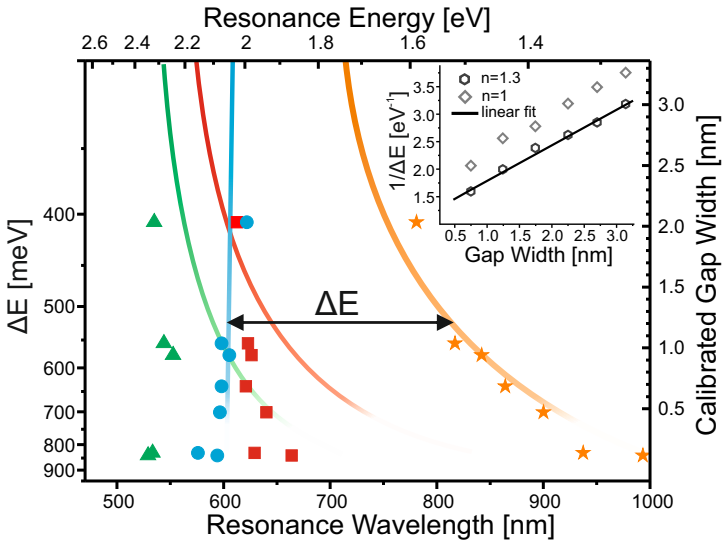

Figure 4.8: Gap calibration. Energy splitting versus resonance wavelength for the experimental data (symbols) and the simulated results (continuous lines). The gap width on the right is calibrated using the linear relationship (n=1.3) between inverse energy splitting ($1/\Delta$E) and gap width obtained by FDTD simulations (see inset). Copyright (2012) American Chemical Society.

numerically studied for the extreme cases of water (n=1.3) and no material (n=1) in the gap. The results are plotted in the inset of Figure 4.8. An approximately linear relationship between inverse energy splitting and gap width is found in the considered gap width range of 0.5 to 3.2 nm. For gap widths smaller than 0.5 nm, this relation becomes nonlinear. Each nanorod dimer therefore possesses an internal ruler that sensitively reports the gap width in a range of few up to tens of angstroms once calibrated by FDTD simulations.

Assuming a refractive index of n=1.3 in the gap, a gap width can be assigned to each investigated nanorod dimer (Figure 4.8). The resulting gap widths range from about 2 to <0.5 nm, which is in good agreement with the HAADF-STEM studies. Two dimers show extreme hybridization splittings of up to 800 meV, falling outside of the linear calibration regime. Qualitatively, the gap-width axis becomes stretched for splittings larger than 750 meV. These large splittings therefore suggest gap widths below 0.5 nm, which is close to the nearest-neighbor distance between gold atoms in the crystal lattice and consequently poses a lower limit for the gap width.

4.4 Quantum and non-local effects

The investigated dimers possess atomic-scale gaps with widths below 0.5 nm, a regime where non-locality of the dielectric function and electron tunneling are expected to influence plasmonic resonances. Non-local effects arise from electron-electron repulsion due to the Pauli principle. This quantum repulsion causes the electron gas to be resistant against compression by an external electromagnetic field, resulting in a pressure in the electron gas. The electron pressure is proportional to the Fermi velocity and can be included within a hydrodynamic description. It leads to an additional term within the dielectric function which depends on the wave vector. Consequently, in real space the electric field is related with the displacement field via a spatially dependent, i.e. non-local, dielectric function. Theoretical calculations, taking non-local effects into account, predict a blue-shift of plasmonic resonances [52] as well as a decrease in field enhancement [232]. In a recent experimental study [43] a good agreement to a non-local model has been claimed down to gap sizes of 0.5 nm, whereas a local model deviates for gap sizes below 1 nm. The investigated structures were gold nanoparticles on top of a multi-crystalline gold film. The distance between particle and film was controlled by a molecular spacer layer. The authors record scattering spectra and compare the resonance wavelength to a theoretical model.

The second quantum effect in nanoparticle dimers is electron tunneling from one particle to the other. In principle a full quantum mechanical simulation is required to include tunneling effects, which is computationally feasible only for low-density metal (e.g. sodium) particles with a size of a few nanometers. Nevertheless, by incorporating the tunneling conductance into the dielectric function in a quantum-corrected model [243] a reasonable agreement to the full quantum-mechanical simulation is obtained. Tunneling decreases the surface charge density at the gap, which leads to a lower field enhancement as well as a blue-shift of the resonance. However, tunneling only occurs for extremely small gap sizes and even for a gap size of 0.26 nm the reported bonding dimer plasmon blue-shifts by only 30 nm [233]. A recent experiment claims to achieve

gaps below 0.3 nm by pushing one metal tip against another [44]. In this study, optical scattering spectra are recorded as a function of gap distance and the onset of quantum tunneling is reported to occur for gap sizes of 0.3 nm. In another study, the electron energy loss spectra are studied as a function of distance between two gold particles [46]. The fact that the intensity of the dipolar resonance decreases and shows a less drastic red-shift than a classical model for gap widths below 0.5 nm was attributed to the observation of tunneling effects. Besides affecting the dipolar resonance, tunneling can lead to the occurrence of a charge transfer mode, which was observed for molecular tunnel junctions between two silver nanoparticles [45].

From these studies it can be concluded that for gap sizes larger than 0.3 nm the influence of quantum effects is rather small and causes resonance shifts on the order of tens of nanometers. These shifts could be measurable in a system with tunable gap width, under the condition that the individual particles remain constant, i.e. they are not deformed. When comparing different structures with variable, stationary gaps it is very challenging to observe such small resonance shifts with the necessary reliability and precision. In particular, an intrinsic variation in resonance wavelength can be caused by small variations in geometrical parameters (see Figure 4.6) as well as uncertainties in the dielectric function of material in the gap.

The data presented here shows extreme hybridization splittings, which points toward a rather small influence of quantum effects. However, it is interesting to note that systematic deviations between simulations and experimental data at small gap widths seem to be most pronounced for antisymmetric modes at higher energies. This finding is in agreement with simulation results taking into account non-local effects [52] as well as the above mentioned studies.

4.5 Conclusion and Outlook

In this chapter the rich mode spectrum of side-by-side aligned gold nanorod dimers has been investigated. STEM analysis of the dimers confirms the presence of atomically well-defined sub-nanometer gaps. The successful assignment of symmetric and antisymmetric modes allows to use the hybridization splitting between corresponding modes as a direct measure for the Coulomb interaction between surface charges across the gap. The observed splitting of up to 800 meV reveals the presence of atomically confined and resonantly enhanced optical fields in the dimer gap. In agreement to recent publications, the influence of quantum effects seems to remain small down to (at least) 0.5 nm. This is an important finding and good news for all studies concerning enhanced light-matter interaction.

The atomic-scale confinement and enhancement of visible light for the cavity modes as well as their spectral tunability and large sensitivity to the gap width, will have applications in various fields of research. In order to realize optical spectroscopy with near-atomic resolution, for example, exploiting Raman scattering, dimers with flat end-facets could be embedded in suitable tip structures for scanning probe microscopy. The small modal volume can lead to strong light-matter interaction and therefore sensing of molecular fluctuations in the gap, for example conformational changes or spatial diffusion, might be possible. The strong dependence of the resonance wavelength on

the gap will open new possibilities in the field of cavity optomechanics [244]. It is also conceivable that quantum-optical effects, like the so-called photon blockade [245, 246] may become observable in gold nanorod dimer resonators due to their extremely small modal volumes. Furthermore, generation of higher harmonics has been predicted to occur in metal particle dimers featuring ultrasmall gaps [233], which could give rise to novel solid-state sources of attosecond laser pulses [247].

5 Electrically-connected resonant optical antennas

The interaction of low-frequency electric fields and optical-frequency photons forms the basis for a variety of technological milestones such as electrically-driven light sources, photovoltaic cells and devices for optical data processing and communication. For many applications the devices could benefit from the strongly localized and enhanced optical fields provided by plasmonic nanostructures. Increasing the interaction strength between photons and electric fields would not only allow to decrease the interaction volume and consequently the size of opto-electronic devices but could possibly lead to the observation of novel physical phenomena. Consequently, the interaction between electric fields/currents and enhanced optical near-fields has stimulated a variety of research within the young field of electro-plasmonics. Plasmons have been used to enhance the performance of light-emitting devices and solar-cells, electro-optical switching of plasmonic fields has been demonstrated and plasmons have been excited by electrons. A more detailed overview on the research field of electro-plasmonics is given in Chapter 2.3.1.

Notwithstanding the achievements of the mentioned experiments, so far little attention was paid to the design of the respective plasmonic structures and their enhanced and localized optical fields. A carefully designed structure could provide even more intense optical fields and lead to a further enhancement of the interaction between electrons and plasmons. Nano-antennas with small gaps show a particularly high field enhancement and localization. In this chapter the concept of electrically-connected resonant optical antennas is proposed and demonstrated. The key idea behind this study is that contacting a resonant antenna by metallic leads in nodes of the electric field is expected to hardly affect the antenna resonance. In Section 5.2 this is demonstrated by a numerical study. Using the obtained design principle, the fabrication of optimally connected antenna is shown in the next Section 5.3. Optical characterization, presented in Section 5.4, reveals pronounced and tunable antenna resonances. The influence of the choice of milling parameters on the electrical properties is shown in the Section 5.5. In particular, it is demonstrated that the antennas exhibit a very high electrical resistance and withstand applied voltages of at least 8 V corresponding to DC electric fields of 10^8 V/m in the gap. The results of this Chapter have been published in [248] and most of the text and graphics have been taken one-to-one from this publication.

5.1 Challenges and main idea

Electro-plasmonic devices are based on three essential ingredients. First, they exploit the enhanced optical near-fields provided by the plasmonic nanostructure. Second,

suitable electrical properties are required, that is an "active region" where large direct current (DC) electric fields occur, currents flow or charges recombine/separate. Finally, the electrically active and optically active region must spatially overlap.

A geometry that is natural to explore in this context is the two-wire gap antenna, as illustrated in Figure 5.1. The two-wire gap antenna provides a pronounced plasmonic resonances with strongly enhanced and localized optical fields in the gap region. The antenna arms may also be used as electrodes for (static) electric fields, leading to a capacitive coupling over the nanoscale gap. Consequently, an electrically-connected antenna automatically causes a self-alignment of the optically and electrically "active region". Therefore, electrically-connected antennas provide a versatile platform for a wide range of electro-plasmonic devices, where the functionality is determined by an additional material placed in the gap. For the concept to be applicable, the gap

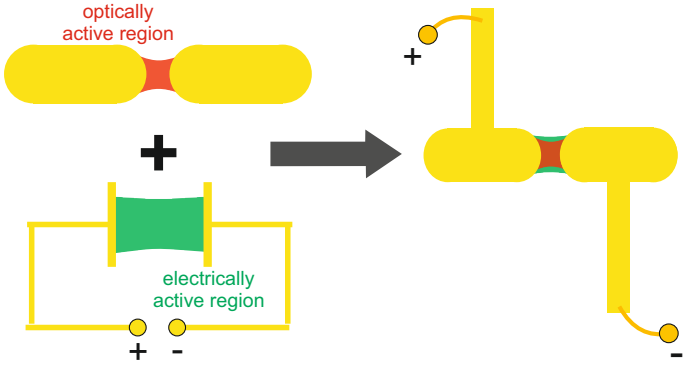

Figure 5.1: Concept of electrically-connected resonant optical antennas.

resistance is required to be high and other contact resistances to be low. If this is the case, then high potential differences can be built up over the gap, and prospective active materials that could be placed in the gap will dominate the electrical properties of the circuit. For the actual realization of such a structure, however, care must be taken when attaching an electrical connection to a nanoscopic antenna, since the antenna resonance is highly sensitive to its local environment [249, 250]. Consequently, it is important to study the influence of the electrical connection on the optical near-field distribution, resonance wavelength as well as resonance width.

5.2 Proof of concept via numerical simulations

Numerical simulations are performed with the aim of optimizing the position of the leads connecting the two antenna arms. The connecting lead is assumed to act as a perturbation of the unconnected antenna system. When an object with a small electric polarizability is placed near the antenna, the strength of the perturbation, in first approximation, scales with the square of the electric field at the objects position [251]. One may thus assume that, by attaching the leads to the antenna arms in the minimum of the electric field, their influence on the plasmon resonance is minimized. In order to verify this assumption the influence of the position of the leads on the

antenna resonance is investigated by numerical FDTD simulations (see Chapter 3.2.1 for details on this technique). Simulations are performed for 300 nm long, 50 nm wide, and 30 nm high gold antennas with a 20 nm gap on a transparent substrate (n=1.4). The antenna is illuminated from the substrate side with a tightly focused beam (NA=1.3) centered on the antenna gap.

To find the position along the antenna arms where the electric field intensity is minimal, the electric field intensity distribution is simulated in a cross section parallel to the bare antenna and perpendicular to the substrate. A plane at a 5 nm distance from the antenna is chosen as indicated in Figure 5.2a. It should be noted that the final results do not depend significantly on the choice of this distance. The normalized near-field intensity enhancement of the fundamental bonding-mode resonance at the cross section is shown in Figure 5.2b. High optical-frequency electric fields appear in the vicinity of regions in which surface charge is accumulated in response to the driving optical field, that is, the regions around the gap and the outer ends of the antenna. The integrated near-field intensity along the antenna cross-section is plotted as a function of the position in Figure 5.2c. From this plot one can obtain the field minimum, which occurs near the center of the arms at a distance of d = 71 nm.

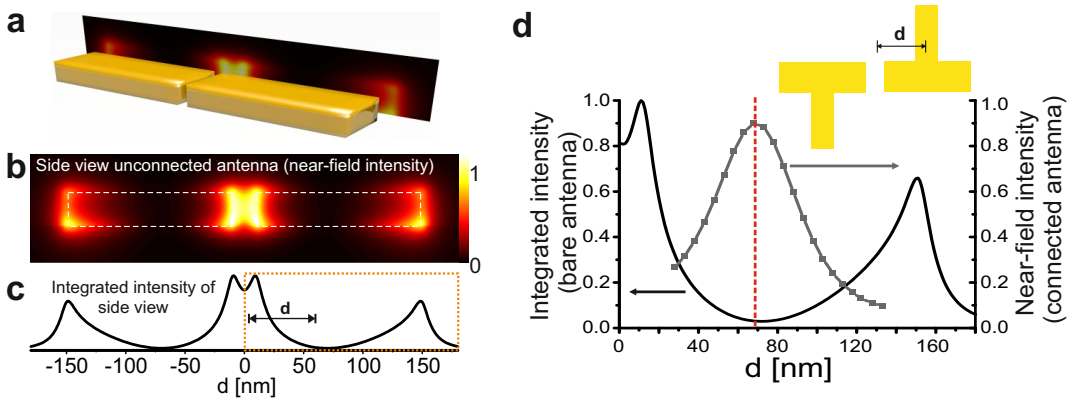

Figure 5.2: Near-field intensity of an isolated antenna. **a** Three-dimensional view of the antenna indicating the position of the cross section imaged in b. **b** The normalized near-field intensity map of the unconnected antenna in a cross section 5 nm from the surface of the antenna. **c** The normalized integrated electric field intensity of the cross section. Copyright (2012) American Chemical Society.

As a next step the role of the lead position is investigated by varying the connection point d of the 35 nm wide and 30 nm high gold leads, while preserving the point-symmetry of the structure (see inset in Figure 5.2d). The obtained resonant near-field intensities in the gap of the connected antenna are normalized to the enhancement of the bare antenna. In Figure 5.2d the result is compared to the integrated near-field intensity of the bare antenna (identical to the orange box in Figure 5.2c). The highest intensity enhancement is found for an optimal lead position of 68 nm (marked by the dashed red line). This is in excellent agreement with the position where the minimum of the near-field intensity is found for the bare antenna. It is important to note that the

connection point is robust against small deviations of the geometrical parameters of the connectors. For example, a connector position 10 nm from the optimum still shows a field enhancement which is only a factor 0.8 lower than the unconnected antenna.

The resonant character of connected antennas can be clearly observed in the near-field spectra recorded at the center of the gap, as displayed in Figure 5.3a. The spectrum of an unconnected antenna shows near-field intensity enhancements up to 1200 and a resonance with a quality factor of Q = 6. The optimally connected antenna (d=68 nm) exhibits a nearly unperturbed resonance with a near-field intensity enhancement of 1090 and a quality factor of Q=5.7. On the other hand, contacting the leads at the gap (d=17 nm) or at the antenna ends (d=132 nm) obviously leads to a dramatic decrease of the intensity enhancement and strong broadening of the resonance for the gap-connected and end-connected antenna (Q=2.7 and Q≈0, respectively). Since only moderate resonance shifts are introduced by the leads, it seems that the main effect of the leads at these positions is to damp the antenna resonance.

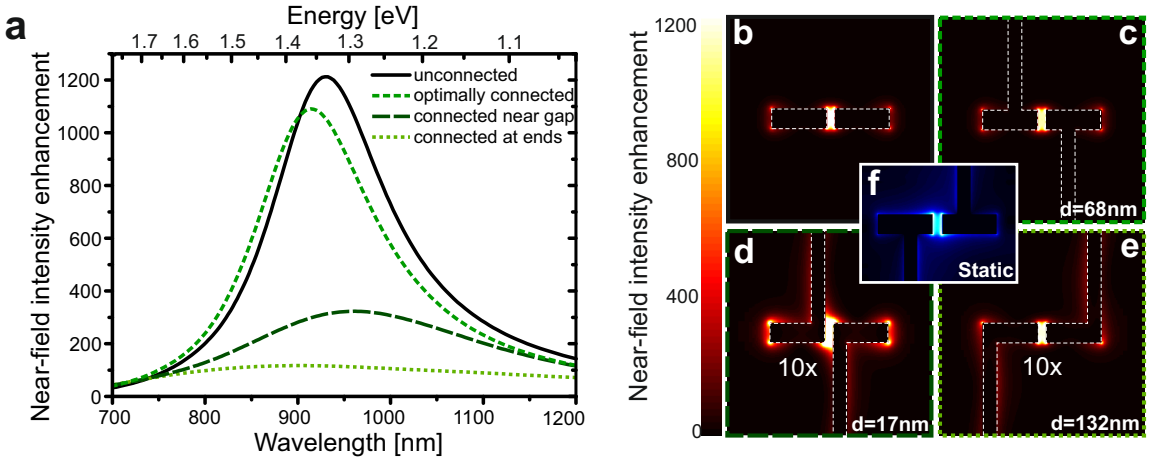

Figure 5.3: Near-field intensity of connected and isolated antennas. **a** Near-field intensity enhancement spectra in the center of the gap for the unconnected antenna (black, continuous), the optimally connected antenna (d=68 nm green, short-dash), gap connected (d=17 nm, dark green, long-dash), and end connected antenna (d=132 nm light green, dotted). **b-e** Resonant near-field intensity in a cross section 15 nm above the substrate: **b** Unconnected antenna, **c** optimally connected antenna (d=68 nm), **d** antenna connected at the gap (10-fold increased, d=17 nm), **e** end connected antenna (10-fold increased, d=132 nm). **f** Electrostatic field distribution of an optimally connected antenna. All antennas have a total length of 300 nm. Copyright (2012) American Chemical Society.

To gain insight into the nature of the perturbation and damping caused by the leads, Figure 5.3b-e show near-field intensity enhancement maps at the resonance frequencies of an unconnected antenna (b) and antennas connected at the gap (d) at the ends (e) and at the optimal contact point (c). All structures exhibit an intensity enhancement in the gap. However, in Figures 5.3d,e the near-field intensity enhancement is multi-

plied by a factor of 10, showing the adverse influence of leads connected to high-field regions. When comparing the near-field intensity maps, it can be seen that the field pattern of the optimally connected antenna is hardly perturbed. On the other hand, connecting the wire at the ends of the antenna or at the gap, leads to efficient launching of surface plasmons propagating along both leads (note the intensity along the leads in Figure 5.3d,e). It was found in simulations that the power flow over the leads is more than 10-fold higher in the case of a gap or end connected antenna compared to the optimally connected antenna. This additional loss channel likely explains the considerable broadening of the antenna resonance, as observed in the near-field spectra displayed in Figure 5.3a. However, the connection of the leads to high-field regions can no longer be considered as a small perturbation, and therefore a detailed treatment of the magnitude of this energy loss compared to the actual reduction of the quality factor is very complex and is beyond the scope of this thesis.

A co-localization of the region of intense optical field and high static electric field due to the voltage applied to the leads is expected to occur in the gap of connected antennas. To demonstrate this behavior, the static electric field for the optimally connected antenna was calculated using the relaxation method [252]. The antenna and leads were treated as perfect conductors, while for the glass substrate a dielectric constant of 3.7 was used. The influence of the outer boundary conditions was minimized by employing a large calculation volume. Figure 5.3f shows the static electric field distribution. The field strength in the gap is roughly the applied potential divided by the gap size. By comparing the simulated resonant field enhancement map (Figure 5.3c) and the electrostatic field map (Figure 5.3f), it can be seen that indeed both maps show a very good spatial overlap in the gap region. Consequently best conditions for electro-plasmonic interaction are provided.

5.3 Fabrication of electrically-connected antennas

Connecting the lead to roughly the center of the antenna arm has been found the optimal design for an electrically-connected antennas. To demonstrate the feasibility of this design, these structures are fabricated by focused ion beam (FIB) milling of single-crystalline gold flakes (see Chapter 3.1.3 and 3.1.4), which have been deposited onto glass cover slips. The use of single-crystalline gold for the fabrication of these structures might be critical for good device properties. The advantages arising from using single-crystalline gold are three-fold. First of all, FIB fabrication in single-crystalline gold provides better defined structures than for the case of multi-crystalline gold [73]. Second, resonant plasmonic structures with fewer grain boundaries have less ohmic damping leading to resonances with a narrower line width [253]. Finally, and probably most important in the present context, due to lack of grains the specific resistance of single-crystalline leads is largely independent of the wire cross section and therefore provides nanowire connections with good conductivity [222]. Moreover, a key advantage of the present approach is that, by using one material for both antenna and leads, the number of processing steps can be reduced, and problems due to contact resistance between different materials can be largely avoided [254]. Figure 5.4 shows scanning electron micrographs of four optimally connected antennas with different

antenna arm lengths and a gap width of 30 nm. These antennas are characterized by optical scattering experiments and will be color-coded according to the boxes around the antennas.

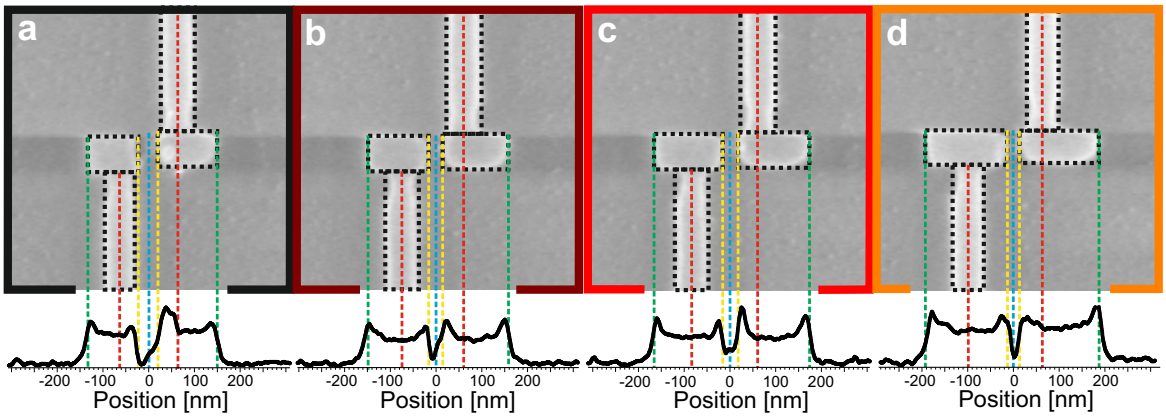

Figure 5.4: Fabrication of electrically-connected antennas. **a-d** Electron micrographs of the four optically characterized antennas. The bottom row shows respective intensity profiles through the center of the antenna. The colored lines are used to retrieve the dimensions of the antennas. Copyright (2012) American Chemical Society.

In order to retrieve the cross-sectional shape of the antennas the secondary electron intensity profiles of the electron micrographs are evaluated at the center of the antennas (bottom row of Fig. 5.4). It is observed that the cross-sectional shape is slightly trapezoidal, which leads to an uncertainty for the exact positioning of the rectangles of ±20 nm. The uncertainty for the determination of the leads' center is estimated to ±5 nm. The colored dashed lines mark the outer position of the antenna arms (green), the inner position of the antenna arms (yellow), the center of the antenna (blue) as well as the lead position (red). With these assumptions the respective lead positions, gap size and length of the individual antennas are retrieved:

	Antenna (a)	**Antenna (b)**	**Antenna (c)**	**Antenna (d)**
Lead position left	63 ± 5 nm	64 ± 5 nm	82 ± 5 nm	99 ± 5 nm
Lead position right	64 ± 5 nm	60 ± 5 nm	61 ± 5 nm	62 ± 5 nm
Gap size	44 ± 20 nm	30 ± 20 nm	32 ± 20 nm	26 ± 20 nm
Antenna length	283 ± 40 nm	309 ± 40 nm	340 ± 40 nm	380 ± 40 nm

It can be concluded that all four investigated structures have the leads attached near the optimal connection point considering the uncertainty in the measured dimensions as well as the rather broad minimum of the local near-field intensity enhancement.

5.4 Optical characterization

In the previous section it was demonstrated that electrically-connected antennas can be fabricated with the desired optimal design. Numerical simulations have shown that for this design the connected antennas are expected to provide a pronounced plasmon resonance despite the lead. In order to demonstrate this behavior experimentally scattering spectra were recorded using an asymmetric dark-field white-light scattering setup (see Chapter 3.2.2). The scattering spectra were normalized to the reference spectra of the halogen lamp, which was Fourier filtered to remove artifacts due to etaloning in the CCD camera. The scattering spectra are displayed together with the respective electron micrographs in Figure 5.5. The four characterized antennas have lengths of 280, 310, 340, and 380 nm, as determined from Figure 5.4. The scattering spectra show clear resonances and an increasing resonance wavelength for longer antennas as expected. From the Lorentzian fitting a quality factor of 4 has been obtained, which is in good agreement to the simulated value. The inset in Figure 5.5e shows the dark-field image of one of the antennas demonstrating that scattering occurs almost exclusively at the antenna. Scattering from the leads is very weak and does therefore not affect the measured scattering spectrum. These results clearly show that the fabricated connected antennas have excellent resonant optical properties.

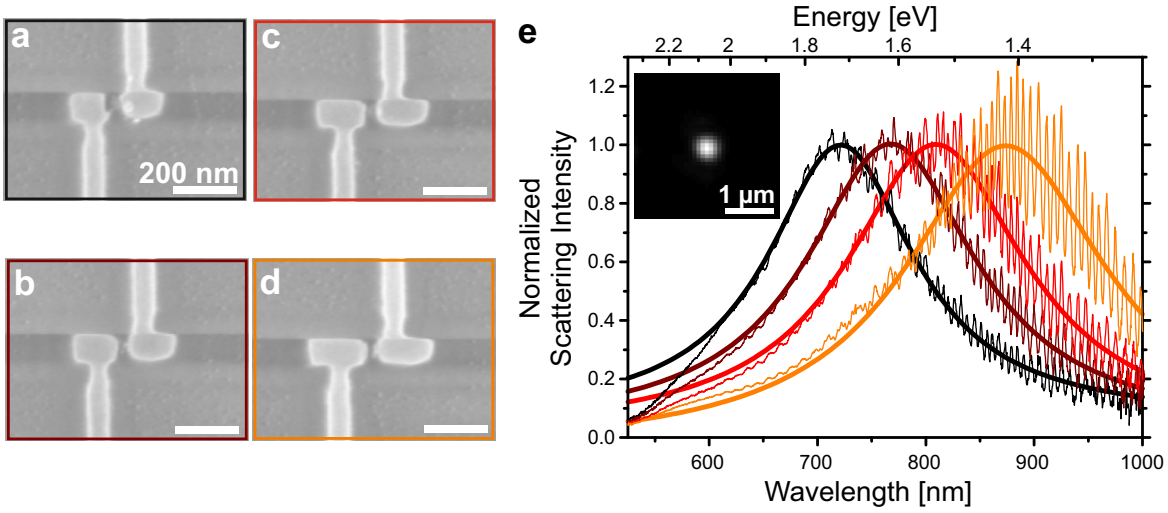

Figure 5.5: Optical characterization of connected antennas. **a-d** Electron micrographs of the four optically characterized antennas. **e** Dark-field scattering spectra of the four antennas shown in **a-d**, with a Lorentzian fit to the data. The black, dark red, red, and orange curves correspond to the scattering spectra of 280 nm, 310 nm, 340 nm, and 380 nm long antennas, respectively. The apparent oscillations for long wavelengths are due to etaloning in the CCD. The inset shows a typical dark-field image of a single connected antenna. Copyright (2012) American Chemical Society.

5.5 Electrical characterization

The electrically-connected antennas exhibit pronounced and tunable plasmon resonances. Future electro-plasmonic devices could exploit the intense optical and electrical fields in the antenna gap. In other applications an additional functional material could be placed in the gap of the antenna. For this reason it is important that the pristine antenna does not provide any parasitic electric conduction and low contact resistances are favorable. The electrical properties of the connected optical antennas were determined by measuring their current-voltage characteristics using a sourcemeter (SMU 2601A, Keithley, Cleveland, USA). The experiment was performed inside the vacuum of a scanning electron microscope (Ultra plus, Zeiss, Oberkochen) by contacting two macroscopic electrodes, which are in contact with the antenna arms, with copper beryllium (BeCu) probe needles attached to micromanipulators (MM3A-EM, Kleindiek Nanotechnik, Reutlingen). Further details of the electrical setup can be found in Chapter 3.2.3.

As a first step connected antennas without gap, i.e. a continuous gold wire, have been fabricated by ion-milling and their current-voltage characteristics were recorded. An electron micrograph of such a structure and a typical current-voltage characteristic is shown in Figure 5.6a. The maximum applied voltage was 0.5 V since for larger voltages electromigration [255] causes a movement of ions within the wire, which finally results in the formation of a gap. In the investigated voltage range a linear ohmic behavior is observed and the resistance has been determined to 250 Ω from a linear fit. This value is in good agreement to the expected value (255 Ω) of a 3.5 μm long gold wire with a quadratic cross-section of 55x55 nm^2, using a specific resistance of 0.02 $\mu\Omega$m. Similar structures fabricated from multi-crystalline gold show resistances of more than 1 kΩ. It can be concluded, that the single-crystalline gold exhibits superior electric properties and that the contact resistance between the BeCu probe needles

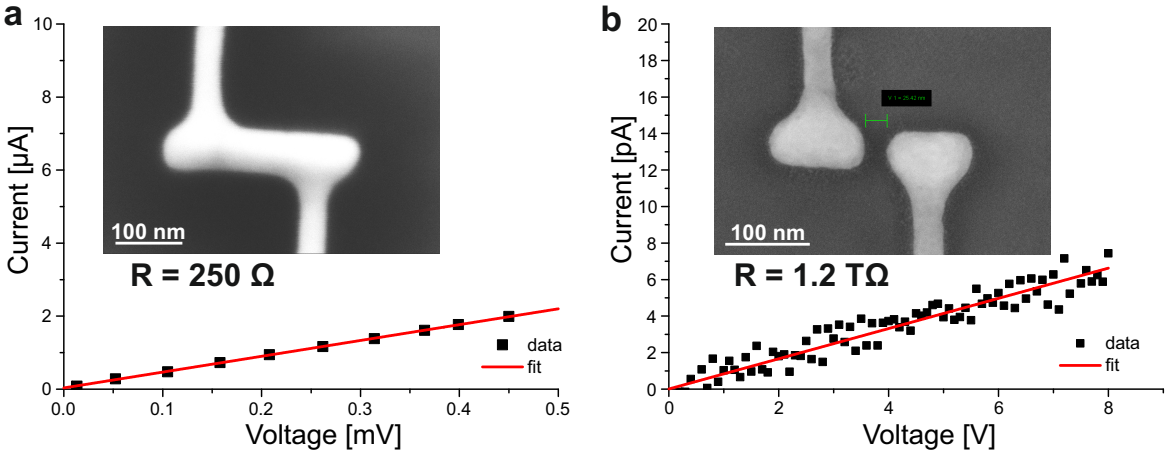

Figure 5.6: Electrical characterization of connected antennas. Current-voltage characteristic and electron micrograph of a connected antenna **a** without gap and **b** with gap. Resistances have been determined from a linear fit. Note the different x and y-scales.

and the single-crystalline gold is negligible.

Next, a typical current-voltage characteristic of a connected antenna with gap is investigated. The gap is about 25 nm wide and has been cut by focused-ion-beam milling. Figure 5.6b shows an electron micrograph and a typical current-voltage characteristic of such a structure. A linear ohmic characteristic is observed and the resistance has been determined to 1.2 TΩ. Consequently, these antennas exhibit superior electrical properties and are ideal elements of future electro-plasmonic devices.

Previous works using gallium-ion milling report ohmic resistances of 400 GΩ [256] and 80 GΩ [257] for nanogaps in gold wires on top of a titanium adhesion layer. Assisting the milling process by an iodine gas has lead to an increase in the resistance to about 50 TΩ [256]. Iodine is a gold etchant and it is likely that the observed increase in resistance is caused by the removal of small gold particles residing in the gap region after milling. In another work a sub-10 nm nanogap has been created by Argon etching [258]. In this study the authors report resistances larger than 500 TΩ, possibly by having avoided Gallium implantation as well as small gold particles.

Similar effects have been observed during the course of this thesis. In particular, it was found that the gap resistance strongly depends on the milling depth. If the gap is not milled deep enough, small gold particles can reside in the gap region. In this case a significant current can flow over the antenna arms. An electron micrograph of an exemplary structure and a zoom-in to the gap region is depicted in Figure 5.7a. For this structure the milling depth of the gap was set 5 nm smaller than the measured gold flake thickness. Remaining gold particles around the antenna arms can be clearly seen and it is likely that these particles also reside in the gap region. The electrical char-

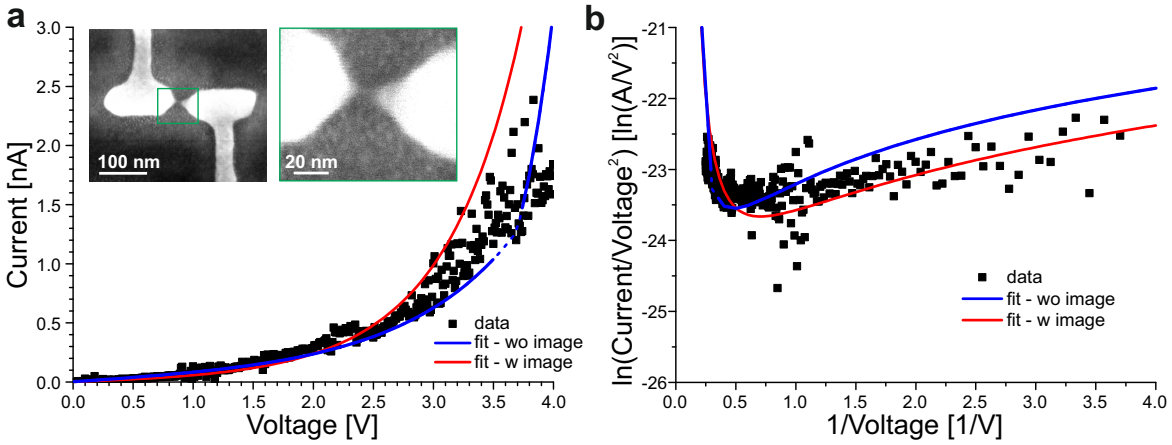

Figure 5.7: Current-voltage characteristic of a connected antenna with a shallow gap. **a** Current-voltage characteristic in a linear plot. Inset shows the electron micrograph of the antenna and a zoom-in to the gap region. **b** Current-voltage characteristic in a Fowler Plot. Solid lines are the respective fits of the tunnel current with (red) and without (blue) considering image charge effects.

acterization was performed under vacuum conditions, as described in the beginning of this chapter. The antenna shows a non-linear current-voltage characteristic (Figure

5.7a) and a change from positive to negative slope occurs in the Fowler-Nordheim representation (Figure 5.7b). A similar behavior would be expected for a tunnel junction, as discussed in Chapter 2.2.2. Therefore it is speculated that the gold particles form a conductive chain inside (or possibly even outside) of the gap region. The chain is disconnected at a certain point and consequently a tunneling junction is formed.

In order to test this hypothesis the tunneling current is modeled by equation 2.21 without the inclusion of image charge effects as well as with the inclusion of classical image charge effects according to equation 2.22. A non-linear fitting routine is performed via the commercial software OriginLab (Origin 8.5, OriginLabCorporation, Northhampton, USA) using a chi-square minimization algorithm (Levenberg Marquardt). The fitting algorithm is performed in the Fowler-Nordheim representation, i.e. $\ln[I/V^2]$ as a function of $1/V$. A reasonable agreement between the experimental data and the model is observed with and without the inclusion of image charge effects. For both models the tunneling cross-section was set to 1 nm^2 and a current offset of 2 pA as well as a leakage resistance of 1 TΩ have been assumed. The resulting tunnel gap widths are 0.73/0.9 nm and the barrier heights are 3.69/4.99 eV for the model with/without image charges, respectively. The recorded voltage range spans over the direct tunneling regime (applied voltage is smaller than the barrier height) as well as the Fowler-Nordheim regime (applied voltage is larger than the barrier height) for the model without image charges. Due to the mathematical treatment (see Chapter 2.2.2 for details) a discontinuity occurs at the transition and this region is plotted as a dashed curve in Figure 5.7a and b. Overall, the quality of the fit and the realistic values for gap size as well as barrier height indicate that a tunneling junction is formed. However, it is important to note that it is extremely difficult to reproducibly fabricate these types of tunneling junction. On the other hand, when milling the gaps sufficiently deep, electrical resistances on the order of 1 TΩ can be achieved in a controllable and reproducible manner. Consequently, these structures will be used for the electro-optical experiments in Chapter 6. There robust tunnel-junctions are created by positioning a single gold nanoparticle inside the gap.

5.6 Conclusion and Outlook

In conclusion, the experimental realization of an optical antenna structure that features electrical connections while preserving its resonant optical properties has been demonstrated. Numerical simulations showed that the position of the lead's connection point is critical. The optimal connection point is found to be the near-field intensity minimum of the fundamental bonding antenna mode. For this case the resonance properties are fully maintained. It is believed that this is a general concept, which can be applied to various other antenna geometries and resonances.

The feasibility of the present design has been demonstrated by fabricating optimally connected antennas of different length and the observation of respective shifts in their fundamental antenna resonance by dark-field spectroscopy. Current-voltage characteristics show a > 1 TΩ electrical resistance over the gap. The high resistance ensures that large potential differences can be maintained over the antenna gap. The proposed design enables electro-optical effects to be investigated in plasmon-enhanced

nanoscale devices and opens new avenues for realizing applications in quantum optics, nonlinear optics, optoelectronics, and photovoltaics. In particular, in the next chapter an electrically-driven sub-wavelength photon source is realized by using an electrically-connected resonant optical antenna.

6 Sub-wavelength photon source based on an electrically-driven nanoantenna

Nanoscale electrically-driven photon sources are an essential building block for future integrated opto-electronic devices and circuits. Micrometer-scale light-emitting devices have been realized by employing carbon nanotubes [259], semiconductor nanostructures [260, 261] and organic molecules [39, 262]. In these devices the emitting wavelength as well as the spectral bandwidth is limited by the internal electronic structure of the light-emitting material. Charge carrier injection and transport requires bulky electrodes or conductive matrices as well as sophisticated material compositions. Typically, control over the radiative properties is achieved by adding wavelength-scale structures such as out-coupling elements or dielectric resonators.

In this chapter a novel concept is demonstrated that integrates light generation and control into a planar single-material nanostructure. The investigated sub-wavelength photon source consists of an electrically-connected plasmonic nanoantenna (see Chapter 5) with an atomic-scale gap (see Chapter 4) as active element. Upon applying a DC voltage electrons tunnel inelastically across the antenna gap and generate far-field photons via the antenna resonance. A sketch of the geometry and the light emission process, including an energy diagram of one of the junction, is shown in Figure 6.1.

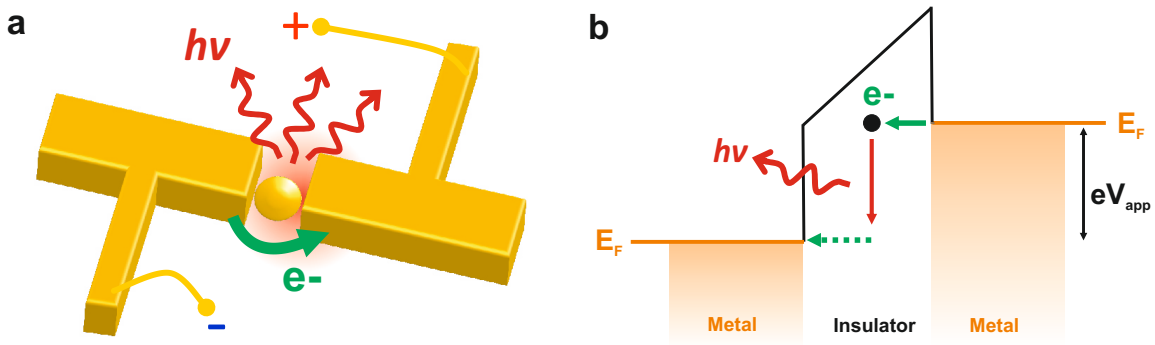

Figure 6.1: Electrically-driven sub-wavelength photon source based on a nanoantenna. **a** Artistic sketch of the investigated geometry. Electrons tunnel through the junctions formed between antenna arm and particle. The asymmetric position of the particle causes a voltage drop over only one junction. At this junction electrons that tunnel inelastically can couple to the antenna resonance leading to the generation of photons. **b** Energy diagram and schematic drawing of the light generation process via inelastic tunneling through the dominating tunnel junction.

Tunneling is a statistical process and the fluctuations in the tunneling current exhibit spectral components which can reach into the optical frequency regime. The broadband statistically-fluctuating current drives the antenna resonance, which then emits photons (see Chapter 2.3.2). The spectrum, directivity and polarization of the radiated photons are therefore dictated by the antenna geometry and the photon emission from inelastic tunneling is strongly enhanced with respect to a non-resonant system. The inelastic tunneling process has been studied before in MIM junctions and scanning tunneling microscopy. For an overview the reader is referred to Chapter 2.3.2.

Here, the planar geometry provides a voltage-independent gap, well-defined resonances, easy external access to the tunnel gap as well as potential for extending the antenna [71, 263] and electrode [264, 265] design. The presented work will push the development of electrically driven single- and multiphoton sources, opto-electronic nano circuitry for high speed data processing and on-chip multi-plexing, ultra-sensitive spectroscopy and sensing with nanometer resolution, DC-field induced nonlinear optics, as well as advanced display technology with ultra-high pixel densities. It furthermore establishes a strong link to the field of molecular electronics, as filling the nanoscale gap with functionalized organic molecules opens a variety of possibilities to tailor the electronic and optical properties of the junction.

The outline of this chapter is as follows. In the first section it will be shown how a (sub)-nanometer junction can be created by positioning a gold nanoparticle into the antenna gap with an atomic-force-microscope (AFM). The current-voltage characteristics presented in the second section prove the existence of tunneling gaps. The optical properties of the structure is investigated and the numerically simulated scattering spectra are in good agreement to the experiment. In the last section of the chapter the properties of the emitted light are analyzed and it will be shown that emission wavelength, polarization as well as directivity are dictated by the antenna resonance.

6.1 Fabrication of tunneling gaps via AFM-manipulation

For the fabrication top-down focused-ion beam structuring from single-crystalline gold flakes (Chapter 3.1.4) is combined with manipulation of functionalized gold nanoparticles into the antenna gap by means of an atomic-force microscope (Chapter 3.1.5). The gold particles are surrounded by a molecular layer (Chapter 3.1.2). In Chapter 4 it has been demonstrated that this layer acts as a stabilizing spacer leading to well-defined atomic-scale gaps. Here, this fact is exploited for the creation of tunneling-junctions. A main advantage of this method is that the antenna as well as the functional particle are single-crystalline gold. The single-crystal character ensures a high degree of reproducibility and at the same time electrical and optical properties may benefit.

The starting point for the fabrication are optical antennas, which are electrically connected to a suitable electrode structure (see Chapter 5.3). The gap width of the antenna has been fabricated to 28-32 nm to precisely match the gold spheres. Gold nanospheres with a diameter of 30 nm are drop-casted onto the sample leading to a

random distribution of spherical particles around the antenna (see Chapter 3.1.2 for details). Prior to manipulation, particles located within 5 μm from the antenna are identified with an SEM to avoid time-consuming AFM scans. Details of the manipulation procedure have been presented in Chapter 3.1.5 and here only the main steps are repeated. Within the first step a single particle is brought within 500 nm distance from the antenna. The initial distance determines the number of movements which are necessary, since it is difficult to move the particle more than 1 μm at once. Figure 6.2a shows the antenna and the gold particle before and after this step. The second step moves the particle into its final position as shown in Figure 6.2b. This step is much more critical and the final movements are only several tens of nanometers to avoid a false positioning. Typically more than 10 movements are required for this step. It should be noted that in some cases the particle seems to jump to the antenna gap, arm or even on top of the antenna. Once the particle is attached it is difficult to alter its position. Even though the manipulation can be time-consuming and may not be successful for every structure, antennas with tunneling junctions can be reproducibly fabricated. It is difficult to judge the exact position of the nanoparticle from an AFM

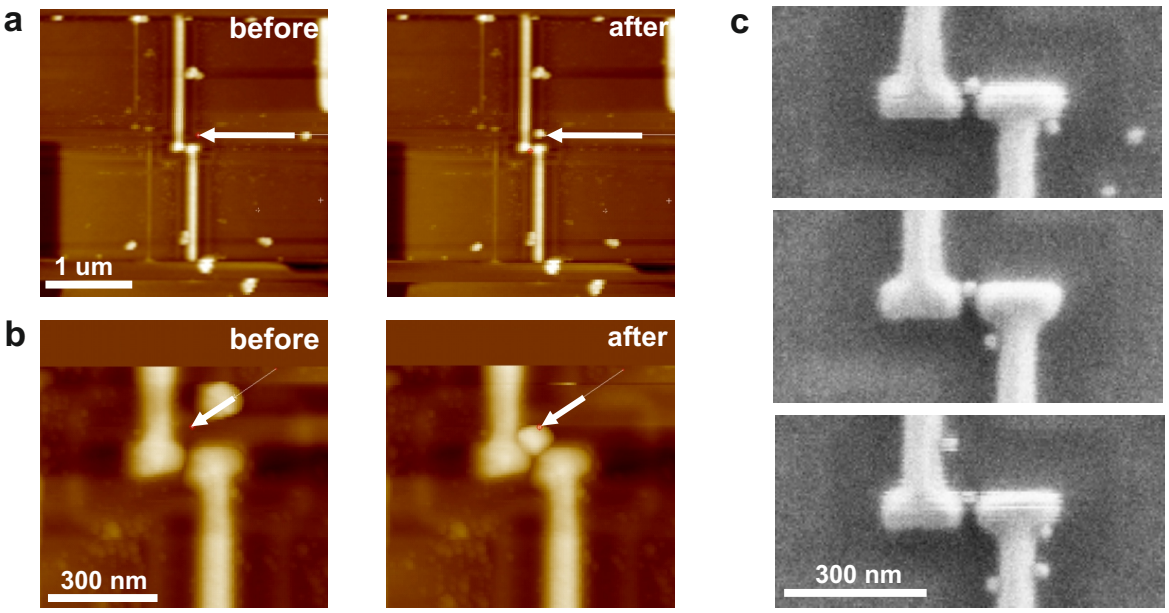

Figure 6.2: Creation of tunnel junctions by loading antennas with nanoparticles. **a** The first step of the manipulation procedure brings a spherical gold particle close to the antenna. **b** Within the second step the particle is brought into its final position inside the antenna gap. Left/right AFM images show the situation before/after manipulation, respectively. The white arrow indicates the specified movement of the AFM tip. **c** Electron micrographs of three different antennas with a nanoparticle in the gap.

image, since an AFM image is a convolution of the AFM tip and the sample. For this reason the final results are investigated in an SEM to resolve the position of the particle. Typical electron micrographs of fabricated structures are shown in Figure 6.2c.

The exact gap size cannot be determined due to the resolution of the SEM and only an upper limit of a few nanometers can be given for the gap size.

In order to prove that a tunneling junction has been created the electrical properties of the structures are investigated and the results are presented in the next chapter.

6.2 Electrical properties of nanoantennas with tunneling gaps

In the previous chapter it was shown that small gaps can be created by positioning a particle in the gap of an antenna. In this chapter the current-voltage characteristics of these gaps are investigated and it is demonstrated that a tunnel junction exists between antenna arm and particle.

The current-voltage characteristics are obtained under ambient conditions and details of the experimental setup are described in Chapter 3.2.3. A non-linear dependence of the current on the voltage is observed (Figure 6.3a). The Fowler-Nordheim representation of the data is presented in Figure 6.3b. A transition from a positive slope to a negative slope is observed, as expected for electron tunneling (see Chapter 2.2.2). Before analyzing the current-voltage characteristics it is important to recall that the structure consist of two tunnel-junctions (one on each side of the particle) in series. The voltage drop at either gap therefore depends on the respective junction resistance. However, the tunneling resistance depends exponentially on the gap size and it is assumed that the two gaps have a slightly different size. The applied voltage will drop mainly over the larger gap which therefore dominates the current-voltage characteristic. Experimentally this is justified by observing the predicted shift of the quantum cutoff with applied voltage (Chapter 6.4). Consequently, the system is modeled as a single-junction and the current-voltage characteristic (equation 2.21) presented in Chapter 2.2.2 is applicable. A non-linear fitting routine is performed via the commercial software OriginLab (Origin 8.5, OriginLab Corporation, Northampton, USA) using a chi-square minimization algorithm. Due to the exponential dependence of current on voltage the fitting is performed in the Fowler-Nordheim representation. A current offset of 2 pA as well as leakage resistance of 1 TΩ has been considered and the tunneling cross-section has been fixed to 1x1 nm^2. The two open parameters are the gap size s as well as the barrier height φ_0. As discussed in Chapter 2.2.2, image charge effects have a strong influence on the current-voltage characteristic. For this reason the experimental data has been fitted with (solid gray line) and without (dashed blue lines) the inclusion of image charges. In the Fowler-Nordheim representation as well as on a linear scale the fit agrees well with the experimental data (black rectangles) when image charge effects are included. Without the inclusion of image charge effects reasonable fits can be obtained either in the low voltage regime (dark blue line) or in the high voltage regime (light blue line). However, it is not possible to get a good agreement to the experimental data over the full voltage range. The recorded voltage range spans over the direct tunneling regime (applied voltage is smaller than the barrier height) as well as the Fowler-Nordheim regime (applied voltage is larger than the barrier height). Due to the mathematical treatment (see Chapter 2.2.2 for details) a

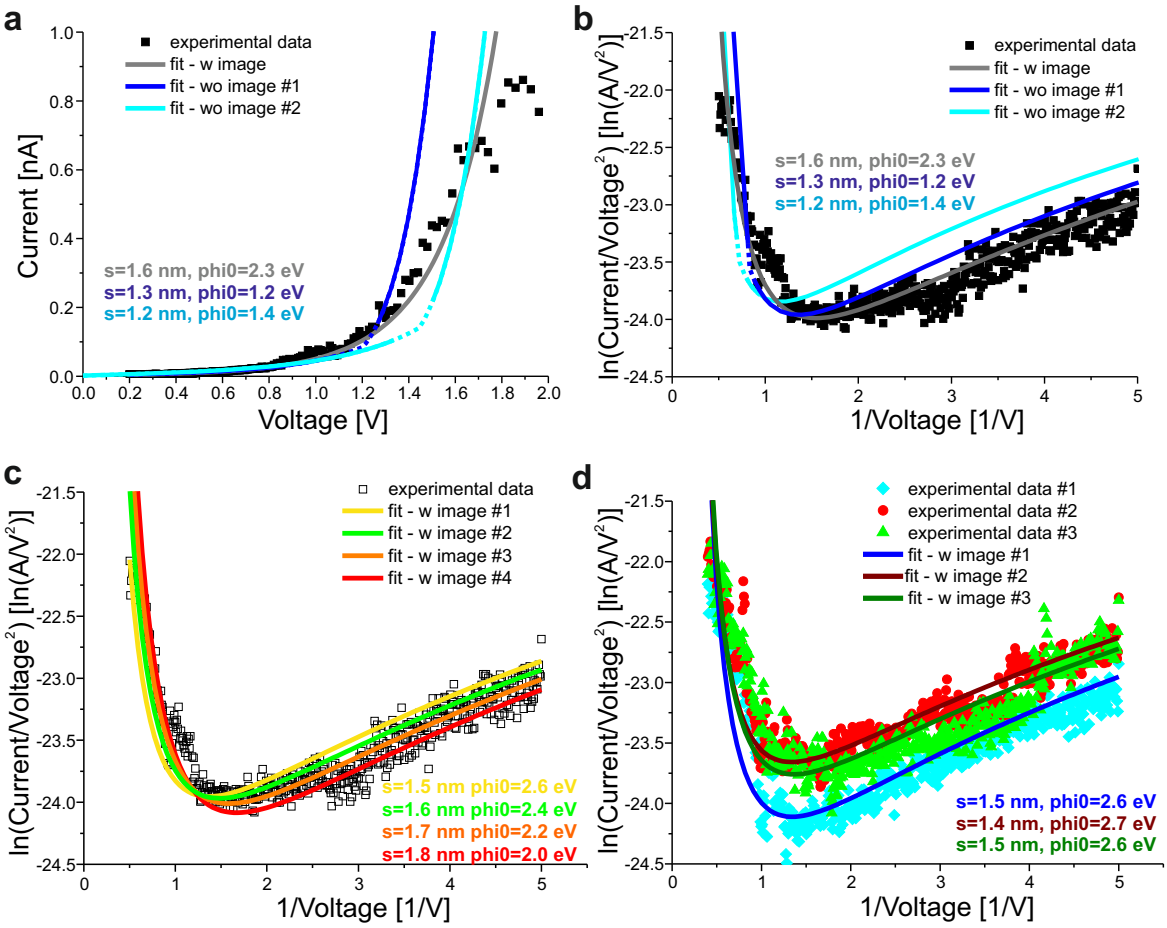

Figure 6.3: Electrical properties of nanoantennas with tunneling gaps. **a** Experimental current-voltage characteristic on a linear scale. Solid lines are non-linear fits to the data with (gray) and without (blue) the inclusion of image charge effects. **b** Fowler-Nordheim representation of the data in **a**. **c** Fitting the same current-voltage characteristic with different fixed gap sizes. **d** Three subsequently recorded current-voltage characteristics of the same structure with corresponding fits.

discontinuity occurs at the transition and this region is plotted as a dashed curve in Figure 6.3a and b.

With the inclusion of image charges a value of 1.6 nm is obtained for the gap size, which is in good agreement to the value estimated from the electron microscopy image of the measured structure. For the barrier height a value of 2.3 eV is obtained. As discussed in Chapter 2.2.1, the barrier height is strongly affected by surfaces states or adsorbents at the interface, such as organic molecules or water. Since the measurements have been conducted at ambient conditions a value of 2.3 eV for the barrier height is reasonable and similar values have been reported in the literature [115–117].

To estimate the uncertainties of gap size and barrier height the fitting procedure has been repeated for 4 different fixed gap sizes (1.5-1.8 nm) leaving the barrier height

as the only open parameters. The results are shown in Figure 6.3c and reasonable fits are obtained for a gap size of 1.6 nm and a barrier height of 2.4 eV, as well as for a gap size of 1.7 nm and a barrier height of 2.2 eV. For a gap size of 1.5 nm and 1.8 nm deviations between the experimental data and the fit are clearly visible. Consequently, for this structure the resulting uncertainty is about 0.2 nm for the gap size and 0.2 eV for the barrier height. It should be noted that an additional error is introduced by assuming a simple model for a single planar junction, however it is difficult to estimate the magnitude of this error.

In order to test the stability of the investigated system three additional current-voltage characteristics have been measured for the same structure and the obtained data as well as corresponding fits are presented in Figure 6.3d. For the first measurement (blue rhombus) a gap size of 1.5 nm and a barrier height of 2.6 eV is obtained. The values from the second measurements (red circles) are 1.4 nm and 2.7 eV for gap size and barrier height respectively. The third measurement (green triangles) yields a gap size of 1.5 nm and a barrier height of 2.6 eV. These differences are within the above determined uncertainty and it can be concluded that the structure exhibits a stable tunneling junction.

It should be noted that for different antennas the obtained gap sizes and barrier heights vary since the position and size of the nanoparticle is slightly different for each structure. For all structures the obtained gap size lies within 0.8 to 2 nm and the barrier heights range from 1.2 to 2.8 eV. In some cases the current-voltage characteristic was unstable in the beginning or has changed after several voltage sweeps. However, all data presented in this chapter were recorded for structures which were stable during the measurements (see also Figure 6.8).

6.3 Optical properties of nanoantennas loaded with a nanoparticle

In the previous chapter it has been demonstrated that a tunnel junction is formed between the gold particle and the antenna arm. Optical antennas are sensitive to their environment and it is expected that the particle which is situated in a high-field region significantly alters the optical properties with respect to the isolated antenna. To investigate these effects numerical FDTD simulations are performed. The antenna is modeled as two rectangular particles with a width of 80 nm, a height of 50 nm and an arm length of 120 nm. The choice of approximating the antenna arms by rectangles is justified since scattering spectra are not sensitive to the exact shape [266]. The antenna is situated on top of a SiO_2 (n=1.455) half-space. The dielectric constant of gold is modeled by an analytical fit to experimental data [217]. A spherical particle with a diameter of 28 nm is placed in the 30 nm large gap between the antenna arms. The effect of the position of the particle is investigated. A refinement mesh of 0.25 nm is placed over of the gap region. The structure is excited by a total-field scattered-field source and the scattering intensity is obtained by calculating the power-flow into the substrate direction. Further details on the simulation technique can be found in Chapter 3.2.1. The simulated scattering spectra are shown together with a sketch of

the respective geometry in Figure 6.4a. The diameter of the particle is denoted d and the position of the particle from the antenna gap is z. The spectra are normalized, but all scattering intensities are of the same order of magnitude.

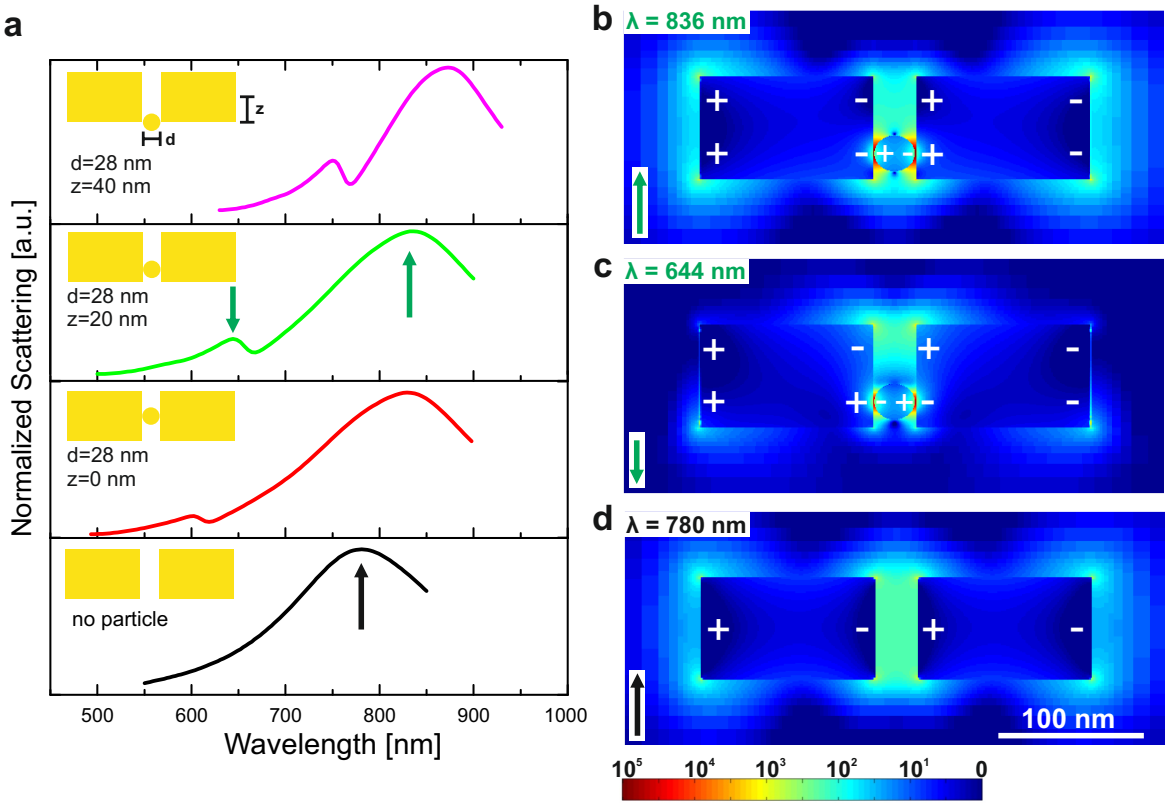

Figure 6.4: Influence of nanoparticle on optical properties. **a** Scattering spectra obtained from FDTD simulations for different gold particle positions. **b-d** Near-field intensity distributions in logarithmic color scale. **b** Antenna with particle in the gap. Resonance at 836 nm, as indicated by the green upward-pointing arrow in a. **c** Antenna with particle in the gap. Resonance at 644 nm, as indicated by the green downward-pointing arrow in a. **c** Antenna without particle.

The antenna without particle shows a single resonance at 780 nm (black line in Figure 6.4a). The corresponding near-field intensity enhancement of the dipolar mode is about 500 and the intensity is concentrated between the antenna arms (Figure 6.4d). When the particle is placed into the antenna gap two peaks are observed which depend on the position of the particle. If the particle is in the center of the gap, the peak positions are 820 and 600 nm (red line in Figure 6.4a). For the case where the particle is 20 nm out of the center the peak positions are at 644 nm and 836 nm (green line in Figure 6.4a). A further displacement of the particle from the center leads to a further shift of the peaks, which are then situated at 750 and 870 nm. Similar results have been obtained for gold loaded disk antennas [267].

To investigate the physical origin of the respective peaks the near-field intensity

distributions have been calculated for a position of the particle 20 nm from the center. For the lower energy mode at a wavelength of 836 nm (Figure 6.4b) the charge distribution is very similar to the isolated antenna. The particle in the center is in phase with the antenna arms and high-field regions occur between the particle and both antenna arms. The intensity enhancement in this region is about $2{\cdot}10^5$, which is more than two orders of magnitude larger than for the antenna without particle. The resonance wavelength of the lower energy mode is shifted to larger wavelength with respect to the isolated antenna and its peak position strongly depends on the antenna length. Moreover, the peak position depends on the size of the particle and larger resonance wavelengths are observed for larger particles. Consequently, the particle seems to act as a polarizable material, which increases the surface charge accumulation at the gap.

For the higher energy mode at a wavelength of 644 nm (Figure 6.4c) the particle oscillates out of phase with respect to the charges at the outer side of the antenna arms. The charges at the inner side of the antenna, i.e. the gap region, are of opposite sign at the position of the particle compared to the position without particle. Consequently, a field minimum occurs at the very center of the antenna. The near-field intensity enhancement at the position between the polarized particle and both antenna arms is about $5{\cdot}10^4$. The higher-energy mode strongly depends on the position of the particle as well as the width of the antenna. However, its peak position is only slightly affected by the length of the antenna.

As a next step the experimental scattering spectra are analyzed and compared to the numerical results. To this end the spectra of a single nanoantenna are recorded before and after positioning of the particle. The electron micrograph of the antenna with particle is shown in Figure 6.5a. The obtained structural dimensions are a gap size of 28±2 nm, a particle size of 26±2 nm and an offset from the center of 15±2 nm. The error is given by the pixel size of the micrograph.

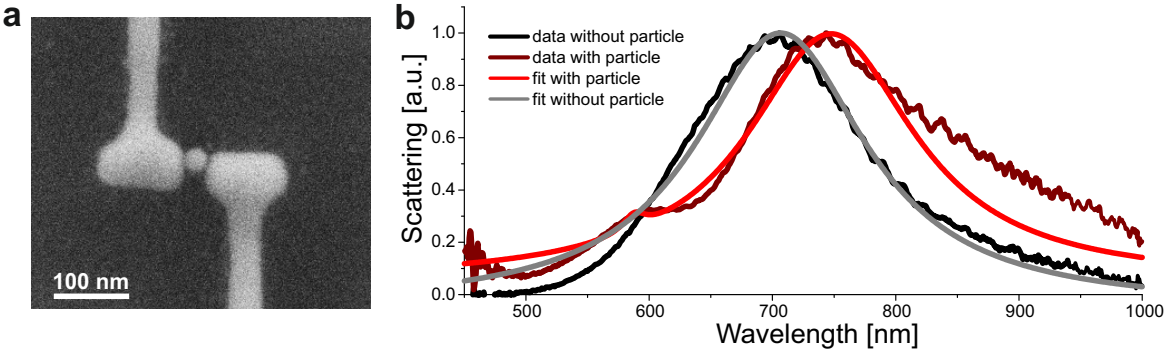

Figure 6.5: Influence of nanoparticle on optical properties. **a** Electron micrograph of the antenna with the positioned nanoparticle. **b** Experimental scattering spectra without (black) and with (brown) the positioned nanoparticle. The solid grey line is a Lorentzian fit. The solid red line is a fit consisting of two Lorentzians.

In Figure 6.5b the white-light scattering spectra are presented together with the

corresponding Lorentzian fits for the antenna without (black/gray line) and with (brown/red line) the particle in the gap. The pristine antenna shows a single resonance at a wavelength of 703 nm. For the antenna with particle in gap two resonances are observed at a wavelength of 595 and 747 nm. The observation of two resonances as well as their spectral position relative to the pristine antenna are in good agreement to the numerical simulations for the 28 nm particle at a position 20 nm from the center.

6.4 Nanoantenna-based photon source

In the previous sections the optical and electrical properties of the tunnel junction between particle and electrically-connected nanoantennas were analyzed. This section investigates the antenna enhanced photon generation via inelastic tunneling. The electroluminescence spectrum, polarization and radiation patterns of the sub-wavelength photon source will be analyzed.

Electroluminescence and its dependence on voltage

Applying a voltage to the antenna arms causes electrons to tunnel over the (sub)-nanometer gap. A certain amount of electrons tunnel inelastically and far-field photons are generated by the antenna. In order to study the light emission process the tunneling current as well as the radiated photons are recorded simultaneously. The emitted photons are dispersed onto an EM-CCD camera via a grating (80 lines/mm). Typical integration times of the electroluminescence spectra are on the order of 500 ms. All spectra have been corrected for the wavelength-dependent detection efficiency of the optical setup.

In a first experiment the applied voltage has been increased in steps of 0.1 V. In Figure 6.6a the tunneling current is plotted together with the amount of emitted photons as a function of voltage. The current-voltage characteristic shows a non-linear relationship as expected for a tunneling junction. The gray line shows a fit to the data from which a gap size of 0.9 nm and a barrier height of 1.3 eV have been obtained. The number of photons is calculated considering the collection efficiency of the setup including the sensitivity of the EM-CCD camera. The first photon signal is observed at a voltage of 1.6 V and after that the number of photons increase non-linearly with voltage. An almost linear relationship is observed between photon and current signal. The current has been limited to 200 nA by the sourcemeter, in order to avoid destruction of the sample.

The electroluminescence spectra for voltages from 1.7 to 2.0 V are presented in Figure 6.6b. These voltages are larger than the barrier height and consequently electrons tunnel through a reduced barrier, i.e. the Fowler-Nordheim tunneling regime. In the electroluminescence spectra a clear peak is observed, which shifts to lower wavelengths with increasing voltage.

The spectral dependence of the electroluminescence can be understood by assuming that fluctuations in the tunneling current couple to the antenna resonance. As discussed in Chapter 2.3.2 the magnitude of the frequency-dependent fluctuations shows a voltage dependence of $C(\omega) = eV\left(1 - \frac{\hbar\omega}{eV}\right)$. These fluctuations can be seen as a con-

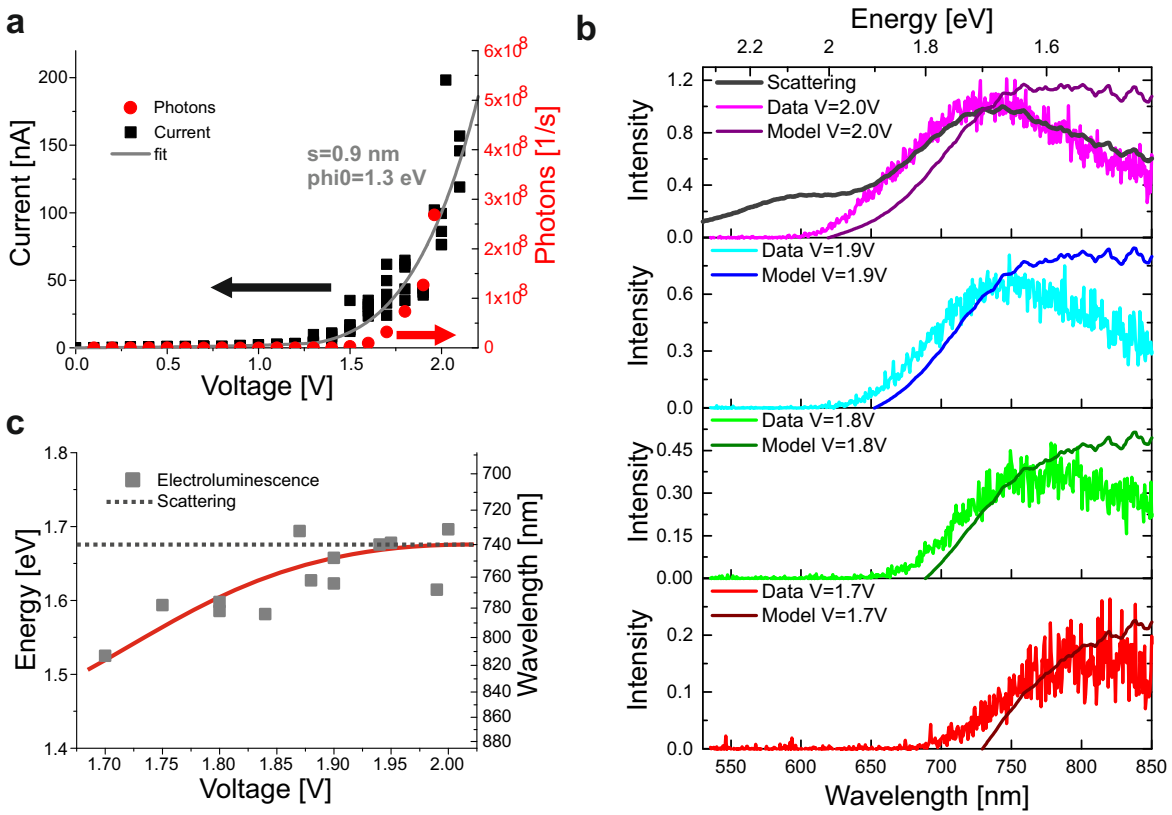

Figure 6.6: Electroluminescence (EL) as a function of voltage. **a** Current (black squares) and number of photons (red circles) recorded simultaneously as a function of applied voltage. The solid gray line is a non-linear fit of the current-voltage characteristic. **b** Experimental EL spectra for an applied voltage of 1.7, 1.8, 1.9 and 2.0 V as well as modeled spectra. In the top row the scattering spectra of the same structure is shown for comparison. **c** Peak position of the electroluminescence (gray squares) as a function of voltage. The peak position of the scattering spectra is plotted as a dashed gray line. The solid red line serves as a guide to the eye.

tinuous distribution of single-frequency dipole sources which reside within the tunnel gap. The light generation is a two-step process. In a first step the dipole excites the antenna in its near-field and the excitation efficiency depends on the near-field response of the antenna resonance. In the second step the antenna radiates into the far-field and the radiation spectrum is given by the far-field response of the antenna. The investigated single-crystalline antennas exhibit relatively narrow resonances and it has been shown that under such circumstances near- and far-field response are almost identical [268]. As a consequence the spectral response of the electroluminescence can, within a first approximation, be described by a multiplication of the frequency-dependent dipole source $C(\omega)$ with the scattering spectrum of the antenna.

The scattering spectrum as well as a comparison between model and experiment is shown in Figure 6.6. Good agreement is observed between experiment and model.

Most importantly, the shift of the spectrum with increasing voltage is predicted. For a linear process the energy of the emitted photons cannot be larger than the applied potential energy (quantum cutoff), a fact that is also observed in the experiment. The quantum cutoff in the electroluminescence spectra is observed at the position of the applied voltage, which confirms that the light generation is dominated by a single junction.

For voltages larger than 1.9 eV the electroluminescence spectrum resembles the scattering spectrum and does not shift further. This fact is clearly observed in Figure 6.6c, where the peak position of the electroluminescence approaches the scattering peak for increasing voltage. Once the voltage is large enough no further shift is observed and the spectrum only increases in intensity. A direct comparison between scattering and electroluminescence is shown in the top row of Figure 6.6b. It can be clearly seen that the electroluminescence spectrum is almost identical to the scattering spectrum from 900 to 650 nm wavelength. At 650 nm a second peak is observed in the scattering spectrum, as discussed in Chapter 6.3. For this higher-energy mode the near-field intensity enhancement as well as the radiation efficiency is lower than for the lower-energy mode. Consequently, the light generation efficiency is significantly lower and the higher-energy peak cannot be detected above the noise of the measurement. On the other hand the dipolar antenna mode at a wavelength of 740 nm exhibits good radiative properties and the fact that the electroluminescence spectrum is dictated by this resonance shows the enhancement of the photon generation process by the antenna.

Angular distribution and spatial dimensions

As a next step it will be shown that the angular distribution of the radiated light is determined by the antenna. To this end an additional convex lens (focal length 1000 mm) has been placed in order to image the back-focal plane of the microscope objective (Plan-Apochromat 63x, 1.4NA, Zeiss, Jena). The integration time was 10 s. A schematic drawing of the experimental configuration is shown in Figure 6.7a. The emission pattern is recorded below the substrate. The experimentally obtained emission pattern is presented in Figure 6.7b. For comparison a numerically calculated emission pattern of a loaded nanoantenna is shown in Figure 6.7c. Good agreement is obtained between experimental and numerical result. Moreover, the polarization of the emitted light was investigated. A 10:1 polarization ratio was found along the antenna axis, limited by the depolarization of the 1.4NA objective. Consequently, it can be concluded that the directivity as well as the polarization of the radiated light is dictated by the nanoantenna.

In order to proof that the detected photons are originating from a sub-wavelength source the emission spot has been imaged with the EM-CCD camera. Figure 6.7d shows the result and is overlayed with an electron micrograph of the antenna. In order to allow for a precise overlay the structure has been illuminated by a low-intensity white-light source. An Airy pattern is expected for a diffraction limited spot and Airy rings are clearly observed. From the vertical cross-section in Figure 6.7d a full-width-half-maximum (FWHM) of 350 nm is obtained. The expected FWHM in the lateral direction from a fluorescent point object is given by FWHM$=0.51\cdot\lambda/$NA [269].

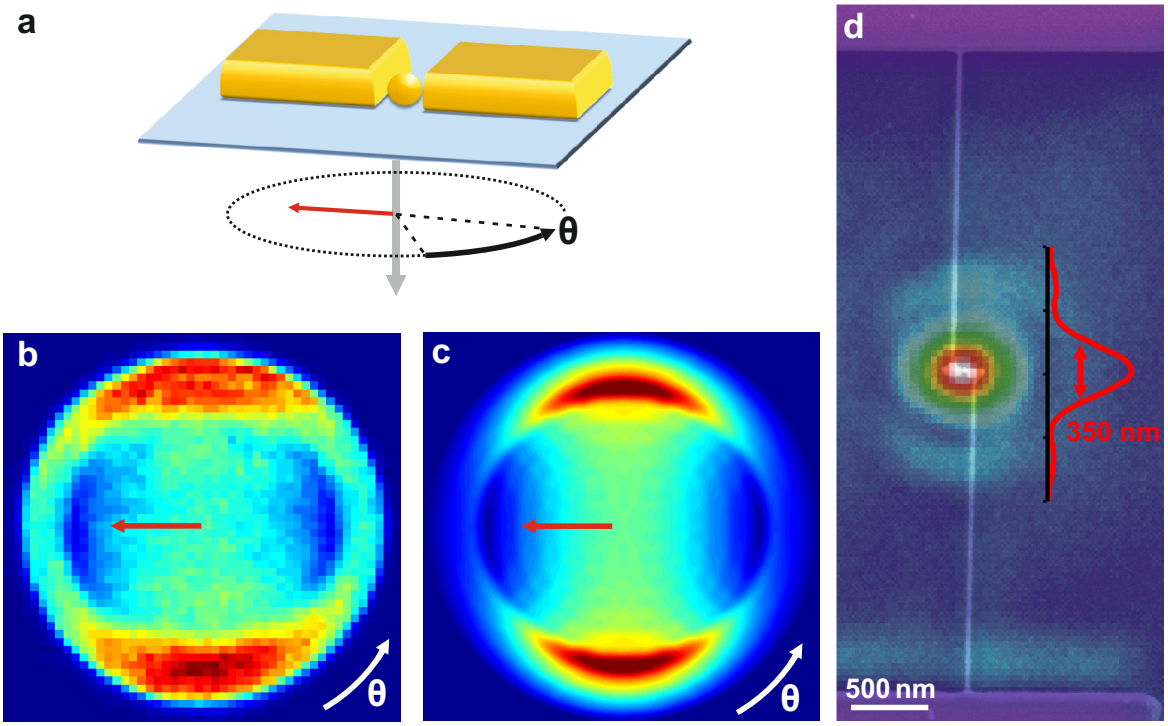

Figure 6.7: Emission pattern and spatial dimensions of the nanoantenna-based photon source. **a** Schematic drawing of the experimental configuration. Electroluminescence is emitted in direction of the glass substrate. **b** Experimental emission pattern of the electroluminescence emitted by the nanoantenna-based photon source. **c** Simulated emission pattern of a loaded nanoantenna. Red arrows in **a-c** mark the antenna long axis. Azimuthal angle is denoted θ. **d** Overlay of EL image and electron micrograph of the emitting antenna. Inset shows a vertical cross-section through the center of the emission spot.

For the investigated nanoantenna-based photon source the emitted central wavelength was 900 nm and an objective with an NA of 1.4 was used. A FWHM of 328 nm is expected, which is in good agreement to the experiment. It can be concluded that the electrically-driven nanoantenna is a sub-wavelength photon source.

Stability of the tunneling junction

The tunneling current is very sensitive to the width of the junction. Movements of the particle within the gap or changes of the atomic configuration of the gap, e.g. by surface diffusion [270] are expected to affect the tunneling current as well as the electroluminescence signal. Since all measurements are conducted at room temperature and ambient conditions, it is important to investigate the stability of the tunneling junction. To this end, a voltage of 1.8 V corresponding to a field strength on the order of 1^9 V/m was applied to the junction while the tunneling current is recorded simultaneously with the electroluminescence spectrum. By integration over the spectrum the

total amount of emitted photons can be obtained. In Figure 6.8a the tunneling current is plotted together with the number of radiated photons as a function of time. During the recorded 30 seconds the tunneling current increases slightly and does show some fluctuation. The emitted photons follow this trend. The electroluminescence spectrum during the same time interval is shown in Figure 6.8b. The shape of the spectrum is very stable and no significant shifts in wavelengths are observed. Considering the

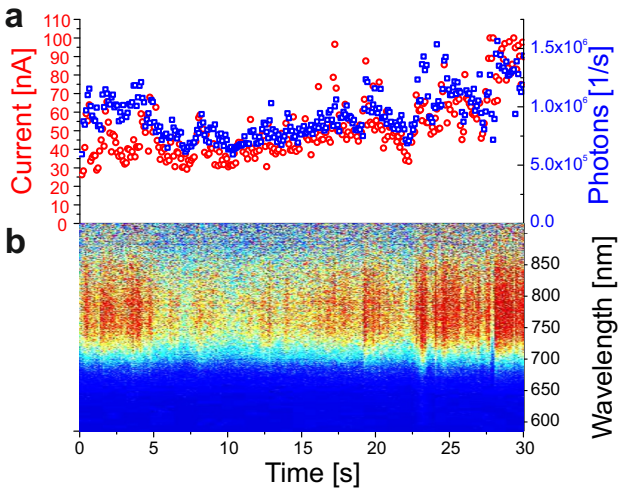

Figure 6.8: Time and spectral stability. **a** Tunneling current and number of emitted photons recorded simultaneously over 30 seconds. **b** Spectrum of the electroluminescence during the same 30 seconds.

fact that the experiments are performed at room temperature, the tunneling junction shows an astonishing good stability. The good stability can be likely attributed to the molecular spacer layer around the spherical particle, which is electro-statically bound to the antenna. Even more stable junctions could be realized by exploiting molecules which covalently bind to the gold surface or by embedding the tunneling junction into an insulating material.

Tunability of the emission spectrum and comparison to a non-resonant structure

In the last part of this chapter the tunability of the emission spectrum by the antenna geometry is investigated. Moreover, a non-resonant wire of micrometer-length is investigated for comparison and the efficiency of the light generation process is discussed. The electron micrographs of the respective structures are shown in Figure 6.9a-d. The scattering as well as the electroluminescence spectrum are shown in the same row as the micrographs. All spectra have been normalized to 1 for better visibility. Typical integration times for the electroluminescence spectra are 100 ms for the antenna structures and 1 s for the non-resonant wire. For all structures a very good agreement is observed between scattering and electroluminescence. The antennas are of similar length and the peak position is mainly determined by the position and size of the particle in the gap. A clear shift of the resonance is observed and the peak positions are

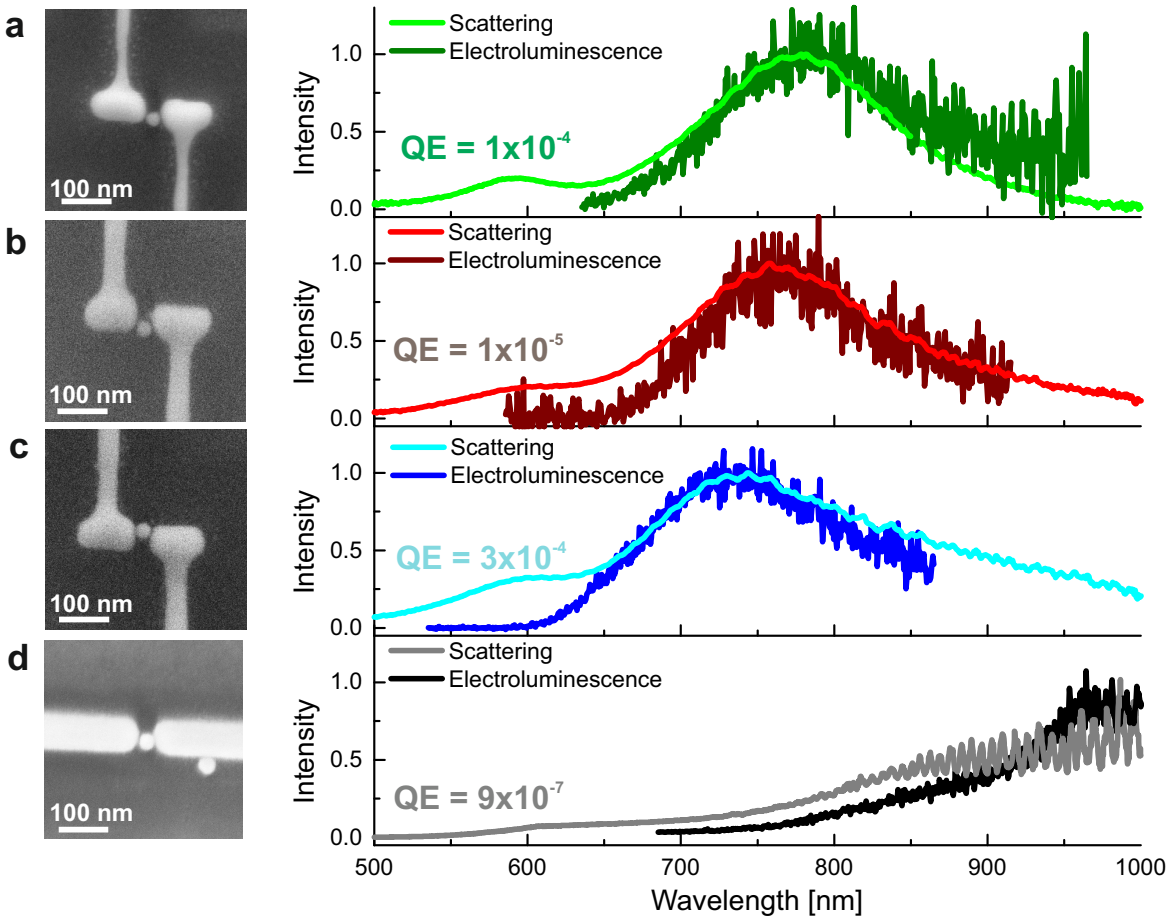

Figure 6.9: Electroluminescence and scattering spectra. **a-c** Investigated antenna geometries. **d** Non-resonant several micrometer long wire. The electron micrographs of the corresponding structures are shown on the left. The quantum efficiencies (QE) of the structures are stated in the respective graphs.

783, 763, 732 nm for structure a, b, c respectively. Consequently the emission spectra are dominated by the antenna resonance and can be tuned to the desired wavelength. The micrometer long wire, on the other hand, does not show any resonance and its emission spectrum increases in intensity for larger wavelengths.

By increasing the antenna length it is possible to further tune the emission wavelength to the infrared region. Shifting the emission wavelength to lower wavelengths can be achieved by shorter antenna length. However, gold exhibits damping due to interband transitions the green-blue spectral region and most likely alternative materials such as silver or aluminum need to be used.

From the detected photons and the simultaneously recorded tunneling current the quantum efficiency of the light emission process can be estimated. The quantum efficiency is defined as the number of emitted photons divided by the number of tunneling electrons. The obtained efficiencies range from $1{\cdot}10^{-5}$ to $1{\cdot}10^{-4}$ for the antenna-

based structures. The non-resonant wire exhibits a quantum efficiency of $9{\cdot}10^{-7}$. The best antenna shows a two order of magnitude higher efficiency compared to the non-resonant wire and a one order of magnitude larger efficiency than typical values for STM light emission under ambient conditions [189, 190]. This clearly demonstrates the enhancement of the photon generation process by exploiting the excellent radiative properties of the antenna.

6.5 Conclusion and Outlook

In conclusion, an electrically-driven sub-wavelength photon source has been realized. The antenna-based photon source integrates light control and generation into a planar single-material nanostructure. Upon applying a DC voltage between the antenna arms, electrons tunnel inelastically over the gap and are efficiently coupled to the antenna's local photonic density of states. Consequently, the emission wavelength is dictated by the antenna resonance and can be tuned by the geometry of the antenna. As expected, the polarization of the emitted light is found to be along the antenna axis and the obtained angular radiation patterns are dipolar. The quantum efficiency of the light emitting process is $1{\cdot}10^{-4}$ to $1{\cdot}10^{-5}$, which is two orders of magnitude larger than that of a non-resonant structure.

The presented sub-wavelength source based on lateral tunnel-junction inside the gap of a nanoantenna is not only a technological breakthrough but provides a large potential for further studies. One vision is to integrate the light source in a plasmonic nanocircuit [69]. Within the circuit the optical signal is processed and finally converted back into an electronic signal. Multiple colors can be fed into the circuit and the signal can be multi-plexed. An integrated optical transistor could be possibly realized by means of photon-assisted tunneling.

In addition, it would be exciting to imprint the fermionic nature of electrons onto photons in order to realize a source of single photons. In a theoretical study it has been shown that a single-channel quantum point contact can emit photons with a sub-Poissonian statistic [271]. In that sense, it would be very interesting to integrate a well-controlled quantum-point contact [265] into the antenna-based photon source and study the statistics of the emitted photons. Moreover, non-classical electrically-driven photon sources have been realized by means of the Coulomb-blockade effect [272] as well as from single quantum dots [273]. These structures could possibly benefit from the excellent radiative properties of the nanoantenna as well.

For all applications it is important to further improve the stability as well as the efficiency of the photon source. The tunneling junction could be stabilized by the evaporation of an insulator or by exploiting a covalent bond between the molecular layers on the gold particle and the antenna arms.

7 Summary and Outlook

Nano-antennas are an emerging concept for the manipulation and control of optical fields at the sub-wavelength scale. In analogy to their radio- and micro-wave counterparts they provide an efficient link between propagating and localized fields. Antennas operating at optical frequencies are typically on the order of a few hundred nanometer in size and are fabricated from noble metals. Upon excitation with an external field the electron gas inside the antenna can respond resonantly, if the dimensions of the antenna are chosen appropriate. Consequently, the resonance wavelength depends on the antenna dimensions. The electron-density oscillation is a hybrid state of electron and photon and is called a localized plasmon resonance. The oscillating currents within the antenna constitute a source for enhanced optical near-fields, which are strongly localized at the metal surface.

A particular interesting type of antennas are pairs of metal particles separated by a small insulating gap. For anti-symmetric gap modes charges of opposite sign reside across the gap. The dominating field-components are normal to the metal surface and due to the boundary conditions they are sizable only inside the gap. The attractive Coulomb interaction increases the surface-charge accumulation at the gap and enhanced optical fields occur within the insulating gap. The Coulomb interaction increases with decreasing gap size and extreme localization and strongest intensity enhancement is expected for small gap sizes.

In this thesis optical antennas with extremely small gaps, just slightly larger than inter-atomic distances, are investigated by means of optical and electrical excitation. In the case of electrical excitation electron tunneling across the antenna gap is exploited.

At the beginning of this thesis little was known about the optical properties of antennas with atomic scale gaps. Standard measurement techniques of field confinement and enhancement involving well-separated source, sample and detector are not applicable at atomic length-scales due to the interaction of the respective elements. Here, an elegant approach has been found. It is based on the fact that for closely-spaced metallic particles the energy splitting of a hybridized mode pair, consisting of symmetric and anti-symmetric mode, provides a direct measure for the Coulomb interaction over the gap. Gap antennas therefore possess an internal ruler which sensitively reports the size of the gap.

Upon self-assembly side-by-side aligned nanorods with gap sizes ranging from 2 to 0.5nm could be obtained. These antennas exhibit various symmetric and anti-symmetric modes in the visible range. In order to reveal optical modes of all symmetries a novel scattering setup has been developed and is successfully applied. Careful analysis of the optical spectra and comparison to numerical simulations suggests that extreme field confinement and localization can occur in gaps down to 0.5 nm. This is possibly the limit of plasmonic enhancement since for smaller gaps electron tunneling as well as non-locality of the dielectric function affect plasmonic resonances [43–46].

The strongly confined and intense optical fields provided by atomic-scale gaps are ideally suited for enhanced light-matter interaction. The interplay of intense optical-frequency fields and static electric fields or currents is of great interest for opto-electronic applications. In this thesis a concept has been developed, which allows for the electrical connection of optical antennas. By means of numerical simulations the concept was first verified for antennas with gap sizes on the order of 25 nm. It could be shown, that by attaching the leads at positions of a field minimum the resonant properties are nearly undisturbed. The resonance wavelengths shift only by a small amount with respect to isolated antennas and the numerically calculated near-field intensity enhancement is about 1000, which is just slightly lower than for an unconnected antenna. The antennas are fabricated from single-crystalline gold and exhibit superior optical and electrical properties. In particular, the conductivity is a factor of 4 larger with respect to multi-crystalline material, the resistance of the gap is as large as 1 TΩ and electric fields of at least 10^8 V/m can be continuously applied without damage. Optical scattering spectra reveal well-pronounced and tunable antenna resonances, which demonstrates the concept of electrically-connected antennas also experimentally.

By combining atomic-scale gaps and electrically-connected optical antennas a novel sub-wavelength photon source has been realized. To this end an antenna featuring an atomic scale gap is electrically driven by quantum tunneling across the antenna gap. The optical frequency components of this fluctuating current are efficiently converted to photons by the antenna. Consequently, light generation and control are integrated into a planar single-material nano-structure. Tunneling junctions are realized by positioning gold nanoparticles into the antenna gap, using an atomic force microscope. The presence of a stable tunneling junction between antenna and particle is demonstrated by measuring its distinct current-voltage characteristic. A DC voltage is applied to the junction and photons are generated by inelastically tunneling electrons via the enhanced local density of photonic states provided by the antenna resonance. The polarization of the emitted light is found to be along the antenna axis and the directivity is given by the dipolar antenna mode. By comparing electroluminescence and scattering spectra of different antennas, it has been shown that the spectrum of the generated light is determined by the geometry of the antenna. Moreover, the light generation process is enhanced by two orders of magnitude with respect to a non-resonant structure.

The controlled fabrication of the presented single-crystalline structures has not only pushed the frontiers of nano-technology, but the extreme confinement and enhancement of optical fields as well as the light generation by tunneling electrons lays a groundwork for a variety of fundamental studies and applications.

Field localization down to the (sub-)nanometer scale is a prerequisite for optical spectroscopy with near-atomic resolution. Indeed, recently first pioneering experiments have achieved molecular resolution exploiting plasmon-enhanced Raman scattering [12]. The small modal volume of antennas with atomic-scale gaps can lead to light-matter interaction in the strong coupling regime. Quantum electro-dynamical effects such as Rabi splitting or oscillations are likely when a single emitter is placed into resonant structures with atomic-scale gaps.

The concept of electrically-connected optical antennas is expected to be widely

applied within the emerging field of electro-plasmonics. The sub-wavelength photon source developed during this thesis will likely gain attention for future plasmonic nanocircuits. It is envisioned that in such a circuit the optical signal provided by the source is processed at ultrafast speed and nanometer-scales on the chip and is finally converted back into an electronic signal. An integrated optical transistor could be realized by means of photon-assisted tunneling. Moreover, it would be interesting to investigate, if it is possible to imprint the fermionic nature of electrons onto photons in order to realize an electrically-driven source of single photons. Non-classical light sources with the potential for on-chip integration could be built from electrically-connected antennas and are of great interest for quantum communication. To this end single emitters could be placed in the antenna gap or single electron tunneling could be achieved by means of a single-channel quantum point contact [274] or the Coulomb-blockade effect [272].

Zusammenfassung und Ausblick

Nanoantennen sind ein zukunftweisendes Konzept für die Manipulation und Kontrolle von optischen Feldern auf der Subwellenlängen-Skala. Analog zu Radio- und Mikrowellenantennen können sie auf effiziente Weise propagierende und lokalisierte Felder ineinander umwandeln. Optische Antennen sind typischerweise nur einige hundert Nanometer groß und werden aus Edelmetallen hergestellt. Besitzt die Antenne passende geometrische Maße, kann das Elektronengas durch Anregung mit einem externen Feld in resonante Schwingungen versetzt werden. Die Resonanzwellenlänge ist somit durch die Antennengeometrie bestimmt. Die Elektronendichte-Schwingung ist ein Hybridzustand aus Elektron und Photon und wird lokalisierte Plasmonenresonanz genannt. Wird die Resonanz angeregt so kommt es zu oszillierenden Strömen, welche eine Quelle für verstärkte optische Nahfelder darstellen. Diese Felder sind an die Metalloberfläche gebunden und daher stark lokalisiert.

Eine besonders interessante Antennengeometrie ist ein Paar von Metallpartikeln, die durch einen schmalen Spalt getrennt sind. Antisymmetrische Antennenmoden besitzen Ladungen mit entgegengesetzten Vorzeichen auf der jeweiligen Seite des Spalts. Die dominierenden elektrischen Felder stehen senkrecht zur Metalloberfläche und sind aufgrund der elektromagnetischen Randbedingungen hauptsächlich im Antennenspalt lokalisiert. Bei anti-symmetrischen Moden verstärkt die Coulombanziehung die Landungsträgerdichte in der Nähe des Spalts und es treten verstärkte optische Nahfelder zwischen den zwei Antennenarmen auf. Die Coulombwechselwirkung nimmt mit kleiner werdendem Abstand zu und für Strukturen mit sehr kleinem Abstand ist eine sehr große Feldverstärkung und eine sehr starke Lokalisation zu erwarten.

In dieser Dissertation wurden optische Antennen untersucht, deren zwei Antennenarme durch einen extrem schmalen Spalt in der Größenordnung von interatomaren Abständen getrennt sind. Eigenmoden der Antennen werden durch zwei fundamental verschiedene Mechanismen anregt: Entweder durch optische Anregung oder durch das Anlegen einer elektrischen Gleichspannung. Bei der zweiten Methode wird der quantenmechanische Elektron-Tunnelprozess ausgenutzt.

Zu Beginn dieser Arbeit existierten nur wenige Studien über Antennen mit sehr kleinen Spaltbreiten und es war nicht bekannt ob optische Felder auf atomarer Skala lokalisiert und verstärkt werden können. Allerdings ist eine direkte Messung der Feldlokalisation und Feldverstärkung auf atomarer Skala nicht möglich, da eine Unterscheidung zwischen Quelle, Probe und Detektor aufgrund deren gegenseitigen Wechselwirkungen schwierig ist. In dieser Arbeit wurde jedoch ein eleganter Ansatz entwickelt um dieses Problem zu umgehen. Dieser Ansatz nutzt aus, dass die energetische Aufspaltung eines hybridisierten Modenpaares, bestehend aus einer symmetrischen und anti-symmetrischen Mode, proportional zur Coulombwechselwirkung zwischen den Antennenarmen ist. Die Coulombwechselwirkung skaliert mit der Spaltbreite und somit gibt die energetische Aufspaltung der beiden Moden sehr genau den Abstand zwischen

den zwei Antennenarmen wieder.

Die untersuchten Strukturen waren zwei längsseitig-parallel liegende Nanostäbchen mit einem Abstand von 2 bis weniger als 0,5 nm. Diese Antennen konnten auf einfache Weise durch Selbstorganisation erhalten werden. Ein weiterer Grund für die Verwendung dieser Strukturen lag darin, dass bei ihnen symmetrische und anti-symmetrische Moden im sichtbaren Spektralbereich liegen. Um optische Moden jeglicher Symmetrie anregen zu können wurde in dieser Arbeit ein neuartiger experimenteller Aufbau zur Messung von Streuspektren entwickelt und erfolgreich eingesetzt. Sorgfältige Analysen der optischen Spektren und Vergleiche mit numerischen Rechnungen legen nahe, dass hohe Feldverstärkungen und Lokalisationen selbst für Strukturen mit Spaltbreiten von nur 0,5 nm auftreten. Möglicherweise erreichen die untersuchten Antennen die maximal möglichen Feldverstärkungen, denn für kleinere Abstände werden Plasmonenresonanzen durch elektronische Tunnelprozesse und nicht-lokale Effekte der dielektrischen Funktion geschwächt [43–46].

Die lokalisierten und verstärkten optischen Felder, die durch Antennen mit Spaltbreiten auf der Skala von atomaren Abständen erreicht werden können, eignen sich hervorragend für eine Verstärkung von Licht-Materie-Wechselwirkungen. Für optoelektronische Anwendungen ist hierbei das Wechselspiel zwischen Feldern mit optischen Frequenzen und statischen elektrischen Feldern oder Strömen von großem Interesse. In dieser Arbeit wurde ein Konzept erarbeitet, welches es ermöglicht optische Antennen elektrisch zu kontaktieren. Dieses Konzept wurde zunächst an Antennen mit circa 25 nm breiten Spalten mithilfe von numerischen Berechnungen verifiziert. Es konnte gezeigt werden, dass durch die Kontaktierung an den Positionen der Feldminima die Eigenmoden der Antenne nahezu unverändert bleiben. So liegen die Resonanzen der kontaktierten Antennen bei nahezu den gleichen Wellenlängen wie bei der unkontaktierten Antennen und die berechneten Feldverstärkungen sind mit einem Wert von 1000 nur minimal kleiner. Die Strukturen wurden aus einkristallinem Gold hergestellt und besitzen sehr gute optische und elektrische Eigenschaften. Beispielsweise ist die elektrische Leitfähigkeit viermal größer als bei multikristallinen Strukturen. Der elektrische Widerstand der Spalte ist circa 1 TΩ und elektrische Felder mit einer Stärke von mindestens 10^8 V/m können dauerhaft angelegt werden, ohne die Strukturen zu beschädigen. Mithilfe von Weißlicht-Streuexperimenten wurden die optischen Eigenschaften der hergestellten Strukturen untersucht. Die gemessenen Spektren zeigen wohl definierte Plasmonenresonanzen, deren Resonanzwellenlänge durch die Antennenlänge bestimmt ist. Somit konnte das Konzept auch experimentell bestätigt werden.

Durch Kombination von Spalten in der Größenordnung von atomaren Abständen mit elektrisch kontaktierten Antennen konnte eine Lichtquelle mit Abmessungen kleiner als die Lichtwellenlänge realisiert werden. Die Lichtquelle basiert auf einem neuartigen Mechanismus bei dem Photonen durch elektrisches Treiben der Antenne generiert werden. Die hierzu benötigten Felder mit optischen Frequenzen werden durch statistische Fluktuationen des quantenmechanischen Tunnelstromes bereitgestellt. Somit findet die Lichterzeugung und -kontrolle in einer planaren Nanostruktur statt, die nur aus einem einzelnen Material besteht. Um einen Tunnelkontakt zwischen den elektrisch kontaktierten Antennenarmen zu erreichen, wurden Goldnanopartikel mithilfe eines Rasterkraftmikroskops in dem Antennenspalt platziert. Zwischen dem Goldpar-

tikel und mindestens einem der Antennenarmen bildet sich dabei ein stabiler Tunnelkontakt, dessen Existenz durch die reproduzierbare Messung der charakteristischen Strom-Spannungskennlinie bewiesen werden konnte. Durch Anlegung einer konstanten Spannung kommt es zu inelastischen Tunnelprozessen bei denen Photonen erzeugt werden. Dabei wird die erhöhte optische Zustandsdichte der Antenne ausgenutzt, so dass das abgestrahlte Licht eine Polarisation entlang der Antennenachse zeigt und die räumliche Abstrahlcharakteristik durch die dipolartige Antennenmode bestimmt ist. Durch Variation der Antennengeometrie und durch Vergleich mit Streuspektren konnte gezeigt werden, dass die Wellenlänge des elektrisch erzeugten Lichts durch die Antennengeometrie bestimmt ist. Der Vergleich mit einer nicht-resonanten Referenzstruktur zeigt, dass die Antenne die Effizienz des Lichterzeugungsprozesses um zwei Größenordnungen erhöht.

Die in dieser Arbeit entwickelten Methoden zur kontrollierten Herstellung einkristalliner Nanoantennen mit Spaltbreiten auf der Skala von atomaren Abständen erweitern die Grenzen der Nanotechnologie. Darüber hinaus konnte gezeigt werden, dass lokalisierte und verstärkte optische Felder auf atomarer Skala existieren können und es wurde mit einer Gleichspannung mithilfe des inelastischen Tunnelprozesses Licht erzeugt. Diese Studien eröffnen vielfältige Möglichkeiten sowohl für Grundlagenforschung als auch praktische Anwendungen.

Die Lokalisation von optischen Feldern auf der (sub)-nanometer Skala ist die Voraussetzung für optische Spektroskopie nahe an der atomaren Auflösung. So konnte kürzlich in einem wegweisenden optischen Experiment molekulare Auflösung durch Messung von plasmonen verstärkter Ramanstreuung gezeigt werden [12]. Das kleine Modenvolumen von Antennen mit Spaltbreiten in der Größenordnung atomarer Abstände kann zu einer Licht-Materie-Wechselwirkung im Bereich der starken Kopplung führen. Dies hätte zur Folge, dass Quanten-Elektro-Dynamische Effekte wie Rabi-Aufspaltung oder -Oszillationen in Zukunft bei Experimenten, in denen einzelne Lichtemitter in sehr schmale Antennenspalte platziert sind, beobachtet werden können.

Es ist zu erwarten, dass elektrisch kontaktierte optische Antennen zukünftig in dem neuen Forschungsgebiet der Elektro-Plasmonik eingesetzt werden. Die entwickelte Subwellenlängen-Lichtquelle ist von großem Interesse für zukünftige plasmonische Nano-Schaltkreise. Es ist vorstellbar, dass optische Signale in solchen Schaltkreisen mit sehr hoher Geschwindigkeit auf der Nanoskala manipuliert werden und anschließend wieder in elektrische Signale umgewandelt werden können. Des Weiteren wäre es möglich einen optischen Transistor, basierend auf einer kontaktierten Antenne, zu integrieren. Die Schaltung des Transistors könnte durch den photon-unterstützten Tunneleffekt erreicht werden.

Ein weiteres interessantes Experiment in naher Zukunft wäre die Übertragung der fermionischen Eigenschaften von Elektronen auf Photonen, um eine elektrisch-getriebene Einzelphotonen-Quelle zu erhalten. Solch eine nicht-klassische Lichtquelle könnte aus elektrisch kontaktierten Antennen hergestellt werden und besäße das Potential zur Integration in Schaltkreise für Quantenkommunikations-Anwendungen. Ein Ansatz dafür wäre die Positionierung von Einzelemittern in den Antennenspalt. Ein anderer Ansatz könnte auf Einzel-Elektronen-Tunnelprozessen basieren, wie sie in Einkanal-Quantenpunktkontakten [274] oder aufgrund des Coulombblockade-Effektes [272] stattfinden.

List of Publications

J.S. Huang, J. Kern, P. Geisler, P. Weinmann, M. Kamp, A. Forchel, P. Biagioni, and B. Hecht.
Mode Imaging and Selection in Strongly Coupled Nanoantennas.
Nano Letters **10**, 2105–2110 (2010).

J.S. Huang, V. Callegari, P. Geisler, C. Brüning, J. Kern, J.C.Prangsma, X. Wu, T. Feichtner, J. Ziegler, P. Weinmann, M. Kamp, A. Forchel, P. Biagioni, U. Sennhauser, and B. Hecht.
Atomically flat single-crystalline gold nanostructures for plasmonic nanocircuitry.
Nature Communications **1**, 150 (2010).

J.C. Prangsma, J. Kern, A.G. Knapp, S. Grossmann, M. Emmerling, M. Kamp, and B. Hecht.
Electrically Connected Resonant Optical Antennas.
Nano Letters **12**, 2915–3919 (2012).

J. Kern, S. Großmann, N.V. Tarakina, T. Häckel, M. Emmerling, M. Kamp, J.S. Huang, P. Biagioni, J.C. Prangsma, and B. Hecht.
Atomic-Scale Confinement of Resonant Optical Fields.
Nano Letters **12**, 5504–5509 (2012).

P. Biagioni, D. Brida, J.S. Huang, J. Kern, L. Duò, B. Hecht, M. Finazzi, G. Cerullo.
Dynamics of multi-photon photoluminescence in gold nanoantennas.
Nano Letters **12**, 2941–2947 (2012).

J. Kern, R. Kullock, J.C. Prangsma, M. Emmerling, M. Kamp and B. Hecht.
Electrically-driven optical antenna.
In preparation.

Bibliography

[1] P. Kukura, M. Celebrano, A. Renn, and V. Sandoghdar.
Single-Molecule Sensitivity in Optical Absorption at Room Temperature.
Journal of Physical Chemistry Letters **1**, 3323–3327 (2010).

[2] M. Y. Berezin and S. Achilefu.
Fluorescence Lifetime Measurements and Biological Imaging.
Chemical Reviews **110**, 2641–2684 (2010).

[3] L. Novotny.
From near-field optics to optical antennas.
Physics Today **64**, 47–52 (2011).

[4] P. Bharadwaj, B. Deutsch, and L. Novotny.
Optical Antennas.
Advances in Optics and Photonics **1**, 438 (2009).

[5] P. Biagioni, J. S. Huang, and B. Hecht.
Nanoantennas for visible and infrared radiation.
Reports on Progress in Physics **75**, 024402 (2012).

[6] J. Dorfmüller, R. Vogelgesang, R. T. Weitz, C. Rockstuhl, C. Etrich, T. Pertsch, F. Lederer, and K. Kern.
Fabry-Pérot Resonances in One-Dimensional Plasmonic Nanostructures.
Nano Letters **9**, 2372–2377 (2009).

[7] P. Ghenuche, S. Cherukulappurath, T. H. Taminiau, N. F. van Hulst, and R. Quidant.
Spectroscopic Mode Mapping of Resonant Plasmon Nanoantennas.
Physical Review Letters **101**, 116805 (2008).

[8] E. J. R. Vesseur, R. de Waele, M. Kuttge, and A. Polman.
Direct Observation of Plasmonic Modes in Au Nanowires Using High-Resolution Cathodoluminescence Spectroscopy.
Nano Letters **7**, 2843–2846 (2007).

[9] J. Nelayah, M. Kociak, O. Stéphan, F. J. García de Abajo, M. Tencé, L. Henrard, D. Taverna, I. Pastoriza-Santos, L. M. Liz-Marzán, and C. Colliex.
Mapping surface plasmons on a single metallic nanoparticle.
Nature Physics **3**, 348–353 (2007).

[10] M. Aeschlimann, M. Bauer, D. Bayer, T. Brixner, S. Cunovic, F. Dimler, A. Fischer, W. Pfeiffer, M. Rohmer, C. Schneider, F. Steeb, C. Strüber, and D. V. Voronine.
Spatiotemporal control of nanooptical excitations.
PNAS **107**, 5329–5333 (2010).

[11] C. Höppener, Z. J. Lapin, P. Bharadwaj, and L. Novotny.
Self-Similar Gold-Nanoparticle Antennas for a Cascaded Enhancement of the Optical Field.
Physical Review Letters **109**, 017402 (2012).

[12] R. Zhang, Y. Zhang, Z. C. Dong, S. Jiang, C. Zhang, L. G. Chen, L. Zhang, Y. Liao, J. Aizpurua, Y. Luo, J. L. Yang, and J. G. Hou.
Chemical mapping of a single molecule by plasmon-enhanced Raman scattering.
Nature **498**, 82–86 (2013).

[13] C. C. Neacsu, J. Dreyer, N. Behr, and M. B. Raschke.
Scanning-probe Raman spectroscopy with single-molecule sensitivity.
Physical Review B **73**, 193406 (2006).

[14] T. Hanke, G. Krauss, D. Träutlein, B. Wild, R. Bratschitsch, and A. Leitenstorfer.
Efficient Nonlinear Light Emission of Single Gold Optical Antennas Driven by Few-Cycle Near-Infrared Pulses.
Physical Review Letters **103**, 257404 (2009).

[15] P. Mühlschlegel, H.-J. Eisler, M. O.J.F., H. B., and P. D.W.
Resonant Optical Antennas.
Science **308**, 1607–1609 (2005).

[16] M. Sivis, M. Duwe, B. Abel, and C. Ropers.
Extreme-ultraviolet light generation in plasmonic nanostructures.
Nature Physics **9**, 304–309 (2013).

[17] M. Schenk, M. Krüger, and P. Hommelhoff.
Strong-Field Above-Threshold Photoemission from Sharp Metal Tips.
Physical Review Letters **105**, 257601 (2010).

[18] G. Herink, D. R. Solli, M. Gulde, and C. Ropers.
Field-driven photoemission from nanostructures quenches the quiver motion.
Nature **483**, 190–193 (2012).

[19] S. Nie and S. Emory.
Probing Single Molecules and Single Nanoparticles by Surface-Enhanced Raman Scattering.
Science **275**, 1102–1106 (1997).

[20] P. Anger, P. Bharadwaj, and L. Novotny.
Enhancement and Quenching of Single-Molecule Fluorescence.
Physical Review Letters **96**, 113002 (2006).

[21] S. Kühn, U. Håkanson, L. Rogobete, and V. Sandoghdar.
Enhancement of Single-Molecule Fluorescence Using a Gold Nanoparticle as an Optical Nanoantenna.
Physical Review Letters **97**, 017402 (2006).

[22] A. Kinkhabwala, Z. Yu, S. Fan, Y. Avlasevich, K. Müllen, and W. E. Moerner.
Large single-molecule fluorescence enhancements produced by a bowtie nanoantenna.
Nature Photonics **3**, 654–657 (2009).

[23] S. Khatua, P. M. R. Paulo, H. Yuan, A. Gupta, P. Zijlstra, and M. Orrit.
Resonant Plasmonic Enhancement of Single-Molecule Fluorescence by Individual Gold Nanorods.
ACS Nano **4**, 4440–4449 (2014).

[24] A. G. Curto, G. Volpe, T. H. Taminiau, M. P. Kreuzer, R. Quidant, and N. F. van Hulst.
Unidirectional Emission of a Quantum Dot Coupled to a Nanoantenna.
Science **329**, 930–933 (2010).

[25] D. Dregely, R. Taubert, J. Dorfmüller, R. Vogelgesang, K. Kern, and H. Giessen.
3D optical Yagi-Uda nanoantenna array.
Nature Communications **2**, 267 (2011).

[26] T. Ming, L. Zhao, H. Chen, K. C. Woo, J. Wang, and H.-Q. Lin.
Experimental Evidence of Plasmophores: Plasmon-Directed Polarized Emission from Gold Nanorod–Fluorophore Hybrid Nanostructures.
Nano Letters **11**, 2296–2303 (2011).

[27] M. Ringler, A. Schwemer, M. Wunderlich, A. Nichtl, K. Kürzinger, T. Klar, and J. Feldmann.
Shaping Emission Spectra of Fluorescent Molecules with Single Plasmonic Nanoresonators.
Physical Review Letters **100**, 203002 (2008).

[28] E. LeRu, P. Etchegoin, J. Grand, N. Felidj, J. Aubard, and G. Levi.
Mechanisms of Spectral Profile Modification in Surface-Enhanced Fluorescence.
Journal of Physical Chemistry C **111**, 16076–16079 (2007).

[29] A. V. Akimov, A. Mukherjee, C. L. Yu, D. E. Chang, A. S. Zibrov, P. R. Hemmer, H. Park, and M. D. Lukin.
Generation of single optical plasmons in metallic nanowires coupled to quantum dots.
Nature **450**, 402–406 (2007).

[30] S. Schietinger, M. Barth, T. Aichele, and O. Benson.
Plasmon-Enhanced Single Photon Emission from a Nanoassembled Metal-Diamond Hybrid Structure at Room Temperature.
Nano Letters **9**, 1694–1698 (2009).

[31] N. T. Fofang, T.-H. Park, O. Neumann, N. A. Mirin, P. Nordlander, and N. J. Halas.
Plexcitonic Nanoparticles: Plasmon-Exciton Coupling in Nanoshell-J-Aggregate Complexes.
Nano Letters **8**, 3481–3487 (2008).

[32] N. T. Fofang, N. K. Grady, Z. Fan, A. O. Govorov, and N. J. Halas.
Plexciton Dynamics: Exciton-Plasmon Coupling in a J-Aggregate-Au Nanoshell Complex Provides a Mechanism for Nonlinearity.
Nano Letters **11**, 1556–1560 (2011).

[33] P. Vasa, W. Wang, R. Pomraenke, M. Lammers, M. Maiuri, C. Manzoni, G. Cerullo, and C. Lienau.

Real-time observation of ultrafast Rabi oscillations between excitons and plasmons in metal nanostructures with J-aggregates.
Nature Photonics **7**, 128–132 (2013).

[34] L. Tang, S. E. Kocabas, S. Latif, A. K. Okyay, D.-S. Ly-Gagnon, K. C. Saraswat, and D. A. B. Miller.
Nanometre-scale germanium photodetector enhanced by a near-infrared dipole antenna.
Nature Photonics **2**, 226–229 (2008).

[35] M. W. Knight, H. Sobhani, P. Nordlander, and N. J. Halas.
Photodetection with Active Optical Antennas.
Science **332**, 702–704 (2011).

[36] P. Fan, K. C. Y. Huang, L. Cao, and M. L. Brongersma.
Redesigning Photodetector Electrodes as an Optical Antenna.
Nano Letters **13**, 392–396 (2013).

[37] H. A. Atwater and A. Polman.
Plasmonics for improved photovoltaic devices.
Nature Materials **9**, 205–213 (2010).

[38] S. Linic, P. Christopher, and D. B. Ingram.
Plasmonic-metal nanostructures for efficient conversion of solar to chemical energy.
Nature Materials **10**, 911–921 (2011).

[39] D. Koller, A. Hohenau, H. Ditlbacher, N. Galler, F. Reil, F. Aussenegg, A. Leitner, E. List, and J. Krenn.
Organic plasmon-emitting diode.
Nature Photonics **2**, 684–687 (2008).

[40] K. Okamoto, I. Niki, A. Shvartser, Y. Narukawa, T. Mukai, and A. Scherer.
Surface-plasmon-enhanced light emitters based on InGaN quantum wells.
Nature Materials **3**, 601–605 (2004).

[41] M. T. Hill, Y.-S. Oei, B. Smalbrugge, Y. Zhu, T. de Vries, P. J. van Veldhoven, F. W. M. van Otten, T. J. Eijkemans, J. P. Turkiewicz, H. de Waardt, E. J. Geluk, S.-H. Kwon, Y.-H. Lee, R. Nötzel, and M. K. Smit.
Lasing in metallic-coated nanocavities.
Nature Photonics **1**, 589–594 (2007).

[42] K. Ding, Z. C. Liu, L. J. Yin, M. T. Hill, M. J. H. Marell, P. J. van Veldhoven, R. Nöetzel, and C. Z. Ning.
Room-temperature continuous wave lasing in deep-subwavelength metallic cavities under electrical injection.
Physical Review B **85**, 041301 (2012).

[43] C. Ciracì, R. T. Hill, J. J. Mock, Y. Urzhumov, A. I. Fernández-Domínguez, S. A. Maier, J. B. Pendry, A. Chilkoti, and D. R. Smith.
Probing the Ultimate Limits of Plasmonic Enhancement.
Science **337**, 1072–1074 (2012).

[44] K. J. Savage, M. M. Hawkeye, R. Esteban, A. G. Borisov, J. Aizpurua, and J. J. Baumberg.
Revealing the quantum regime in tunnelling plasmonics.
Nature **491**, 574–577 (2012).

[45] S. F. Tan, L. Wu, J. K. W. Yang, P. Bai, M. Bosman, and C. A. Nijhuis.
Quantum Plasmon Resonances Controlled by Molecular Tunnel Junctions.
Science **343**, 1496–1499 (2014).

[46] J. A. Scholl, A. García-Etxarri, A. L. Koh, and J. A. Dionne.
Observation of Quantum Tunneling between Two Plasmonic Nanoparticles.
Nano Letters **13**, 564–569 (2013).

[47] P. West, S. Ishii, G. Naik, N. Emani, V. Shalaev, and A. Boltasseva.
Searching for better plasmonic materials.
Laser & Photonics Reviews **4**, 795–808 (2010).

[48] P. Tassin, T. Koschny, M. Kafesaki, and C. M. Soukoulis.
A comparison of graphene, superconductors and metals as conductors for metamaterials and plasmonics.
Nature Photonics **6**, 259–264 (2012).

[49] G. V. Naik, V. M. Shalaev, and A. Boltasseva.
Alternative Plasmonic Materials: Beyond Gold and Silver.
Advanced Materials **25**, 3264–3294 (2013).

[50] L. Novotny and B. Hecht.
Principles of Nano-Optics.
Second edition. Cambridge University Press (2012).

[51] P. B. Johnson and R. W. Christy.
Optical Constants of the Noble Metals.
Physical Review B **6**, 4370–4379 (1972).

[52] G. Toscano, S. Raza, A.-P. Jauho, N. A. Mortensen, and M. Wubs.
Modified field enhancement and extinction by plasmonic nanowire dimers due to non-local response.
Optics Express **20**, 4176–4188 (2012).

[53] C. F. Bohren and D. R. Huffman.
Absorption and Scattering of Light by Small Particles.
Wiley-VCH Verlag GmbH (2007).

[54] H. C. van de Hulst.
Light scattering: by small particles.
Courier Dover Publications (1981).

[55] P. Melchior, D. Bayer, and M. Aeschlimann.
Probing and imaging of optical antennas with PEEM.
In *Optical Antennas.* Cambridge University Press (2013).

[56] C. Deeb, R. Bachelot, J. Plain, A.-L. Baudrion, S. Jradi, A. Bouhelier, O. Soppera, P. K. Jain, L. Huang, C. Ecoffet, L. Balan, and P. Royer.
Quantitative Analysis of Localized Surface Plasmons Based on Molecular Probing.
ACS Nano **4**, 4579–4586 (2010).

[57] T. Geldhauser, A. Kolloch, N. Murazawa, K. Ueno, J. Boneberg, P. Leiderer, E. Scheer, and H. Misawa.
Quantitative Measurement of the Near-Field Enhancement of Nanostructures by Two-Photon Polymerization.
Langmuir **28**, 9041–9046 (2012).

[58] M. Husnik, M. W. Klein, N. Feth, M. König, J. Niegemann, K. Busch, S. Linden, and M. Wegener.
Absolute extinction cross-section of individual magnetic split-ring resonators.
Nature Photonics **2**, 614–617 (2008).

[59] T. R. Jensen, G. C. Schatz, and R. P. Van Duyne.
Nanosphere Lithography: Surface Plasmon Resonance Spectrum of a Periodic Array of Silver Nanoparticles by Ultraviolet-Visible Extinction Spectroscopy and Electrodynamic Modeling.
Journal of Physical Chemistry B **103**, 2394–2401 (1999).

[60] S. L. Westcott, J. B. Jackson, C. Radloff, and N. J. Halas.
Relative contributions to the plasmon line shape of metal nanoshells.
Physical Review B **66**, 155431 (2002).

[61] C. Sönnichsen, T. Franzl, T. Wilk, G. von Plessen, J. Feldmann, O. Wilson, and P. Mulvaney.
Drastic Reduction of Plasmon Damping in Gold Nanorods.
Physical Review Letters **88**, 077402 (2002).

[62] A. M. Funston, C. Novo, T. J. Davis, and P. Mulvaney.
Plasmon Coupling of Gold Nanorods at Short Distances and in Different Geometries.
Nano Letters **9**, 1651–1658 (2009).

[63] D. P. Fromm, A. Sundaramurthy, P. J. Schuck, G. Kino, and W. E. Moerner.
Gap-Dependent Optical Coupling of Single "Bowtie" Nanoantennas Resonant in the Visible.
Nano Letters **4**, 957–961 (2004).

[64] J. Schäfer.
Implementierung und Anwendung analytischer und numerischer Verfahren zur Lösung der Maxwellgleichungen für die Untersuchung der Lichtausbreitung in biologischem Gewebe.
Ph.D. thesis, Ulm (2011).

[65] D. Boyer, P. Tamarat, A. Maali, B. Lounis, and M. Orrit.
Photothermal Imaging of Nanometer-Sized Metal Particles Among Scatterers.
Science **297**, 1160–1163 (2002).

[66] H. Ditlbacher, A. Hohenau, D. Wagner, U. Kreibig, M. Rogers, F. Hofer, F. R. Aussenegg, and J. R. Krenn.
Silver Nanowires as Surface Plasmon Resonators.
Physical Review Letters **95**, 257403 (2005).

[67] E. S. Barnard, J. S. White, A. Chandran, and M. L. Brongersma.
Spectral properties of plasmonic resonator antennas.
Optics Express **16**, 16529–16537 (2008).

[68] T. H. Taminiau, F. D. Stefani, and N. F. van Hulst.
Optical Nanorod Antennas Modeled as Cavities for Dipolar Emitters: Evolution of Sub- and Super-Radiant Modes.
Nano Letters **11**, 1020–1024 (2011).

[69] J.-S. Huang, T. Feichtner, P. Biagioni, and B. Hecht.
Impedance Matching and Emission Properties of Nanoantennas in an Optical Nanocircuit.
Nano Letters **9**, 1897–1902 (2009).

[70] L. Novotny.
Effective Wavelength Scaling for Optical Antennas.
Physical Review Letters **98**, 266802 (2007).

[71] A. G. Curto, T. H. Taminiau, G. Volpe, M. P. Kreuzer, R. Quidant, and N. F. van Hulst.
Multipolar radiation of quantum emitters with nanowire optical antennas.
Nature Communications **4**, 1750 (2013).

[72] W. Rechberger, A. Hohenau, A. Leitner, J. Krenn, B. Lamprecht, and F. Aussenegg.
Optical properties of two interacting gold nanoparticles.
Optics Communications **220**, 137–141 (2003).

[73] J.-S. Huang, V. Callegari, P. Geisler, C. Brüning, J. Kern, J. C. Prangsma, X. Wu, T. Feichtner, J. Ziegler, P. Weinmann, M. Kamp, A. Forchel, P. Biagioni, U. Sennhauser, and B. Hecht.
Atomically flat single-crystalline gold nanostructures for plasmonic nanocircuitry.
Nature Communications **1**, 150 (2010).

[74] E. Prodan, C. Radloff, N. Halas, and P. Nordlander.
A Hybridization Model for the Plasmon Response of Complex Nanostructures.
Science **302**, 419–422 (2003).

[75] J.-S. Huang, J. Kern, P. Geisler, P. Weinmann, M. Kamp, A. Forchel, P. Biagioni, and B. Hecht.
Mode Imaging and Selection in Strongly Coupled Nanoantennas.
Nano Letters **10**, 2105–2110 (2010).

[76] S.-C. Yang, H. Kobori, C.-L. He, M.-H. Lin, H.-Y. Chen, C. Li, M. Kanehara, T. Teranishi, and S. Gwo.
Plasmon Hybridization in Individual Gold Nanocrystal Dimers: Direct Observation of Bright and Dark Modes.
Nano Letters **10**, 632–637 (2010).

[77] L. S. Slaughter, Y. Wu, B. A. Willingham, P. Nordlander, and S. Link.
Effects of Symmetry Breaking and Conductive Contact on the Plasmon Coupling in Gold Nanorod Dimers.
ACS Nano **4**, 4657–4666 (2010).

[78] D. P. Lyvers, J.-M. Moon, A. V. Kildishev, V. M. Shalaev, and A. Wei.
Gold Nanorod Arrays as Plasmonic Cavity Resonators.
ACS Nano **2**, 2569–2576 (2008).

[79] S. Marhaba, G. Bachelier, C. Bonnet, M. Broyer, E. Cottancin, N. Grillet, J. Lerme, J.-L. Vialle, and M. Pellarin.
Surface Plasmon Resonance of Single Gold Nanodimers near the Conductive Contact Limit.
The Journal of Physical Chemistry C **113**, 4349–4356 (2009).

[80] B. Luk'yanchuk, N. I. Zheludev, S. A. Maier, N. J. Halas, P. Nordlander, H. Giessen, and C. T. Chong.
The Fano resonance in plasmonic nanostructures and metamaterials.
Nature Materials **9**, 707–715 (2010).

[81] J. Lermé, H. Baida, C. Bonnet, M. Broyer, E. Cottancin, A. Crut, P. Maioli, N. Del Fatti, F. Vallée, and M. Pellarin.
Size Dependence of the Surface Plasmon Resonance Damping in Metal Nanospheres.
The Journal of Physical Chemistry Letters **1**, 2922–2928 (2010).

[82] M. Melli, A. Polyakov, D. Gargas, C. Huynh, L. Scipioni, W. Bao, D. F. Ogletree, P. J. Schuck, S. Cabrini, and A. Weber-Bargioni.
Reaching the Theoretical Resonance Quality Factor Limit in Coaxial Plasmonic Nanoresonators Fabricated by Helium Ion Lithography.
Nano Letters **13**, 2687–2691 (2013).

[83] J. G. Simmons.
Conduction in thin dielectric films.
Journal of Physics D: Applied Physics **4**, 613 (1971).

[84] C. Koughia and S. Kasap.
Springer Handbook of Electronic and Photonic Materials, volume Thin Films Electronic Properties.
Springer (2007).

[85] F. A. Pizzarello.
CdS Thin-Film Formation by the Method of Co-evaporation.
Journal of Applied Physics **35**, 2730–2732 (1964).

[86] T. Budinas, P. Mačkus, A. Smilga, and J. Viščakas.
Space-Charge-Limited Currents in Vitreous Antimony Trisulfide Films.
physica status solidi (b) **31**, 375–380 (1969).

[87] A. Rose.
Space-Charge-Limited Currents in Solids.
Physical Review **97**, 1538–1544 (1955).

[88] M. A. Lampert.
Volume-controlled current injection in insulators.
Reports on Progress in Physics **27**, 329 (1964).

[89] M. Stuart.
Conduction in silicon oxide films.
British Journal of Applied Physics **18**, 1637 (1967).

[90] A. Servini and A. K. Jonscher.
Electrical conduction in evaporated silicon oxide films.
Thin Solid Films **3**, 341–365 (1969).

[91] R. Gould and M. Lopez.
Poole-Frenkel conductivity prior to electroforming in evaporated Au-SiOx-Au sandwich structures.
Thin Solid Films **343–344**, 94–97 (1999).

[92] S. M. Sze.
Current Transport and Maximum Dielectric Strength of Silicon Nitride Films.
Journal of Applied Physics **38**, 2951–2956 (1967).

[93] J. G. Simmons.
Poole-Frenkel effect and Schottky effect in metal-insulator-metal systems.
Physical Review **155**, 657 (1967).

[94] N. F. Mott and E. A. Davis.
Electronic Processes in Non-Crystalline Materials.
Oxford University Press (2012).

[95] M. Fujii, Y. Inoue, S. Hayashi, and K. Yamamoto.
Hopping conduction in SiO2 films containing C, Si, and Ge clusters.
Applied Physics Letters **68**, 3749 (1996).

[96] P. R. Emtage and W. Tantraporn.
Schottky Emission Through Thin Insulating Films.
Physical Review Letters **8**, 267–268 (1962).

[97] M. Ilyas, C. A. Hogarth, and R. Harani.
A study of high-field electrical conduction and of optical absorption of SiO/SnO2 thin films.
Journal of Materials Science Letters **3**, 703–706 (1984).

[98] J. Jahanmir, P. E. West, and T. N. Rhodin.
Evidence of Schottky emission in scanning tunneling microscopes operated in ambient air.
Applied Physics Letters **52**, 2086–2088 (1988).

[99] H. Lüth.
Solid Surfaces, Interfaces and Thin Films.
Springer (2001).

[100] S. Hüfner.
Photoelectron Spectroscopy: Principles and Applications.
Springer (2003).

[101] S. G. p. Davison and M. Stęślicka.
Basic Theory of Surface States.
Oxford University Press (1996).

[102] G. Dearnaley, A. M. Stoneham, and D. V. Morgan.
Electrical phenomena in amorphous oxide films.
Reports on Progress in Physics **33**, 1129 (1970).

[103] J. Yao, L. Zhong, D. Natelson, and J. M. Tour.
In situ imaging of the conducting filament in a silicon oxide resistive switch.
Scientific Reports **2**, 242 (2012).

[104] J. Yao, L. Zhong, D. Natelson, and J. M. Tour.
Silicon Oxide: A Non-innocent Surface for Molecular Electronics and Nanoelectronics Studies.
Journal of the American Chemical Society **133**, 941–948 (2011).

[105] W. Shockley, W. W. Hooper, H. J. Queisser, and W. Schroen.
Mobile electric charges on insulating oxides with application to oxide covered silicon pn junctions.
Surface Science **2**, 277–287 (1964).

[106] J. Voorthuyzen, K. Keskin, and P. Bergveld.
Investigations of the surface conductivity of silicon dioxide and methods to reduce it.
Surface Science **187**, 201–211 (1987).

[107] J. G. Simmons.
Generalized Formula for the Electric Tunnel Effect between Similar Electrodes Separated by a Thin Insulating Film.
Journal of Applied Physics **34**, 1793–1803 (1963).

[108] I. Bâldea and H. Köppel.
Transition voltage spectroscopy in vacuum break junction: The standard tunneling barrier model and beyond.
physica status solidi (b) **249**, 1791–1804 (2012).

[109] J. G. Simmons.
Potential Barriers and Emission Limited Current Flow Between Closely Spaced Parallel Metal Electrodes.
Journal of Applied Physics **35**, 2472–2481 (1964).

[110] P. Jennings and R. Jones.
Beyond the method of images—the interaction of charged particles with real surfaces.
Advances in Physics **37**, 341–358 (1988).

[111] Y. Kuk and P. J. Silverman.
Scanning tunneling spectroscopy of metal surfaces.
Journal of Vacuum Science & Technology A **8**, 289–292 (1990).

[112] J. K. Gimzewski and R. Möller.
Transition from the tunneling regime to point contact studied using scanning tunneling microscopy.
Physical Review B **36**, 1284–1287 (1987).

[113] L. Olesen, M. Brandbyge, M. R. Sørensen, K. W. Jacobsen, E. Lægsgaard, I. Stensgaard, and F. Besenbacher.
Apparent barrier height in scanning tunneling microscopy revisited.
Physical Review Letters **76**, 1485 (1996).

[114] M. L. Trouwborst, E. H. Huisman, F. L. Bakker, S. J. van der Molen, and B. J. van Wees.
Single Atom Adhesion in Optimized Gold Nanojunctions.
Physical Review Letters **100**, 175502 (2008).

[115] S. C. Meepagala and F. Real.
Detailed experimental investigation of the barrier-height lowering and the tip-sample force gradient during STM operation in air.
Physical Review B **49**, 10761–10763 (1994).

[116] A. Mangin, A. Anthore, M. L. Della Rocca, E. Boulat, and P. Lafarge.
Reduced work functions in gold electromigrated nanogaps.
Physical Review B **80** (2009).

[117] M. F. Lambert, M. F. Goffman, J. P. Bourgoin, and P. Hesto.
Fabrication and characterization of sub-3 nm gaps for single-cluster and single-molecule experiments.
Nanotechnology **14**, 772 (2003).

[118] M. L. Trouwborst, C. A. Martin, R. H. M. Smit, C. M. Guédon, T. A. Baart, S. J. van der Molen, and J. M. van Ruitenbeek.
Transition Voltage Spectroscopy and the Nature of Vacuum Tunneling.
Nano Letters **11**, 614–617 (2011).

[119] G. Konstantatos and E. H. Sargent.
Nanostructured materials for photon detection.
Nature Nanotechnology **5**, 391–400 (2010).

[120] T. Ishi, J. Fujikata, K. Makita, T. Baba, and K. Ohashi.
Si nano-photodiode with a surface plasmon antenna.
Japanese Journal of Applied Physics **44**, L364 (2005).

[121] C. Clavero.
Plasmon-induced hot-electron generation at nanoparticle/metal-oxide interfaces for photovoltaic and photocatalytic devices.
Nature Photonics **8**, 95–103 (2014).

[122] C. Ropers, D. R. Solli, C. P. Schulz, C. Lienau, and T. Elsaesser.
Localized multiphoton emission of femtosecond electron pulses from metal nanotips.
Physical Review Letters **98**, 43907 (2007).

[123] P. Hommelhoff, Y. Sortais, A. Aghajani-Talesh, and M. A. Kasevich.
Field Emission Tip as a Nanometer Source of Free Electron Femtosecond Pulses.
Physical Review Letters **96**, 077401 (2006).

[124] P. Dombi, A. Hörl, P. Rácz, I. Márton, A. Trügler, J. R. Krenn, and U. Hohenester.
Ultrafast Strong-Field Photoemission from Plasmonic Nanoparticles.
Nano Letters **13**, 674–678 (2013).

[125] M. Krüger, M. Schenk, and P. Hommelhoff.
Attosecond control of electrons emitted from a nanoscale metal tip.
Nature **475**, 78–81 (2011).

[126] C. J. Powell and J. B. Swan.
Origin of the Characteristic Electron Energy Losses in Aluminum.
Physical Review **115**, 869–875 (1959).

[127] A. L. Koh, A. I. Fernández-Domínguez, D. W. McComb, S. A. Maier, and J. K. W. Yang.
High-Resolution Mapping of Electron-Beam-Excited Plasmon Modes in Lithographically Defined Gold Nanostructures.
Nano Letters **11**, 1323–1330 (2011).

[128] F. von Cube, S. Irsen, J. Niegemann, C. Matyssek, W. Hergert, K. Busch, and S. Linden.
Spatio-spectral characterization of photonic meta-atoms with electron energy-loss spectroscopy [Invited].
Optical Materials Express **1**, 1009–1018 (2011).

[129] N. Yamamoto, K. Araya, and F. García de Abajo.
Photon emission from silver particles induced by a high-energy electron beam.
Physical Review B **64** (2001).

[130] F. J. García de Abajo.
Optical excitations in electron microscopy.
Reviews of Modern Physics **82**, 209–275 (2010).

[131] R. J. Walters, R. V. A. van Loon, I. Brunets, J. Schmitz, and A. Polman.
A silicon-based electrical source of surface plasmon polaritons.
Nature Materials **9**, 21–25 (2010).

[132] D. M. O'Carroll, C. E. Hofmann, and H. A. Atwater.
Conjugated Polymer/Metal Nanowire Heterostructure Plasmonic Antennas.
Advanced Materials **22**, 1223–1227 (2010).

[133] S. Pillai, K. R. Catchpole, T. Trupke, G. Zhang, J. Zhao, and M. A. Green.
Enhanced emission from Si-based light-emitting diodes using surface plasmons.
Applied Physics Letters **88**, 161102 (2006).

[134] C. Liu, V. Kamaev, and Z. V. Vardeny.
Efficiency enhancement of an organic light-emitting diode with a cathode forming two-dimensional periodic hole array.
Applied Physics Letters **86**, 143501 (2005).

[135] Y. C. Jun, K. C. Huang, and M. L. Brongersma.
Plasmonic beaming and active control over fluorescent emission.
Nature Communications **2**, 283 (2011).

[136] W. Zhang, L. Huang, C. Santschi, and O. J. F. Martin.
Trapping and Sensing 10 nm Metal Nanoparticles Using Plasmonic Dipole Antennas.
Nano Letters **10**, 1006–1011 (2010).

[137] K. C. Y. Huang, M.-K. Seo, T. Sarmiento, Y. Huo, J. S. Harris, and M. L. Brongersma.
Electrically driven subwavelength optical nanocircuits.
Nature Photonics **8**, 244–249 (2014).

[138] J. Berthelot, A. Bouhelier, C. Huang, J. Margueritat, G. Colas-des Francs, E. Finot, J.-C. Weeber, A. Dereux, S. Kostcheev, H. I. E. Ahrach, A.-L. Baudrion, J. Plain, R. Bachelot, P. Royer, and G. P. Wiederrecht.
Tuning of an Optical Dimer Nanoantenna by Electrically Controlling Its Load Impedance.
Nano Letters **9**, 3914–3921 (2009).

[139] S. Khatua, W.-S. Chang, P. Swanglap, J. Olson, and S. Link.
Active Modulation of Nanorod Plasmons.
Nano Letters **11**, 3797–3802 (2011).

[140] W. Dickson, G. A. Wurtz, P. R. Evans, R. J. Pollard, and A. V. Zayats.
Electronically Controlled Surface Plasmon Dispersion and Optical Transmission through Metallic Hole Arrays Using Liquid Crystal.
Nano Letters **8**, 281–286 (2008).

[141] Z. L. Sámson, K. F. MacDonald, F. De Angelis, B. Gholipour, K. Knight, C. C. Huang, E. Di Fabrizio, D. W. Hewak, and N. I. Zheludev.
Metamaterial electro-optic switch of nanoscale thickness.
Applied Physics Letters **96**, 143105 (2010).

[142] W. Cai, A. P. Vasudev, and M. L. Brongersma.
Electrically Controlled Nonlinear Generation of Light with Plasmonics.
Science **333**, 1720–1723 (2011).

[143] D. R. Ward, F. Hüser, F. Pauly, J. C. Cuevas, and D. Natelson.
Optical rectification and field enhancement in a plasmonic nanogap.
Nature Nanotechnology **5**, 732–736 (2010).

[144] J. Lambe and S. L. McCarthy.
Light emission from inelastic electron tunneling.
Physical Review Letters **37**, 923–925 (1976).

[145] S. L. McCarthy and J. Lambe.
LEIT effect in metal-insulator-semiconductor tunnel junctions.
Applied Physics Letters **33**, 858–860 (1978).

[146] P. K. Hansma and H. P. Broida.
Light emission from gold particles excited by electron tunneling.
Applied Physics Letters **32**, 545 (1978).

[147] R. W. Rendell, D. J. Scalapino, and B. Mühlschlegel.
Role of Local Plasmon Modes in Light Emission from Small-particle Tunnel Junctions.
Physical Review Letters **41**, 1746–1750 (1978).

[148] R. W. Rendell and D. J. Scalapino.
Surface plasmons confined by microstructures on tunnel junctions.
Physical Review B **24**, 3276–3294 (1981).

[149] D. Hone, B. Mühlschlegel, and D. J. Scalapino.
Theory of light emission from small particle tunnel junctions.
Applied Physics Letters **33**, 203 (1978).

[150] N. L. Schneider, G. Schull, and R. Berndt.
Optical Probe of Quantum Shot-Noise Reduction at a Single-Atom Contact.
Physical Review Letters **105**, 026601 (2010).

[151] C. B. Duke.
Tunneling in solids.
Academic Press (1969).

[152] A. Adams, J. C. Wyss, and P. K. Hansma.
Possible Observation of Local Plasmon Modes Excited by Electrons Tunneling through Junctions.
Physical Review Letters **42**, 912–915 (1979).

[153] B. Laks and D. L. Mills.
Photon emission from slightly roughened tunnel junctions.
Physical Review B **20**, 4962–4980 (1979).

[154] J. Kirtley, T. N. Theis, and J. C. Tsang.
Light emission from tunnel junctions on gratings.
Physical Review B **24**, 5650–5663 (1981).

[155] J. R. Kirtley, T. N. Theis, J. C. Tsang, and D. J. DiMaria.
Hot-electron picture of light emission from tunnel junctions.
Physical Review B **27**, 4601–4611 (1983).

[156] B. N. J. Persson and A. Baratoff.
Theory of photon emission in electron tunneling to metallic particles.
Physical Review Letters **68**, 3224–3227 (1992).

[157] Szentirmay Z.
Surface plasmon assisted electron-photon interaction in metal-oxide-metal layered structures.
Progress in quantum electronics **15**, 175–230 (1991).

[158] G. Binnig and H. Rohrer.
Scanning tunneling microscopy—from birth to adolescence.
Reviews of Modern Physics **59**, 615–625 (1987).

[159] J. H. Coombs, J. K. Gimzewski, B. Reihl, J. K. Sass, and R. R. Schlittler.
Photon emission experiments with the scanning tunnelling microscope.
Journal of Microscopy **152**, 325–336 (1988).

[160] J. K. Gimzewski, J. K. Sass, R. R. Schlitter, and J. Schott.
Enhanced Photon Emission in Scanning Tunnelling Microscopy.
Europhysics Letters **8**, 435 (1989).

[161] R. Berndt.
Photon emission scanning tunneling microscope.
Journal of Vacuum Science & Technology B: Microelectronics and Nanometer Structures **9**, 573 (1991).

[162] P. Johansson, R. Monreal, and P. Apell.
Theory for light emission from a scanning tunneling microscope.
Physical Review B **42**, 9210–9213 (1990).

[163] J. Aizpurua, S. P. Apell, and R. Berndt.
Role of tip shape in light emission from the scanning tunneling microscope.
Physical Review B **62**, 2065–2073 (2000).

[164] R. Berndt, R. Gaisch, J. K. Gimzewski, B. Reihl, R. R. Schlittler, W. D. Schneider, and M. Tschudy.
Photon Emission at Molecular Resolution Induced by a Scanning Tunneling Microscope.
Science **262**, 1425–1427 (1993).

[165] X. Tao, Z. C. Dong, J. L. Yang, Y. Luo, J. G. Hou, and J. Aizpurua.
Influence of a dielectric layer on photon emission induced by a scanning tunneling microscope.
The Journal of Chemical Physics **130**, 084706–084706–8 (2009).

[166] M. G. Boyle, J. Mitra, and P. Dawson.
The tip–sample water bridge and light emission from scanning tunnelling microscopy.
Nanotechnology **20**, 335202 (2009).

[167] P. Johansson.
Light emission from a scanning tunneling microscope: Fully retarded calculation.
Physical Review B **58**, 10823 (1998).

[168] K. Meguro, K. Sakamoto, R. Arafune, M. Satoh, and S. Ushioda.
Origin of multiple peaks in the light emission spectra of a Au(111) surface induced by the scanning tunneling microscope.
Physical Review B **65**, 165405 (2002).

[169] V. Sivel, R. Coratger, F. Ajustron, and J. Beauvillain.
Photon emission stimulated by scanning tunneling microscopy in air.
Physical Review B **45**, 8634–8637 (1992).

[170] H. Wang, J. Jing, H. T. Chu, and P. N. Henriksen.
Rearrangement of Au(111) surface as a result of scanning with scanning tunneling/atomic force microscopes.
Journal of Vacuum Science & Technology B: Microelectronics and Nanometer Structures **11**, 2000–2005 (1993).

[171] G. Schull, M. Becker, and R. Berndt.
Imaging Confined Electrons with Plasmonic Light.
Physical Review Letters **101**, 136801 (2008).

[172] G. V. Nazin, X. H. Qiu, and W. Ho.
Atomic Engineering of Photon Emission with a Scanning Tunneling Microscope.
Physical Review Letters **90**, 216110 (2003).

[173] C. Chen, C. A. Bobisch, and W. Ho.
Visualization of Fermi's Golden Rule Through Imaging of Light Emission from Atomic Silver Chains.
Science **325**, 981–985 (2009).

[174] P. Myrach, N. Nilius, and H.-J. Freund.
Photon mapping of individual Ag particles on MgO/Mo(001).
Physical Review B **83**, 035416 (2011).

[175] F. Silly, A. O. Gusev, A. Taleb, F. Charra, and M.-P. Pileni.
Coupled Plasmon Modes in an Ordered Hexagonal Monolayer of Metal Nanoparticles: A Direct Observation.
Physical Review Letters **84**, 5840–5843 (2000).

[176] N. L. Schneider, P. Johansson, and R. Berndt.
Hot electron cascades in the scanning tunneling microscope.
Physical Review B **87**, 045409 (2013).

[177] T. Wang, E. Boer-Duchemin, Y. Zhang, G. Comtet, and G. Dujardin.
Excitation of propagating surface plasmons with a scanning tunnelling microscope.
Nanotechnology **22**, 175201 (2011).

[178] P. Bharadwaj, A. Bouhelier, and L. Novotny.
Electrical Excitation of Surface Plasmons.
Physical Review Letters **106**, 226802 (2011).

[179] S. F. Alvarado, P. Renaud, D. L. Abraham, C. Schönenberger, D. J. Arent, and H. P. Meier.
Luminescence in scanning tunneling microscopy on III–V nanostructures.
Journal of Vacuum Science & Technology B **9**, 409–413 (1991).

[180] U. Håkanson, M. K.-J. Johansson, M. Holm, C. Pryor, L. Samuelson, W. Seifert, and M.-E. Pistol.
Photon mapping of quantum dots using a scanning tunneling microscope.
Applied Physics Letters **81**, 4443–4445 (2002).

[181] G. Hoffmann, L. Libioulle, and R. Berndt.
Tunneling-induced luminescence from adsorbed organic molecules with submolecular lateral resolution.
Physical Review B **65**, 212107 (2002).

[182] Y. Zhang, X. Tao, H. Y. Gao, Z. C. Dong, J. G. Hou, and T. Okamoto.
Modulation of local plasmon mediated emission through molecular manipulation.
Physical Review B **79**, 075406 (2009).

[183] N. L. Schneider, F. Matino, G. Schull, S. Gabutti, M. Mayor, and R. Berndt.
Light emission from a double-decker molecule on a metal surface.
Physical Review B **84**, 153403 (2011).

[184] F. Geng, Y. Zhang, Y. Yu, Y. Kuang, Y. Liao, Z. Dong, and J. Hou.
Modulation of nanocavity plasmonic emission by local molecular states of C60 on Au(111).
Optics Express **20**, 26725–26735 (2012).

[185] X. H. Qiu, G. V. Nazin, and W. Ho.
Vibrationally Resolved Fluorescence Excited with Submolecular Precision.
Science **299**, 542–546 (2003).

[186] Z.-C. Dong, X.-L. Guo, A. S. Trifonov, P. S. Dorozhkin, K. Miki, K. Kimura, S. Yokoyama, and S. Mashiko.
Vibrationally Resolved Fluorescence from Organic Molecules near Metal Surfaces in a Scanning Tunneling Microscope.
Physical Review Letters **92**, 086801 (2004).

[187] C. Chen, P. Chu, C. A. Bobisch, D. L. Mills, and W. Ho.
Viewing the Interior of a Single Molecule: Vibronically Resolved Photon Imaging at Submolecular Resolution.
Physical Review Letters **105**, 217402 (2010).

[188] Z. C. Dong, X. L. Zhang, H. Y. Gao, Y. Luo, C. Zhang, L. G. Chen, R. Zhang, X. Tao, Y. Zhang, J. L. Yang, and J. G. Hou.
Generation of molecular hot electroluminescence by resonant nanocavity plasmons.
Nature Photonics **4**, 50–54 (2010).

[189] M. Bischoff, M. van der Wielen, and H. van Kempen.
STM-induced photon emission spectroscopy of granular gold surfaces in air.
Surface Science **400**, 127–133 (1998).

[190] M. J. Gallagher, S. Howells, L. Yi, T. Chen, and D. Sarid.
Photon emission from gold surfaces in air using scanning tunneling microscopy.
Surface Science **278**, 270–280 (1992).

[191] S. Ushioda.
Scanning tunneling microscope (STM) light emission spectroscopy of surface nanostructures.
Journal of Electron Spectroscopy and Related Phenomena **109**, 169–181 (2000).

[192] G. Reecht, F. Scheurer, V. Speisser, Y. J. Dappe, F. Mathevet, and G. Schull.
Electroluminescence of a Polythiophene Molecular Wire Suspended between a Metallic Surface and the Tip of a Scanning Tunneling Microscope.
Physical Review Letters **112**, 047403 (2014).

[193] M. Reidinger, M. Rydzek, C. Scherdel, M. Arduini-Schuster, and J. Manara.
Low-emitting transparent coatings based on tin doped indiumoxide applied via a sol–gel routine.
Thin Solid Films **517**, 3096–3099 (2009).

[194] J. Pérez-Juste, I. Pastoriza-Santos, L. M. Liz-Marzán, and P. Mulvaney.
Gold nanorods: Synthesis, characterization and applications.
Coordination Chemistry Reviews **249**, 1870–1901 (2005).

[195] C. J. Murphy, T. K. Sau, A. M. Gole, C. J. Orendorff, J. Gao, L. Gou, S. E. Hunyadi, and T. Li.
Anisotropic Metal Nanoparticles: Synthesis, Assembly, and Optical Applications.
Journal of Physical Chemistry B **109**, 13857–13870 (2005).

[196] M.-C. Daniel and D. Astruc.
Gold nanoparticles: assembly, supramolecular chemistry, quantum-size-related properties, and applications toward biology, catalysis, and nanotechnology.
Chemical reviews **104**, 293–346 (2004).

[197] B. Nikoobakht and M. A. El-Sayed.
Evidence for Bilayer Assembly of Cationic Surfactants on the Surface of Gold Nanorods.
Langmuir **17**, 6368–6374 (2001).

[198] T. K. Sau and C. J. Murphy.
Self-Assembly Patterns Formed upon Solvent Evaporation of Aqueous Cetyltrimethylammonium Bromide-Coated Gold Nanoparticles of Various Shapes.
Langmuir **21**, 2923–2929 (2005).

[199] H. Katz-Boon, C. J. Rossouw, M. Weyland, A. M. Funston, P. Mulvaney, and J. Etheridge.
Three-Dimensional Morphology and Crystallography of Gold Nanorods.
Nano Letters **11**, 273–278 (2011).

[200] H. A. Keul, M. Möller, and M. R. Bockstaller.
Structural Evolution of Gold Nanorods during Controlled Secondary Growth.
Langmuir **23**, 10307–10315 (2007).

[201] Z. Wang, M. Mohamed, S. Link, and M. El-Sayed.
Crystallographic facets and shapes of gold nanorods of different aspect ratios.
Surface Science **440**, L809–L814 (1999).

[202] A. D. Nikolov and D. T. Wasan.
Mechanisms of the Assembly of Nano- and Microparticle Two-Dimensional Structures in a Wedge Film.
Industrial & Engineering Chemistry Research **48**, 2320–2326 (2009).

[203] B. Nikoobakht, Z. L. Wang, and M. A. El-Sayed.
Self-Assembly of Gold Nanorods.
The Journal of Physical Chemistry B **104**, 8635–8640 (2000).

[204] N. R. Jana, L. A. Gearheart, S. O. Obare, C. J. Johnson, K. J. Edler, S. Mann, and C. J. Murphy.
Liquid crystalline assemblies of ordered gold nanorods.
Journal of Materials Chemistry **12**, 2909–2912 (2002).

[205] G. Kawamura, Y. Yang, and M. Nogami.
Facile assembling of gold nanorods with large aspect ratio and their surface-enhanced Raman scattering properties.
Applied Physics Letters **90**, 261908 (2007).

[206] Z. Guo, Y. Zhang, Y. DuanMu, L. Xu, S. Xie, and N. Gu.
Facile synthesis of micrometer-sized gold nanoplates through an aniline-assisted route in ethylene glycol solution.
Colloids and Surfaces A: Physicochemical and Engineering Aspects **278**, 33–38 (2006).

[207] Y. Xia, Y. Xiong, B. Lim, and S. E. Skrabalak.
Shape-Controlled Synthesis of Metal Nanocrystals: Simple Chemistry Meets Complex Physics?
Angewandte Chemie International Edition **48**, 60–103 (2009).

[208] A. R. Tao, S. Habas, and P. Yang.
Shape Control of Colloidal Metal Nanocrystals.
Small **4**, 310–325 (2008).

[209] C. Lofton and W. Sigmund.
Mechanisms Controlling Crystal Habits of Gold and Silver Colloids.
Advanced Functional Materials **15**, 1197–1208 (2005).

[210] S. E. Skrabalak, B. J. Wiley, M. Kim, E. V. Formo, and Y. Xia.
On the Polyol Synthesis of Silver Nanostructures: Glycolaldehyde as a Reducing Agent.
Nano Letters **8**, 2077–2081 (2008).

[211] D. Kumar, A. A. Kulkarni, and B. Prasad.
Synthesis of triangular gold nanoplates: Role of bromide ion and temperature.
Colloids and Surfaces A: Physicochemical and Engineering Aspects **422**, 181–190 (2013).

[212] N. C. Lindquist, P. Nagpal, K. M. McPeak, D. J. Norris, and S.-H. Oh.
Engineering metallic nanostructures for plasmonics and nanophotonics.
Reports on Progress in Physics **75**, 036501 (2012).

[213] V. Callegari.
Fabrication of Photonic Elements by Focused Ion Beam (FIB).
Ph.D. thesis, ETH, Zürich (2009).

[214] V. Myroshnychenko, J. Rodríguez-Fernández, I. Pastoriza-Santos, A. M. Funston, C. Novo, P. Mulvaney, L. M. Liz-Marzán, and F. J. García de Abajo.
Modelling the optical response of gold nanoparticles.
Chemical Society Reviews **37**, 1792 (2008).

[215] A. Taflove and S. C. Hagness.
Computational electrodynamics: the finite-difference time-domain method.
Artech House, Boston (2005).

[216] *FDTD Solutions Knowledge Base.*
URL www.lumerical.com/support/knowledge_base (2013).

[217] P. G. Etchegoin, E. C. Le Ru, and M. Meyer.
An analytic model for the optical properties of gold.
The Journal of Chemical Physics **125**, 164705 (2006).

[218] P. G. Etchegoin, E. C. Le Ru, and M. Meyer.
Erratum: "An analytic model for the optical properties of gold" [J. Chem. Phys. 125, 164705 (2006)].
The Journal of Chemical Physics **127**, 189901 (2007).

[219] R. L. Olmon, B. Slovick, T. W. Johnson, D. Shelton, S.-H. Oh, G. D. Boreman, and M. B. Raschke.
Optical dielectric function of gold.
Physical Review B **86**, 235147 (2012).

[220] E. D. Palik.
Handbook of Optical Constants of Solids.
Academic Press (1998).

[221] R. Vogelgesang and A. Dmitriev.
Real-space imaging of nanoplasmonic resonances.
The Analyst **135**, 1175 (2010).

[222] K. Critchley, B. P. Khanal, M. . Górzny, L. Vigderman, S. D. Evans, E. R. Zubarev, and N. A. Kotov.
Near-Bulk Conductivity of Gold Nanowires as Nanoscale Interconnects and the Role of Atomically Smooth Interface.
Advanced Materials **22**, 2338–2342 (2010).

[223] H. Xu, E. J. Bjerneld, M. Käll, and L. Börjesson.
Spectroscopy of single hemoglobin molecules by surface enhanced Raman scattering.
Physical Review Letters **83**, 4357–4360 (1999).

[224] J. N. Farahani, D. W. Pohl, H.-J. Eisler, and B. Hecht.
Single Quantum Dot Coupled to a Scanning Optical Antenna: A Tunable Superemitter.
Physical Review Letters **95**, 017402 (2005).

[225] T. Deckert-Gaudig, F. Erver, and V. Deckert.
Transparent Silver Microcrystals: Synthesis and Application for Nanoscale Analysis.
Langmuir **25**, 6032–6034 (2009).

[226] R. F. Oulton, V. J. Sorger, T. Zentgraf, R.-M. Ma, C. Gladden, L. Dai, G. Bartal, and X. Zhang.
Plasmon lasers at deep subwavelength scale.
Nature **461**, 629–632 (2009).

[227] S. Palomba and L. Novotny.
Near-Field Imaging with a Localized Nonlinear Light Source.
Nano Letters **9**, 3801–3804 (2009).

[228] M. L. Juan, M. Righini, and R. Quidant.
Plasmon nano-optical tweezers.
Nature Photonics **5**, 349–356 (2011).

[229] S. J. van der Molen, J. Liao, T. Kudernac, J. S. Agustsson, L. Bernard, M. Calame, B. J. van Wees, B. L. Feringa, and C. Schönenberger.
Light-controlled conductance switching of ordered metal- molecule- metal devices.
Nano Letters **9**, 76–80 (2009).

[230] A. I. Fernández-Domínguez, S. A. Maier, and J. B. Pendry.
Collection and Concentration of Light by Touching Spheres: A Transformation Optics Approach.
Physical Review Letters **105**, 266807 (2010).

[231] I. Romero, J. Aizpurua, G. W. Bryant, and F. J. García De Abajo.
Plasmons in nearly touching metallic nanoparticles: singular response in the limit of touching dimers.
Optics Express **14**, 9988–9999 (2006).

[232] C. David and F. J. García de Abajo.
Spatial Nonlocality in the Optical Response of Metal Nanoparticles.
Journal of Physical Chemistry C **115**, 19470–19475 (2011).

[233] D. Marinica, A. Kazansky, P. Nordlander, J. Aizpurua, and A. G. Borisov.
Quantum Plasmonics: Nonlinear Effects in the Field Enhancement of a Plasmonic Nanoparticle Dimer.
Nano Letters **12**, 1333–1339 (2012).

[234] J. Kern, S. Großmann, N. V. Tarakina, T. Häckel, M. Emmerling, M. Kamp, J.-S. Huang, P. Biagioni, J. C. Prangsma, and B. Hecht.
Atomic-Scale Confinement of Resonant Optical Fields.
Nano Letters **12**, 5504–5509 (2012).

[235] A. L. Koh, D. W. McComb, S. A. Maier, H. Low, and J. K. W. Yang.
Sub-10 nm patterning of gold nanostructures on silicon-nitride membranes for plasmon mapping with electron energy-loss spectroscopy.
Journal of Vacuum Science Technology B: Microelectronics and Nanometer Structures **28**, C6O45–C6O49 (2010).

[236] F. Schertz, M. Schmelzeisen, R. Mohammadi, M. Kreiter, H.-J. Elmers, and G. Schönhense.
Near Field of Strongly Coupled Plasmons: Uncovering Dark Modes.
Nano Letters **12**, 1885–1890 (2012).

[237] G. Schull, N. Néel, P. Johansson, and R. Berndt.
Electron-Plasmon and Electron-Electron Interactions at a Single Atom Contact.
Physical Review Letters **102**, 057401 (2009).

[238] M. Danckwerts and L. Novotny.
Optical Frequency Mixing at Coupled Gold Nanoparticles.
Physical Review Letters **98**, 026104 (2007).

[239] D. C. Guhr, D. Rettinger, J. Boneberg, A. Erbe, P. Leiderer, and E. Scheer.
Influence of Laser Light on Electronic Transport through Atomic-Size Contacts.
Physical Review Letters **99**, 086801 (2007).

[240] H. Miyazaki and Y. Kurokawa.
Squeezing Visible Light Waves into a 3-nm-Thick and 55-nm-Long Plasmon Cavity.
Physical Review Letters **96**, 097401 (2006).

[241] J. A. Dionne, H. J. Lezec, and H. A. Atwater.
Highly Confined Photon Transport in Subwavelength Metallic Slot Waveguides.
Nano Letters **6**, 1928–1932 (2006).

[242] A. F. Koenderink.
On the use of Purcell factors for plasmon antennas.
Optics Letters **35**, 4208–4210 (2010).

[243] R. Esteban, A. G. Borisov, P. Nordlander, and J. Aizpurua.
Bridging quantum and classical plasmonics with a quantum-corrected model.
Nature Communications **3**, 825 (2012).

[244] T. J. Kippenberg and K. J. Vahala.
Cavity Optomechanics: Back-Action at the Mesoscale.
Science **321**, 1172–1176 (2008).

[245] A. Imamḡolu, H. Schmidt, G. Woods, and M. Deutsch.
Strongly interacting photons in a nonlinear cavity.
Physical Review Letters **79**, 1467 (1997).

[246] I. Smolyaninov, A. Zayats, A. Gungor, and C. Davis.
Single-Photon Tunneling via Localized Surface Plasmons.
Physical Review Letters **88**, 187402 (2002).

[247] T. Brabec and F. Krausz.
Intense few-cycle laser fields: Frontiers of nonlinear optics.
Reviews of Modern Physics **72**, 545 (2000).

[248] J. C. Prangsma, J. Kern, A. G. Knapp, S. Grossmann, M. Emmerling, M. Kamp, and B. Hecht.
Electrically Connected Resonant Optical Antennas.
Nano Letters **12**, 3915–3919 (2012).

[249] A. Lovera and O. J. Martin.
Plasmonic trapping with realistic dipole nanoantennas: Analysis of the detection limit.
Applied Physics Letters **99**, 151104–151104 (2011).

[250] N. Liu, H. Guo, L. Fu, S. Kaiser, H. Schweizer, and H. Giessen.
Three-dimensional photonic metamaterials at optical frequencies.
Nature Materials **7**, 31–37 (2007).

[251] A. Koenderink, M. Kafesaki, B. Buchler, and V. Sandoghdar.
Controlling the Resonance of a Photonic Crystal Microcavity by a Near-Field Probe.
Physical Review Letters **95** (2005).

[252] J. D. Jackson.
Classical electrodynamics.
Wiley (1975).

[253] K.-P. Chen, V. P. Drachev, J. D. Borneman, A. V. Kildishev, and V. M. Shalaev.
Drude Relaxation Rate in Grained Gold Nanoantennas.
Nano Letters **10**, 916–922 (2010).

[254] F. Léonard and A. A. Talin.
Electrical contacts to one- and two-dimensional nanomaterials.
Nature Nanotechnology **6**, 773–783 (2011).

[255] D. R. Strachan, D. E. Smith, D. E. Johnston, T.-H. Park, M. J. Therien, D. A. Bonnell, and A. T. Johnson.
Controlled fabrication of nanogaps in ambient environment for molecular electronics.
Applied Physics Letters **86**, 043109 (2005).

[256] G. C. Gazzadi, E. Angeli, P. Facci, and S. Frabboni.
Electrical characterization and Auger depth profiling of nanogap electrodes fabricated by I2-assisted focused ion beam.
Applied Physics Letters **89**, 173112 (2006).

[257] T. Nagase, K. Gamo, T. Kubota, and S. Mashiko.
Direct fabrication of nano-gap electrodes by focused ion beam etching.
Thin Solid Films **499**, 279–284 (2006).

[258] T. Nagase, T. Kubota, and S. Mashiko.
Fabrication of nano-gap electrodes for measuring electrical properties of organic molecules using a focused ion beam.
Thin Solid Films **438**–**439**, 374–377 (2003).

[259] J. Chen, V. Perebeinos, M. Freitag, J. Tsang, Q. Fu, J. Liu, and P. Avouris.
Bright Infrared Emission from Electrically Induced Excitons in Carbon Nanotubes.
Science **310**, 1171–1174 (2005).

[260] E. D. Minot, F. Kelkensberg, M. van Kouwen, J. A. van Dam, L. P. Kouwenhoven, V. Zwiller, M. T. Borgström, O. Wunnicke, M. A. Verheijen, and E. P. A. M. Bakkers.
Single Quantum Dot Nanowire LEDs.
Nano Letters **7**, 367–371 (2007).

[261] K. C. Y. Huang, M.-K. Seo, Y. Huo, T. Sarmiento, J. S. Harris, and M. L. Brongersma.
Antenna electrodes for controlling electroluminescence.
Nature Communications **3**, 1005 (2012).

[262] M. Nothaft, S. Höhla, F. Jelezko, N. Frühauf, J. Pflaum, and J. Wrachtrup.
Electrically driven photon antibunching from a single molecule at room temperature.
Nature Communications **3**, 628 (2012).

[263] P. Biagioni, J. S. Huang, L. Duò, M. Finazzi, and B. Hecht.
Cross Resonant Optical Antenna.
Physical Review Letters **102**, 256801 (2009).

[264] K. Moth-Poulsen and T. Bjørnholm.
Molecular electronics with single molecules in solid-state devices.
Nature Nanotechnology **4**, 551–556 (2009).

[265] F.-Q. Xie, L. Nittler, C. Obermair, and T. Schimmel.
Gate-Controlled Atomic Quantum Switch.
Physical Review Letters **93**, 128303 (2004).

[266] A. M. Kern and O. J. F. Martin.
Excitation and Reemission of Molecules near Realistic Plasmonic Nanostructures.
Nano Letters **11**, 482–487 (2011).

[267] N. Liu, F. Wen, Y. Zhao, Y. Wang, P. Nordlander, N. J. Halas, and A. Alù.
Individual Nanoantennas Loaded with Three-Dimensional Optical Nanocircuits.
Nano Letters **13**, 142–147 (2012).

[268] J. Zuloaga and P. Nordlander.
On the Energy Shift between Near-Field and Far-Field Peak Intensities in Localized Plasmon Systems.
Nano Letters **11**, 1280–1283 (2011).

[269] U. Kubitscheck.
Fluorescence Microscopy: From Principles to Biological Applications.
John Wiley & Sons (2013).

[270] A. Surrey, D. Pohl, L. Schultz, and B. Rellinghaus.
Quantitative Measurement of the Surface Self-Diffusion on Au Nanoparticles by Aberration-Corrected Transmission Electron Microscopy.
Nano Letters **12**, 6071–6077 (2012).

[271] C. Beenakker and H. Schomerus.
Antibunched Photons Emitted by a Quantum Point Contact out of Equilibrium.
Physical Review Letters **93** (2004).

[272] J. Kim, O. Benson, H. Kan, and Y. Yamamoto.
A single-photon turnstile device.
Nature **397**, 500–503 (1999).

[273] Z. Yuan, B. E. Kardynal, R. M. Stevenson, A. J. Shields, C. J. Lobo, K. Cooper, N. S. Beattie, D. A. Ritchie, and M. Pepper.
Electrically Driven Single-Photon Source.
Science **295**, 102–105 (2002).

[274] I. C. Fulga, F. Hassler, and C. W. J. Beenakker.
Nonzero temperature effects on antibunched photons emitted by a quantum point contact out of equilibrium.
Physical Review B **81** (2010).

Acknowledgements

It is important to note, that this dissertation would not have been possible without the excellent environment and team-work. I am thankful to all the people that have contributed to this thesis and I cannot acknowledge everyone in detail. However, I want to thank some persons explicitly:

- Prof. Dr. Bert Hecht for giving me the opportunity to work in this exciting research field. I enjoyed many fruitful discussions and I am thankful for valuable advice. Moreover, I want to thank for the possibilities to visit several conferences.

- Dr. Jord Prangsma for the amazing teamwork during the study of electrically-connected antennas. Your profound theoretical background and structural thinking have often shone new light on persistent problems. Moreover, I am very thankful for proof-reading parts of this thesis and for the valuable comments.

- Dr. Rene Kullock for the wonderful teamwork during the investigation of the sub-wavelength photon source. It would have been difficult to bear all the frustration alone. The evenings at the Standard and the table football games were a lot of fun.

- Swen Grossmann for the excellent help during the measurements for the atomic-scale confinement of resonant optical field manuscript. I am very thankful for proof-reading this thesis and for the valuable comments. Our evening events were always fun.

- Dr. Xiaofei Wu for expertise on the synthesis of single-crystalline gold flakes growth and for programming an automated-alignement script for the focused-ion-beam.

- Dr. Paolo Biagioni and Dr. Jer-Shing Huang for various scientific discussions and comments during the preparation of manuscripts. I also enjoyed our time at various conferences.

- the Technical physics department at the University of Würzburg for providing marker and electrode structures as well as water of highest quality. Special thanks go to Monika Emmerling for devoting her precious time to the development and execution of electron and optical lithography. I thank Nadezda Tarakina and Martin Kamp for the recording of the STEM images of atomic-scale gaps. Moreover, I highly appreciate the excellent comments Martin Kamp gave at various discussions.

- Patrick Then for proof-reading this thesis and for the valuable comments.

- the other members of the AG-Hecht for various dicussions during coffee breaks or at the group meeting.
- the Stammtisch guys for being great friends and for relaxing evenings.
- my girlfriend Judith for her patience, understanding and love.
- my parents and my family for their support and love.